

Understanding Photoexcited Charge Carrier Dynamics in Methylammonium Lead  
Iodide Perovskite Thin Films by Pump Probe Microscopy

by

Yuheng Liao

Department of Physics  
Duke University

Date: \_\_\_\_\_

Approved:

\_\_\_\_\_  
Warren S. Warren, Supervisor

\_\_\_\_\_  
Martin C. Fischer

\_\_\_\_\_  
Adam P. Wax

\_\_\_\_\_  
Glenn S. Edwards

\_\_\_\_\_  
Michael Rubinstein

Dissertation submitted in partial fulfillment of  
the requirements for the degree of Doctor  
of Philosophy in the Department of  
Physics in the Graduate School  
of Duke University

2021

ABSTRACT

Understanding Photoexcited Charge Carrier Dynamics in Methylammonium Lead  
Iodide Perovskite Thin Films by Pump Probe Microscopy

by

Yuheng Liao

Department of Physics  
Duke University

Date: \_\_\_\_\_

Approved:

\_\_\_\_\_  
Warren S. Warren, Supervisor

\_\_\_\_\_  
Martin C. Fischer

\_\_\_\_\_  
Adam P. Wax

\_\_\_\_\_  
Glenn S. Edwards

\_\_\_\_\_  
Michael Rubinstein

An abstract of a dissertation submitted in partial  
fulfillment of the requirements for the degree  
of Doctor of Philosophy in the Department of  
Physics in the Graduate School of  
Duke University

2021

Copyright by  
Yuheng Liao  
2021

## Abstract

Metal halide perovskite-based thin films, the light harvesting layer in perovskite solar cells, have received increasing attention since 2012. Although many studies have focused on elucidating the complicated dynamics involved in the photoexcitation process of metal halide perovskite-based thin film and their impacts on charge carrier behaviors, the ultrafast photoexcited dynamics (within the first picosecond) and spatial heterogeneity of those dynamics are often overlooked or investigated separately.

In this dissertation, I demonstrate the ability of pump probe microscopy (PPM) to reveal the photoexcited charge carrier dynamics in methylammonium lead iodide (MAPbI<sub>3</sub>) perovskite thin films with sub-picosecond temporal resolution and sub-micrometer spatial resolution. Spatial mapping between PPM images and fluorescence lifetime microscopy (FLIM) images of MAPbI<sub>3</sub> perovskite thin films is achieved to bridge the different time scales of charge carrier dynamics at the same region. By spatially overlapping PPM and FLIM images with scanning electron microscopy (SEM) images, I demonstrate that the spatial heterogeneity of charge carrier dynamics is not solely dependent on the morphology of MAPbI<sub>3</sub> perovskite thin films. Additionally, a model is introduced to decompose the pump probe and fluorescence signal and separate different charge carrier dynamics. Sub-picosecond charge carrier dynamics obtained from pump-probe signals with various probing wavelengths are used to monitor the

cooling process of charge carriers and extract the time-resolved charge carrier temperature with micrometer spatial resolution. In the end, I discuss the potential of PPM in investigating degradation and different microstructures of MAPBI<sub>3</sub> perovskite thin films.

## **Dedication**

For my family, Jianwen Liao, Hong Wu, Hanmu Liao, Xuejiao Hu, Yuxin Lian  
and my fiancée, Yuan Pan.

# Contents

Abstract .....	iv
List of Tables .....	x
List of Figures .....	xi
List of Abbreviation .....	xiv
1 Introduction.....	1
1.1 Introduction to perovskite solar cells .....	2
1.2 Electron band structure of semiconductors .....	3
1.3 Recombination processes in semiconductors .....	7
1.4 Shockley-Queisser limit for single junction solar cells.....	10
1.5 Pump probe microscopy and fluorescence lifetime microscopy .....	11
1.5.1 <i>Nonlinear optical interactions</i> .....	13
1.5.2 <i>Pump probe microscopy</i> .....	16
1.5.3 <i>Fluorescence lifetime microscopy</i> .....	18
1.6 Progress of pump probe microscopy studies on perovskite thin films .....	20
1.7 Thesis outline .....	28
2 Probing the spatial heterogeneity of charge carrier dynamics in CH <sub>3</sub> NH <sub>3</sub> PbI <sub>3</sub> perovskite thin films with femtosecond time-resolved nonlinear optical microscopy.....	30
2.1 Optical microscopy setup.....	31
2.1.1 Pump probe microscopy setup.....	31
2.1.2 Noise analysis of the pump probe microscopy.....	33
2.1.3 Fluorescence lifetime microscopy setup .....	34

2.1.4	Phasor analysis .....	35
2.2	Charge carrier density calculation .....	37
2.3	Experimental results.....	39
2.3.1	Pump probe microscopy images of MAPbI <sub>3</sub> thin films .....	39
2.3.2	Power study of the pump-probe signal .....	41
2.3.3	Phasor analysis of pump probe microscopy data.....	45
2.3.4	Correlation between phasor and SEM images .....	48
2.3.5	Phasor analysis of fluorescence lifetime microscopy data .....	50
2.4	Conclusion .....	54
3	Separating and bridging charge carrier dynamics of MAPbI <sub>3</sub> thin films on different timescales .....	56
3.1	Experimental adjustment .....	56
3.2	Model for charge carrier dynamics .....	57
3.2.1	Model for charge carrier dynamics in pump-probe traces.....	57
3.2.2	Model for charge carrier dynamics in fluorescence traces .....	61
3.3	Fitting result of PPM and FLIM traces .....	62
3.4	Correlation between charge carrier dynamics and the sample's morphology .	68
3.5	Combining FLIM and PPM for the quality evaluation of MAPbI <sub>3</sub> perovskite thin films .....	73
3.6	Conclusion .....	76
4	Analyzing the hot carrier cooling process in MAPbI <sub>3</sub> thin films by multi-wavelength pump probe microscopy .....	78
4.1	Introduction to hot carrier harvesting in solar cells .....	78

4.2	Hot carrier cooling model .....	80
4.3	Spectra of pump-probe signals.....	84
4.4	Local temperature analysis .....	87
4.5	Conclusion.....	91
5	Future research directions and conclusion .....	92
5.1	Revealing degradation on MAPbI <sub>3</sub> perovskite thin films by pump probe microscopy .....	92
5.2	Investigating the charge carrier dynamics of MAPbI <sub>3</sub> thin films with different microstructures.....	94
5.3	Conclusion.....	96
	Appendix A: Power study of the pump-probe signal .....	99
	Appendix B: Single pixel fitting of PPM and FLIM .....	102
	Appendix C: Information of MAPbI <sub>3</sub> thin films .....	104
	Reference .....	105
	Biography.....	113

## List of Tables

Table 1: Intensity dependence of two charge carrier dynamics .....	43
Table 2: Fitting parameters of pump-probe traces in the first 10ps .....	64
Table 3: Fitting parameters of fluorescence and pump-probe signal .....	67
Table 4: Fitting parameters of individual pixels.....	103

## List of Figures

Figure 1: Traditional silicon solar cells and perovskite solar cells.....	3
Figure 2: Electron band structure. ....	6
Figure 3: Energy diagram for solar cells.....	7
Figure 4: Mechanism of charge carrier recombination. ....	8
Figure 5: Spectrum losses counted in Shockley-Queisser limit.....	11
Figure 6: Common nonlinear interactions used in pump probe microscopy.....	13
Figure 7: Time-resolved pump-probe signal of common nonlinear optical interactions. ....	17
Figure 8: Principle of the time-correlated single photon counting technique.....	19
Figure 9: Linear absorption and fluorescence emission spectrum and SEM image of the MAPbI <sub>3</sub> thin film. ....	21
Figure 10: Pump probe microscopy images of MAPbI <sub>3</sub> thin films with different probe wavelengths.....	23
Figure 11: Pump probe microscopy images of the carrier transport in a hybrid perovskite thin film. ....	24
Figure 12: Effects of a refractive index change in pump probe reflection imaging.....	26
Figure 13: Pump probe microscopy setup.....	31
Figure 14: Time-resolved Pump-probe traces and pump-probe image at fixed time.....	33
Figure 15: Fluorescence lifetime microscopy setup.....	35
Figure 16: Phasor plots.....	36
Figure 17: Pump probe microscopy image of MAPbI <sub>3</sub> thin films. ....	39
Figure 18: Power study of two types of pump-probe traces.....	42
Figure 19: Energy diagram of MAPbI <sub>3</sub> thin films. ....	44

Figure 20: Phasor plot of PPM data.....	46
Figure 21: Phasor image and PPM image of the same region. ....	47
Figure 22: Overlapped images of phasor and SEM.....	48
Figure 23: FLIM and reflectance images of MAPbI <sub>3</sub> thin films.....	50
Figure 24: Phasor plot of FLIM data.....	52
Figure 25: Fluorescence lifetime histogram of regions with different PPM phasor locations.....	54
Figure 26: Pump-probe signal of two charge carrier dynamics. ....	60
Figure 27: Pump-probe traces under adjusted beam power.....	62
Figure 28: Fitting traces of PPM data. ....	63
Figure 29: Pump-probe traces of individual charge carrier dynamics.....	64
Figure 30: Fitting result of the fluorescence trace.....	66
Figure 31: Heterogeneous fluorescence signal observed in MAPbI <sub>3</sub> thin films. ....	67
Figure 32: Combined images of SEM and different radiative recombination processes..	69
Figure 33: Combined images of SEM and different charge carrier dynamics in nanosecond scales. ....	71
Figure 34: Long-lived bleaching signal comparison across grains. ....	72
Figure 35: Correlation plot between the long-live bleaching signal and the band-to-band recombination signal. ....	74
Figure 36: Spatial distribution of pixels with high ratio ( $R > 1.54$ ) between the band-to-band recombination signal and the long-lived bleaching signal. ....	75
Figure 37: Spatial distribution of pixels with low ratio ( $R < 0.65$ ) between the band-to-band recombination signal and the long-lived bleaching signal. ....	76
Figure 38: Mechanism for hot carrier harvesting. ....	79

Figure 39: Hot carrier cooling model. ....	81
Figure 40: Spectra of pump-probe signal at different time delays.....	82
Figure 41: Pump-probe traces with different probe beam wavelengths.....	86
Figure 42: Spectra of the pump-probe signal. ....	87
Figure 43: Spectra of pump-probe signal with fitting result and time-resolved electron temperatures.....	88
Figure 44: Electron temperature map at 0.5ps and hot carrier cooling time map. ....	90
Figure 45: Phasor plots of pump-probe signal from the sealed and unsealed samples....	93
Figure 46: Phasor, SEM, and combined images of MAPbI <sub>3</sub> samples. ....	95
Figure 47: Pump power dependence of the instantaneous peak. ....	99
Figure 48: Probe power dependence of the instantaneous peak.....	100
Figure 49: Pump power dependence of the long-lived bleaching signal.....	101
Figure 50: Probe power dependence of the long-lived bleaching signal. ....	101
Figure 51: Single pixel fitting of the fluorescence signal. ....	102
Figure 52: Single pixel fitting of the pump-probe signal in picosecond scales. ....	102
Figure 53: SEM image of MAPbI <sub>3</sub> thin films used in our experiments.....	104

## List of Abbreviation

AOM	Acousto-optic modulator
A.U.	Arbitrary unit
ETM	Electron transport materials
ESA	Excited state absorption
FLIM	Fluorescence lifetime microscopy
GSD	Ground state depletion
HTM	Hole transport materials
OPO	Optical parametrical oscillator
PPM	Pump probe microscopy
PD	Photodiode
PCE	Power conversion efficiency
PMT	Photomultiplier tube
SEM	Scanning electron microscopy
SE	Stimulated emission
SRS	Stimulated Raman scattering
TCSPC	Time-correlated single photon counting
TPA	Two-photon absorption

# 1 Introduction

In the past decade, organic-inorganic halide perovskite solar cells have received enormous attention due to their outstanding power conversion efficiency (PCE), simple fabrication process and tunable absorption range. To date, the highest certified single-junction perovskite solar cell PCE reported is 25.2%<sup>1</sup>. Together with its scalable solution-based fabrication method and low processing costs, organic-inorganic halide perovskite solar cells have already demonstrated the potential to be the next generation solar cell<sup>2</sup>.

To further improve the device performance of perovskite solar cells, researchers now put focus on understanding the photoexcitation processes behind the photovoltaic properties of these materials. By elucidating the complicated charge carrier dynamics involved in photoexcitation processes and the impact of perovskite thin films' microstructure on these dynamics, defect engineering<sup>3</sup> and structure tailoring<sup>4</sup> can be realized to optimize the performance of perovskite solar cells.

Multiple optical methods are employed to investigate the charge carrier dynamics of perovskite thin films. For example, time-resolved pump probe spectroscopy and time-resolved fluorescence lifetime microscopy (FLIM) are widely used to monitor the charge carrier behavior after photoexcitation<sup>5-14</sup>. However, the spectroscopy methods generally analyze the average signal over a large area and fail to provide spatial information. FLIM, in another hand, has micrometer scale spatial resolution but can only

investigate certain charge carrier dynamics, which are radiative processes, in nanosecond time scales.

In this dissertation, I will demonstrate the use of pump probe microscopy (PPM) and FLIM to monitor photoexcited charge carrier dynamics in methylammonium lead iodide (MAPbI<sub>3</sub>) perovskite thin films with sub-picosecond temporal resolution and sub-micrometer spatial resolution.

## ***1.1 Introduction to perovskite solar cells***

Solar cells are electrical devices that harvest solar energy and convert it to electricity via the photovoltaic effect<sup>15</sup>. Traditional solar cells utilize doped silicon to form a PN junction (figure 1a). The depletion zone between P-type silicon and N-type silicon serves as the light harvesting region. When a photon of light is absorbed in this region, a free electron and hole pair is created. The potential difference across the PN junction drives the electron to the cathode and the hole to the anode. If an external circuit is connected to the electrodes, an electric current will flow from the anode to the cathode and the energy conversion is completed.

Instead of using doped silicon to collect light, perovskite solar cells employ materials having ABX<sub>3</sub> crystal structure as their light-harvesting layers. Materials having such crystal structure are called perovskite materials. In this dissertation, we focus on the organic metal halide perovskite (CH<sub>3</sub>NH<sub>3</sub>PbI<sub>3</sub>, MAPbI<sub>3</sub>), which has organic cations CH<sub>3</sub>NH<sub>3</sub><sup>+</sup> (MA) as A, divalent metal atoms Pb<sup>2+</sup> as B and halide anions I<sup>-</sup> as X in the

crystal structure. Electron and hole transport layers are added (figure 1b) in perovskite solar cells to help the separation and transport of free electrons and holes created by light absorption. Due to the high optical absorption of perovskite materials, perovskite thin films deposited from solution whose thickness are around 300nm are widely used in perovskite solar cells<sup>16, 17</sup>.

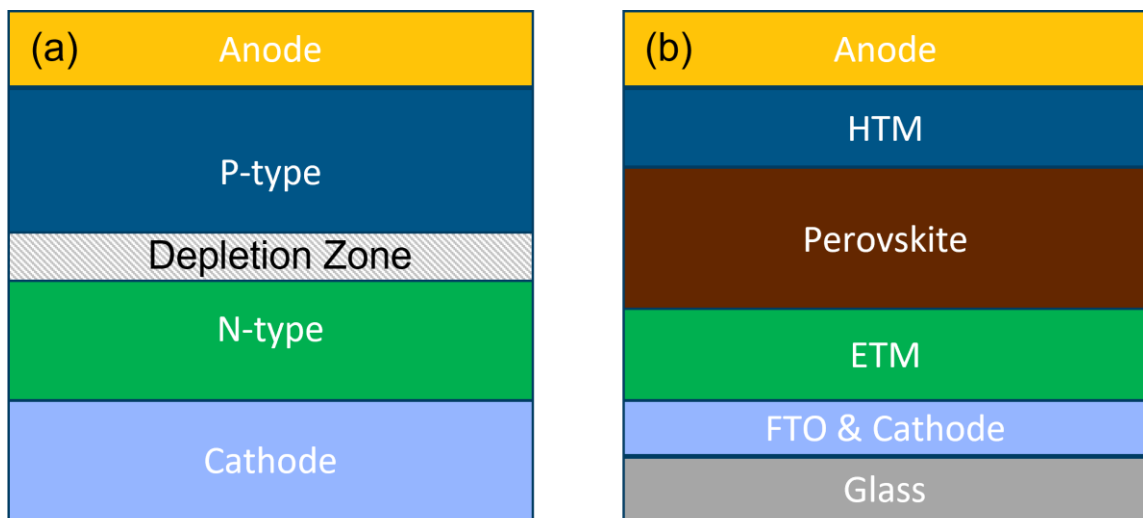


**Figure 1: Traditional silicon solar cells and perovskite solar cells. (a) Traditional silicon solar cells contain P-type silicon layer, N-type silicon layer and electrodes. The depletion zone in the PN junction serves as the light absorption area. (b) Perovskite solar cells contain perovskite materials, hole transport materials (HTM) such as spiro-OMeTAD, electron transport materials (ETM) such as TiO<sub>2</sub>, Fluorine-doped Tin Oxide (FTO) glass, electrodes, and cover glass. FTO glass is a transparent conductive metal oxide used in the fabrication of transparent cathodes.**

## **1.2 Electron band structure of semiconductors**

The electron band structure is the fundamental of photoexcitation processes and the charge carrier transport of semiconductors. A simple model of electron band structure is introduced to better understand the photon-electron interaction in solar cells.

According to the Bloch's theorem<sup>18</sup>, the wave functions of an electron in crystal structure having periodic potential can be written as:

$$\psi(\mathbf{r}) = e^{i\mathbf{k}\cdot\mathbf{r}}u(\mathbf{r}) \quad (1)$$

where  $\psi$  is the wave function,  $\mathbf{r}$  is the position vector,  $\mathbf{k}$  is the crystal momentum vector, and  $u$  is a periodic function that has the same periodicity as the crystal. In the tight binding model<sup>18</sup>, which assumes that electrons are tightly bound to the local atoms and have limited interaction with surrounding atoms, the crystal Hamiltonian  $H_c$  can be expressed by the Hamiltonian of an isolated atom  $H_a$  with a small correction term to the atomic potential  $\Delta V$ :

$$H_s = H_a + \Delta V \quad (2)$$

A solution of the wave function to the time-independent crystal Schrödinger equation can be approximated as a linear combination of atom orbitals  $\varphi_m$ :

$$\psi_m(\mathbf{r}) = \sum_{\mathbf{R}_n} a_m(\mathbf{R}_n) \varphi_m(\mathbf{r} - \mathbf{R}_n) \quad (3)$$

where  $\mathbf{R}_n$  is the atom location in the crystal and  $m$  refers to the atomic energy level. By solving equations 1 and 3, the wave function can be expressed as:

$$\psi_m(\mathbf{r}) = \frac{1}{\sqrt{N}} \sum_{\mathbf{R}_n} e^{i\mathbf{k}\cdot\mathbf{R}_n} \varphi_m(\mathbf{r} - \mathbf{R}_n) \quad (4)$$

where  $N$  is the number of atoms in the crystal. The general wave function can be written as a linear combination of wave functions of different atomic energy levels:

$$\psi(\mathbf{r}) = \sum_m a_m \psi_m(\mathbf{r}) \quad (5)$$

The crystal Schrödinger equation is written as:

$$H_s\psi(\mathbf{r}) = (H_a + \Delta V)\psi(\mathbf{r}) = \varepsilon(\mathbf{k})\psi(\mathbf{r}) \quad (6)$$

where  $\varepsilon(\mathbf{k})$  is the energy associated with the wave function  $\psi(\mathbf{r})$ . Due to the tight binding between electrons and local atoms, the energy associated with the wave function  $\psi$  is close to the energy of atomic levels. However, instead of being a fixed value at a certain atomic level, the electron energy now is a function of the crystal momentum  $k$  ranging through  $N$  values. As  $N$  increases, an energy band is formed close to the energy of atomic levels (figure 2). For example, the energy band close to the  $m$ -th atomic energy level can be expressed by multiply the crystal Schrödinger equation by the wave function  $\psi_m^*(\mathbf{r})$  and integrate over all  $\mathbf{r}$  :

$$\int \psi_m^*(\mathbf{r})(H_a + \Delta V)\psi(\mathbf{r}) d\mathbf{r} = \varepsilon(\mathbf{k}) \int \psi_m^*(\mathbf{r})\psi(\mathbf{r}) d\mathbf{r} \quad (7)$$

utilize the eigenenergy of  $H_a$  and the orthonormality of different atom orbitals, the electron energy inside the  $m$ -th energy band is:

$$\varepsilon(\mathbf{k}) = E_m + \frac{1}{a_m} \int \psi_m^*(\mathbf{r})\Delta V\psi(\mathbf{r}) d\mathbf{r} \quad (8)$$

where  $E_m$  is the energy of the  $m$ -th atomic level. The width of the energy band is closely related to the interatomic spacing since  $\Delta V$  becomes more significant as the distance between electrons reduces. When the electrons are far apart. The energy band returns to the fixed value  $E_m$ .

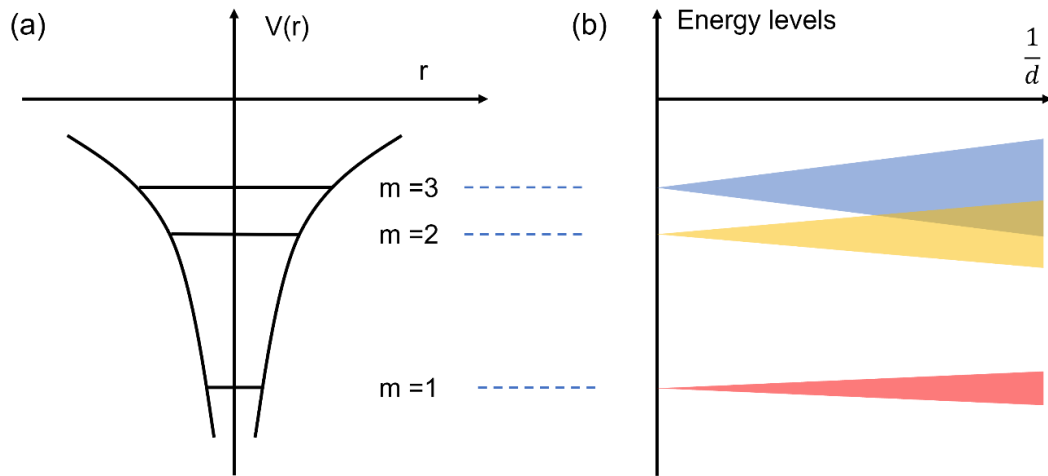


**Figure 2: Electron band structure. (a) Electronic levels of an isolated atom. (b) The energy levels for a system having  $N$  such atoms in a periodic array. The interatomic distance is  $d$ . When atoms become closer, energy bands are formed with  $N$  available values in each band.**

For different materials, the occupation of each energy band varies. For the semiconductors, the valence band is the outermost energy band that is fully occupied by electrons. The unoccupied energy band next to the valence band is called the conduction band. No electronic states exist between these two bands, therefore, the range between them is called the band gap. The energy difference between these two bands is the band gap energy. Normally, photons with energy larger than the band gap energy can excite electrons from the valence band to the conduction band (figure 3). Due to the large population of available energy states in the conduction band, excited electrons can freely move in the material and form current between regions having potential difference. It is how the solar cells generate and transport excited electrons.

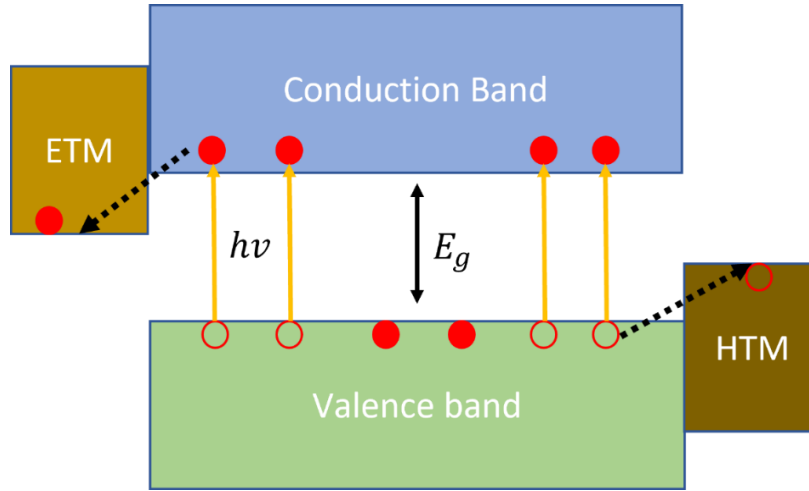


Figure 3: Energy diagram for solar cells. Electrons in the valence band absorb photons with energy  $h\nu$  greater than the band gap energy  $E_g$  and move to the conduction band. Excited electrons and holes move to the electron transport material (ETM) and the hole transport material (HTM) due to the potential difference between materials.

### 1.3 Recombination processes in semiconductors

Since the remarkable PCE of perovskite solar cells is closely related to the long lifetime<sup>19, 20</sup>, long diffusion lengths<sup>21</sup> and low recombination rates<sup>20, 22</sup> of charge carriers in perovskite layers, a better understanding of charge carrier recombination processes is required for further improvement of the PCE of perovskite solar cells.

In semiconductors, charge carrier recombination is usually expressed as:

$$\frac{dn}{dt} = -k_1n - k_2n^2 - k_3n^3 \quad (9)$$

where  $n$  represents the photoexcited charge carrier density.  $k_1$  is the first-order Shockley-Read-Hall (SRH) trapping rate constant and describes the trap-assisted recombination of electrons or holes.  $k_2$  is the second-order band-to-band recombination

rate constant that shows the radiative recombination of an electron hole pair.  $k_3$  only becomes significant with very high light intensity. It represents the third-order Auger recombination which is a non-radiative recombination involving three charge carriers.

Figure 4 shows the mechanism of these recombination.

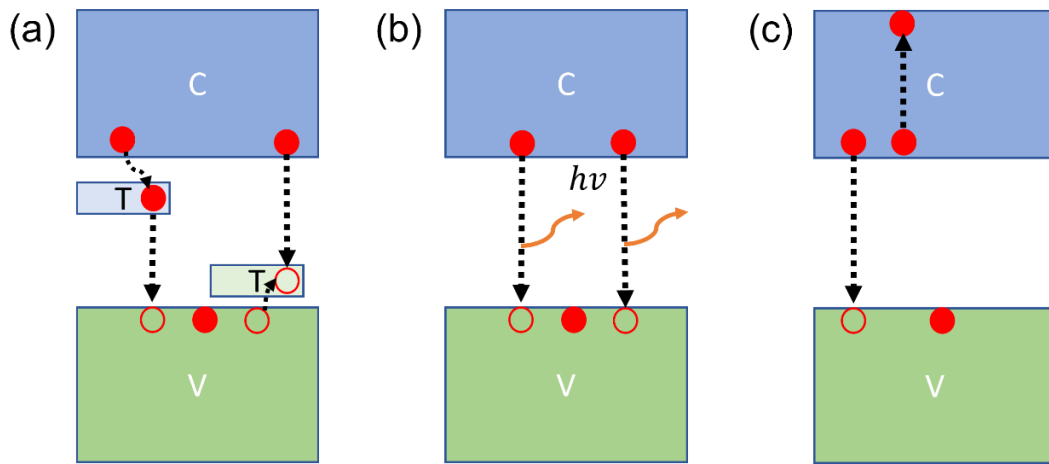


**Figure 4: Mechanism of charge carrier recombination. C is the conduction band and V is the valence band. Solid and hollow circles represent electrons and holes respectively. (a) Trap-assisted recombination. Trapping states are in the band gap, electrons and holes first enter these states and then relax to the ground state. T stands for trapping states. (b) Band-to-band recombination. Radiative recombination of an electron hole pair release energy via photon emission. (c) Auger recombination. The energy released from the recombination of an electron hole pair is absorbed by another electron in the conduction band to reach to a higher energy state.**

For the trap-assisted recombination, the excited electron or hole enters a localized state (trapping state) with energy between the band gap created by a defect in the crystal lattice before relaxing to the ground state. This recombination is mainly non-radiative, the energy dissipates via lattice vibration. For the band-to-band recombination, an excited electron jumps from the conduction band to the valence band and fills a hole.

The energy is released via a photon emission. For the Auger recombination, an excited electron jumps back to the valence band and fills a hole, the released energy is absorbed by another excited electron to move to higher energy states. Since three charge carriers are involved, this recombination requires very high charge carrier density to be significant.

When the charge carrier density remains low, the dominant recombination process is the trap-assisted recombination. Increasing charge carrier population will fill up trapping states. The existence of large amount of free electron and hole pairs makes the band-to-band recombination significant. Further increase of charge carrier population will raise the possibility of the three-particle interaction and lead to dominant Auger recombination. The charge carrier density change under each dominant recombination is listed:

$$n(t) = n_0 e^{-k_1 t} \quad (\text{Trap-assisted recombination}) \quad (10)$$

$$n(t) = \frac{n_0}{1+n_0 k_2 t} \quad (\text{Band-to-band recombination}) \quad (11)$$

$$n(t) = \frac{n_0}{\sqrt{1+2n_0^2 k_3 t}} \quad (\text{Auger recombination}) \quad (12)$$

According to these recombination processes, the diffusion length of charge carriers can be calculated by:

$$r(n) = k_1 + k_2 n + k_3 n^2 \quad (13)$$

$$L_D(n) = \sqrt{\frac{\mu k_B T}{r(n) e}} \quad (14)$$

where  $r(n)$  is the total recombination rate of charge carriers,  $\mu$  is the mobility of charge carriers,  $T$  and  $k_B$  represents temperature and Boltzmann constant respectively and  $e$  is the elementary charge<sup>21, 23</sup>. In realistic situations, the trap-assisted recombination is the dominant recombination process in solar cells under 1-sun illumination (1000 W/m<sup>2</sup> and 25°C standard cell temperature), with the exception that concentrator solar cells use lenses to focus sunlight and achieve high charge carrier density<sup>24</sup>. Therefore, the diffusion length usually depends mainly on  $k_1$ , which is associated with the available trapping states. To obtain a longer diffusion length, trapping states should be minimized by reducing defects and structural disorder in the perovskite layer.

#### ***1.4 Shockley-Queisser limit for single junction solar cells***

Despite various optimizations made to improve the PCE of solar cells, there is a maximum theoretical PCE for solar cells with a single PN junction. It is called the Shockley-Queisser limit. The limit considers energy losses due to the blackbody radiation, radiative recombination between free electron-hole pairs, impedance matching and the spectrum losses. A large portion of the energy losses (52% energy losses for a single junction silicon solar cell<sup>25</sup>) are from the spectrum losses: only photons with more energy than the bandgap energy (the energy difference between the valence

band and the conduction band) of the light harvesting material in the solar cell can create electron-hole pairs and be converted to electricity. Additionally, energy above the bandgap energy is lost during thermalization (figure 5b). One way to exceed the Shockley-Queisser limit is to collect high-energy electrons, also known as hot carriers, before they thermalize to the band edge<sup>26</sup>. A more detailed discussion of the hot carrier harvesting will be provided in chapter 4.

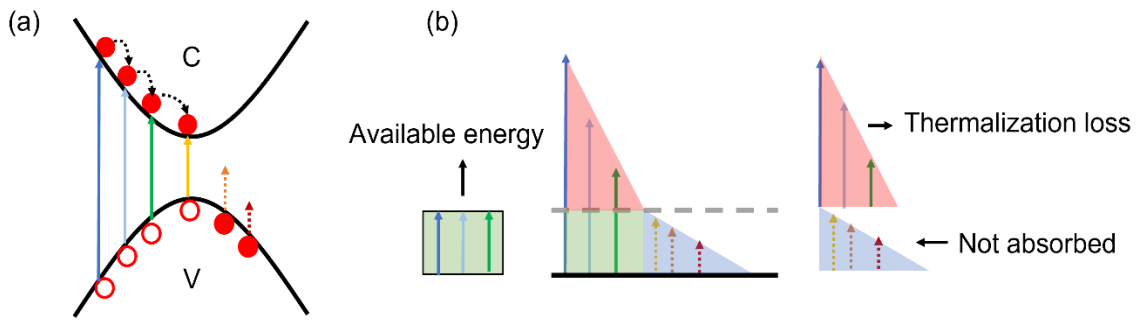


**Figure 5: Spectrum losses counted in Shockley-Queisser limit. (a) Excited electrons (solid red circles) and holes (hollow red circles) created by photons with different energy. The length of arrows represents the amplitude of photon energy. V stands for the valence band and C stands for the conduction band. Black dash arrows show the thermalization process where high energy electrons relax to the band edge. (b) Spectrum losses due to the band gap limitation and the thermalization. The green area shows the available solar energy for electricity conversion. The red area shows the energy loss due to the thermalization. Excess electron energy above the band edge will be lost and converted to heat. In the blue area, photons with energy less than the band gap are not harvested by the solar cell.**

### ***1.5 Pump probe microscopy and fluorescence lifetime microscopy***

The simple and scalable solution-base fabrication method of perovskite thin films gives perovskite solar cells great economic potential<sup>27</sup>. Meanwhile, various types of defects and spatial heterogeneities are inevitably introduced to the perovskite thin films

during fabrication. To study the impact of defects and spatial heterogeneity on the charge carrier dynamics of perovskite thin films, spatial and temporal resolution are required. Scanning electron microscopy (SEM) can provide nanometer spatial resolution but the temporal resolution is absent. Conventional transient absorption spectroscopy and time-resolved photoluminescence spectroscopy can monitor charge carrier dynamics with sub-picosecond and sub-nanosecond temporal resolution respectively. However, their signals usually represent the average value from a large area. Little spatial information is provided, and the local heterogeneity of charge carrier dynamics is overlooked.

To achieve spatial and temporal resolution at the same time for the study of charge carrier dynamics of perovskite thin films, time-resolved fluorescence lifetime microscopy (FLIM) and pump probe microscopy (PPM) are adapted. FLIM can monitor radiative recombination processes of charge carriers and characterize the charge carrier lifetime. The micrometer spatial resolution of FLIM can reveal the region having abundant defects like grain boundaries<sup>10</sup>. Instead of representing only radiative recombination processes, PPM can monitor the change of the total charge carrier population, which includes both radiative and non-radiative recombination processes. The sub-picosecond temporal resolution of PPM enables the study of the ultrafast charge carrier dynamics within the first several picoseconds such as the hot carrier cooling process and charge carrier transport between the perovskite thin films or the electron

and hole transport layers. Additionally, the sub-micrometer spatial resolution of PPM can provide localized information of the charge carrier population. However, typical PPM only measures the charge carrier behaviors within several hundred of picoseconds which limits the study of some long-live charge carrier dynamics. In this dissertation, I demonstrate that the micrometer scale mapping between PPM images and FLIM images bridges the monitoring of charge carrier behaviors in different timescales and gives us a more complete picture of localized charge carrier dynamics.

### 1.5.1 Nonlinear optical interactions

Pump probe microscopy utilizes various nonlinear optical interactions to monitor the charge carrier dynamics. Two laser pulses (pump and probe) are used to resolve electron population changes induced by these interactions. Figure 6 illustrates several common nonlinear optical interactions.

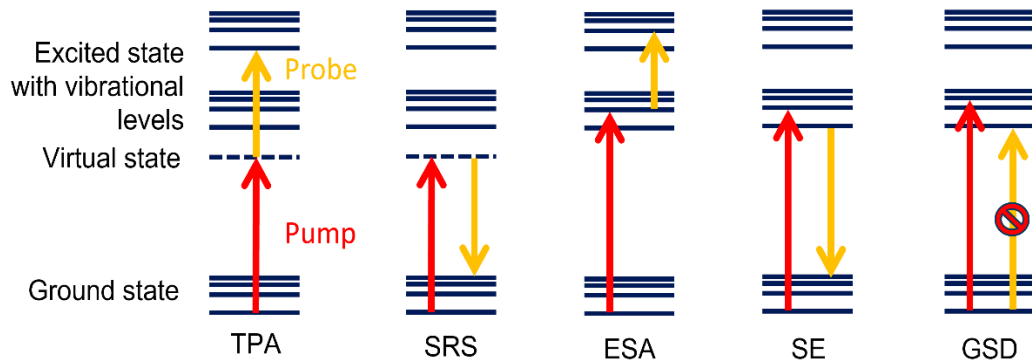


**Figure 6: Common nonlinear interactions used in pump probe microscopy. two-photon absorption (TPA), stimulated Raman scattering (SRS), excited state absorption (ESA), stimulated emission (SE) and ground state depletion (GSD).**

The intensity dependence of these nonlinear optical interactions on the pump and probe beams can be obtained by consider the nonlinear optical susceptibilities of the materials. The polarization  $\tilde{P}$  of the material system can be expressed with the optical susceptibilities as:

$$\tilde{P}(t) = \epsilon_0 [\chi^{(1)} \tilde{E}(t) + \chi^{(2)} \tilde{E}^2(t) + \chi^{(3)} \tilde{E}^3(t) + \dots] \quad (15)$$

where  $\epsilon_0$  is the permittivity of free space,  $\chi^{(1)}$  is the linear susceptibility,  $\chi^{(2)}$  and  $\chi^{(3)}$  are the second- and third-order nonlinear optical susceptibilities. Conventionally, the polarization can be split into the linear and nonlinear parts as:

$$\tilde{P}(t) = \tilde{P}^{(1)}(t) + \tilde{P}^{NL}(t) \quad (16)$$

where  $\tilde{P}^{(1)}(t)$  is the part that has linear dependence on the electric field. Typically, high order susceptibilities are much smaller than the linear susceptibility. Therefore, these nonlinear interactions are only significant under strong electric fields such as the electric field of laser pulses.

According to Maxwell's equations in an isotropic space with no free charge, the wave equation in a nonlinear material can be expressed as:

$$\nabla^2 \tilde{E}(t) - \frac{n^2}{c^2} \frac{\partial^2}{\partial t^2} \tilde{E}(t) = \frac{1}{\epsilon_0 c^2} \frac{\partial^2}{\partial t^2} \tilde{P}^{NL}(t) \quad (17)$$

where  $n$  is the refractive index of the material and  $c$  is the speed of light. The non-zero term containing  $\tilde{P}^{NL}$  acts as a driver of electromagnetic waves. By solving this equation, the modification of the electromagnetic waves due to the nonlinear polarization can be

determined. The real part of the nonlinear optical susceptibilities  $\chi^{(n)}$  in  $\tilde{P}^{NL}$  corresponds to a phase change to the waves and the imaginary part of them results to an absorption change to the waves.

Different nonlinear optical interactions are associated with different order of nonlinear optical susceptibilities, therefore, the intensity dependence of nonlinear optical interactions on the electromagnetic waves can vary. For example, the two-photon absorption shown in figure 6 is associated with the third order nonlinear optical susceptibility and the change of absorption coefficient  $\Delta\alpha$  of the probe beam depends on the intensity of the pump beam:

$$I_{pu} = \frac{1}{2} c \epsilon_0 n |E_{pu}|^2 \quad (18)$$

$$\Delta\alpha(\omega_{pr}) \propto \text{Im}\{\chi^{(3)}(\omega_{pr}, \omega_{pu}, -\omega_{pu})\} |E_{pu}|^2 \propto I_{pu} \quad (19)$$

where  $I_{pu}$  and  $E_{pu}$  represents the intensity and electric field of the pump beam.

$\chi^{(3)}(\omega_{pr}, \omega_{pu}, -\omega_{pu})$  stands for the third order nonlinear optical susceptibility corresponding to the absorption coefficient change of the probe beam. The absorption change  $\Delta A$  of the probe beam is written as:

$$\Delta A(\omega_{pr}) \propto I_{pr} \Delta\alpha(\omega_{pr}) \propto I_{pr} I_{pu} \quad (20)$$

where  $I_{pr}$  is the intensity of the probe beam. Equation 20 shows the change of the probe beam due to the presence of the pump beam. It is the principle of the pump probe microscopy.

### **1.5.2 Pump probe microscopy**

As discussed in the previous section, pump probe microscopy obtains molecular information by interrogating a variety of nonlinear optical interactions of the materials. The pump pulse excites electrons in the ground states and the following probe pulse can monitor transient electron dynamics involving electronic and vibrational energy states. By adjusting the difference of arrival time (time delay,  $t$ ) between the pump and the probe pulse, the time-resolved electron dynamics can be achieved. In addition to adjusting the time delay, tuning the pump and probe wavelengths provide a large parameter space to obtain molecular specificity.

The pump-probe signal detected in the PPM is the intensity change of the probe pulse with the pump pulse on and off. Different nonlinear optical interactions will result in different types of pump-probe responses (different signs and lifetimes). As shown in figure 6, due to the involvement of virtual energy states, two-photon absorption (TPA) and stimulated Raman scattering (SRS) will provide a pump-probe signal that is only significant within the time window when the temporal profile of the pump pulse and the probe pulse are overlapped. Processes such as excited state absorption (ESA), stimulated emission (SE), and ground state depletion (GSD) involve certain excited electronic energy states. The thermal relaxation time of these excited electrons can differ from sample to sample. It leads to different lifetimes of pump-probe signal. Figure 7 illustrates the time-resolved pump-probe signal of several common nonlinear optical

interactions. Additionally, the pump-probe signal of the state-filling effect (SFE), which is usually observed in the pump-probe measurement of perovskite thin films is plotted. The state-filling effect describes the absorption change of the probe beam due to the energy state occupations induced by the pump beam. Empty energy states previously available for the photon absorption of the probe beam are now partially filled by electrons excited by the pump beam. The population of the excited electrons  $\Delta N$  is linearly dependent on the intensity of the pump beam if a linear absorption of the pump beam is assumed. The absorption reduction of the probe beam can be expressed as:

$$\Delta A(t) \propto -\Delta N(t)I_{pu} \propto -I_{pr}I_{pu} \quad (21)$$

Since the state-filling effect involves electronic states, the corresponding pump-probe signal has a certain lifetime.

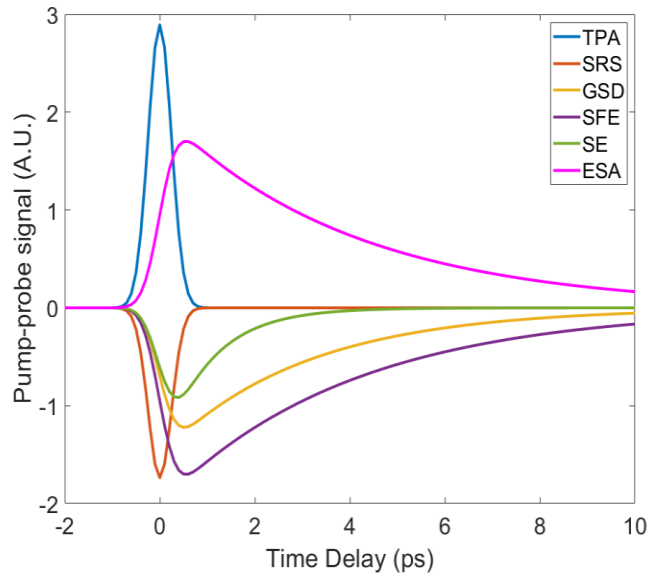


**Figure 7: Time-resolved pump-probe signal of common nonlinear optical interactions.**

As shown in figure 7, TPA and SRS exhibit different signs of pump-probe signal. For TPA, the absorption of the probe pulse is enhanced with the presence of the pump pulse. Therefore, if we measure the transmission of the probe pulse, we will obtain less intensity of the probe signal. It corresponds to a positive pump-probe signal in PPM analysis. Meanwhile, the sign of SRS depends on the wavelength of the pump and probe pulse. When the wavelength of the pump pulse is shorter than the probe pulse, the presence of the pump pulse will result in additional signal in the probe wavelength. In this case (same as shown in figure 6), more transmitted probe signal is measured, and the pump-probe signal is negative.

Note that different conventions of defining the sign of pump-probe signal are adapted by different research groups. Our group uses the positive sign for enhanced absorption of the probe pulse and the negative sign for reduced absorption of the probe pulse by the sample. Starting from Chapter 2, this convention will be used in all PPM analysis. For Section 1.3, the opposite sign will be used (positive for reduced absorption and negative for enhanced absorption) when the PPM work of other groups are reviewed.

### **1.5.3 Fluorescence lifetime microscopy**

Long fluorescence lifetime indicates low density of defects and possible long diffusion length of charge carriers in a perovskite thin film<sup>10</sup>. Both properties are associated with high PCE in perovskite solar cells. Therefore, fluorescence lifetime is an

important parameter for evaluating the quality of a perovskite thin film<sup>10</sup>. FLIM is a powerful method to obtain fluorescence lifetime with micrometer spatial resolution. It is mainly based on the time-correlated single photon counting (TCSPC) technique<sup>28-30</sup>. In the TCSPC technique, single photons of a periodic light signal are detected by a photomultiplier tube (PMT). Usually, the light signal has high repetition rate, and the intensity of the signal is low enough to satisfy the assumption that the probability of detecting one photon in one signal period is low and the change of detecting more than one photon in one signal period can be neglected. Therefore, instead of measuring the fluorescence intensity at different time delays (time difference between light excitation and the detection of fluorescence signal), the TCSPC technique can count the distribution of photons arriving at different time delays over many signal periods (figure 8a). Fluorescence waveforms can be reconstructed based on the time-correlated photon distribution (figure 8b) and the fluorescence lifetime can be extracted from it.

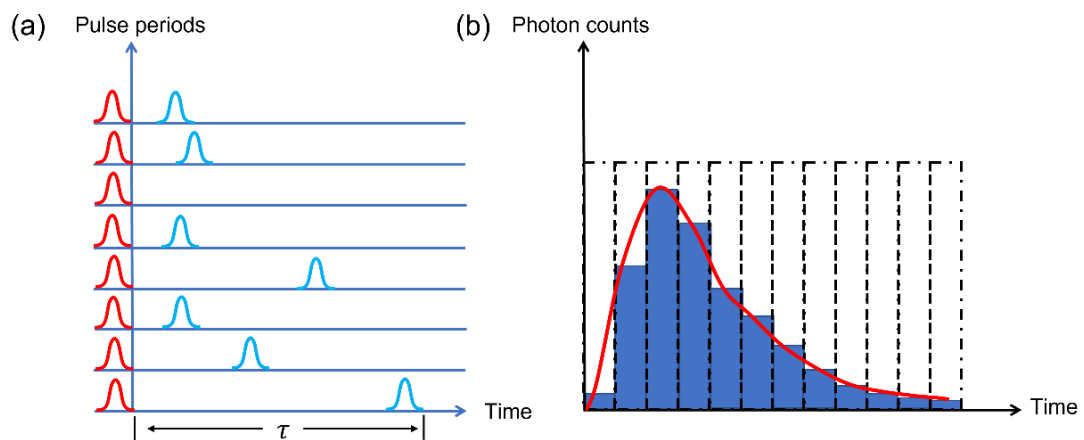


**Figure 8: Principle of the time-correlated single photon counting technique. (a) Red pulses stand for the light signal in each period. Blue pulses stand for single**

photons detected in some periods. The time difference ( $\tau$ ) between a light signal and a detected single photon is used to form a time-correlated photon distribution. (b) The red curve is the reconstructed fluorescence waveform based on the time-correlated photon counting histogram.

In principle, the time resolution of TCSPC is not limited by the bandwidth of the detector, like seen with an analog signal recording technique. Instead, it depends on how accurate the time of a single photon detection can be determined, which usually has much better time resolution than the analog recording technique<sup>31</sup>. In FLIM, in addition to photon detection with TCSPC technique, galvo mirrors scan the laser beam across the sample so that the spatial resolution of fluorescence signal is also obtained.

### ***1.6 Progress of pump probe microscopy studies on perovskite thin films***

Pump probe microscopy has demonstrated its capability of investigating perovskite thin films in the past 5 years<sup>4-6, 32, 33</sup>. Many photovoltaic properties of perovskite thin films have been revealed by several research groups. In this section, I will summarize the recent progress on perovskite thin films study by PPM.

As mentioned in previous section, band gap energy and defects are important for the PCE and charge carrier lifetime of perovskite thin films. These properties are also critical to the choice of pump and probe wavelengths in PPM. Figure 9a shows the linear absorption spectrum and the fluorescence emission spectrum of MAPbI<sub>3</sub> thin films. Photons with energy higher than the band gap energy are likely to be absorbed by the thin film and excited electrons tend to relax to the conduction band edge before

radiatively recombining with holes in the valence band. Therefore, the rapid decrease in the linear absorption spectrum and the sharp peak (760nm) in the emission spectrum together identify the band gap energy of MAPbI<sub>3</sub> thin films at around 1.63eV. Figure 9b shows the morphology of MAPbI<sub>3</sub> thin films with granular structure. Defects are usually associated with structural disorder from pin holes and grain boundaries<sup>10, 34</sup>.

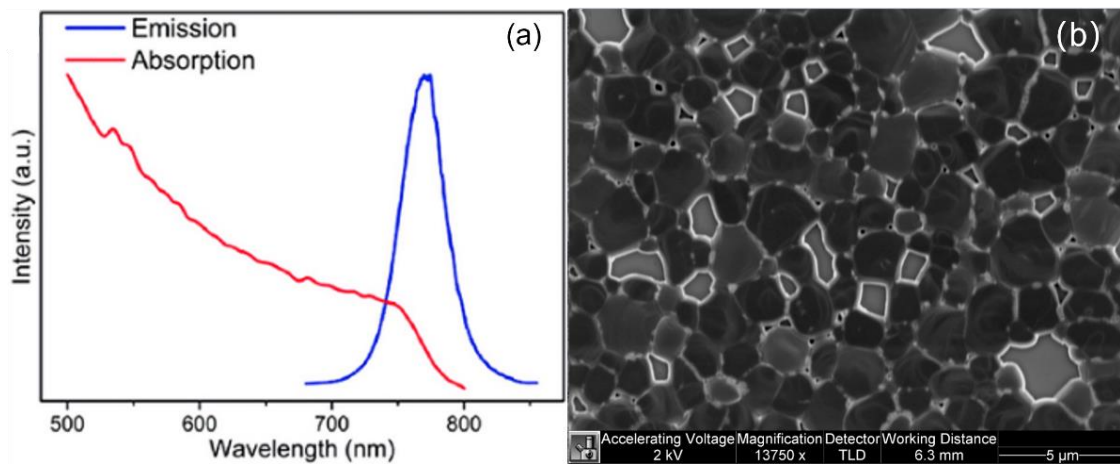


**Figure 9: Linear absorption and fluorescence emission spectrum and SEM image of the MAPbI<sub>3</sub> thin film. (a) The emission peak is centered at 760nm (b) SEM image of the MAPbI<sub>3</sub> thin film having granular structure. Gray regions with bright edge are pin holes with little MAPbI<sub>3</sub>.**

Once the band gap energy is determined, different pump and probe wavelength combinations can be designed to investigate the charge carrier dynamics. Typically, the pump wavelength is chosen to provide photons having energy greater than the band gap energy so that a population of charge carriers is created after the pump excitation. The probe wavelength can be chosen to either probe the absorption change induced by the pump beam<sup>6, 35</sup> or probe the index change induced by the pump beam<sup>36</sup>. To probe the absorption change induced by the pump beam, the probe wavelength needs to excite

electrons slightly above the band edge. Electrons excited by the pump beam fills a portion of available energy states near the band edge so that the absorption of the probe beam will be reduced. Meanwhile, if the probe wavelength is chosen to provide energy much lower than the band gap energy, no significant absorption will occur. However, the pump excitation will result in an index change of perovskite thin films. The transmission of the probe beam will therefore be affected<sup>36</sup>.

In the work of Libai Huang's group<sup>35</sup>, MAPbI<sub>3</sub> thin films with granular structure are investigated with a 630nm pump beam and two color of probe beams: 755nm (photon energy larger than the band gap energy) and 785nm (photon energy slightly less than the band gap energy). Both probe wavelengths show a bleaching signal ( $\Delta T > 0$ , figure 10a, b). Note that the sign convention of enhanced absorption ( $\Delta T < 0$ ) and reduced absorption ( $\Delta T > 0$ ) is used here. The bleaching signal of 755nm and 785nm probe wavelengths are due to the state filling effect of band edge energy states and sub-bandgap energy states respectively. Since sub-bandgap states are trapping states often associated with defects and whose energy are slightly less than the bandgap energy, regions having strong bleaching signal from the 785nm probe are likely to have more defects.

As shown in figure 10a and b, the dashed line represents the edge of a single grain in the MAPbI<sub>3</sub> thin film. In the grain boundary, less bleaching signal from the 755nm probe and more bleaching signal from the 785nm probe is observed. This

observation can be explained by state filling effect of abundant sub-bandgap states around the grain boundary. After pump excitation and thermalization, electron accumulation at band edge energy states will be reduced due to available states below the band edge. Therefore, the bleaching effect at the band edge is less pronounced while the bleaching effect below the band edge becomes more significant due to the state filling effect of sub-bandgap states. Additionally, the lifetime of pump-probe signal at the grain boundary when probing at 755nm is slightly shorter than that at the grain interior (figure 10c). It can be associated with more recombination channels at the grain boundary. This observation again supports that the grain boundary contains more sub-bandgap states than the grain interior.

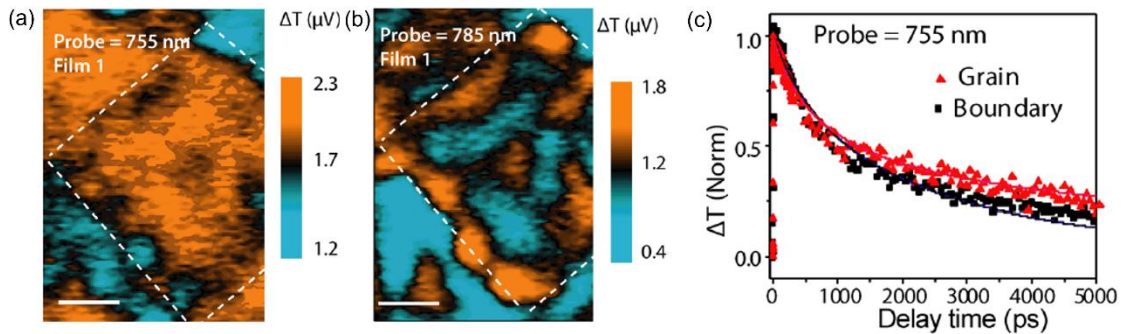


**Figure 10: Pump probe microscopy images of MAPbI<sub>3</sub> thin films with different probe wavelengths. Pump probe microscopy images of 755nm probe beam (a) and 785nm probe beam (b) taken at  $t = 10 ps$  time delay. Two images show the same region of interest. The white dash line indicates a single grain in the MAPbI<sub>3</sub> thin film and scale bars are  $1\mu m$ . (c) Carrier dynamics at 755nm within a grain and at the grain boundary. Solid lines are fitted to a time-dependent carrier density function considering both recombination and carrier diffusion. Adapted with permission from J. M. Snaider, Z. Guo, T. Wang, M. Yang, L. Yuan, K. Zhu and L. Huang, ACS Energy Letters 3 (6), 1402-1408 (2018). Copyright 2018, American Chemical Society.**

Their group also investigates the diffusion coefficient ( $D$ ) of hybrid perovskite thin films. To determine  $D$ , a slight modification of the scanning mechanism of PPM must be made. Typical PPM uses a pair of galvo mirrors to scan the spatially overlapping pump and probe beam across the sample to obtain spatially resolved pump-probe images. In this case, the pump beam is fixed at one position and only the probe beam is scanned. Therefore, only the fixed position is excited by the pump beam. After excitation, excited electrons start to diffuse to surrounding areas having less electron density in the conduction band. The scanning probe beam then measures the diffusion process by the spatial expansion of pump-probe signal<sup>35, 37</sup> (figure 11). For a two-dimension diffusion,  $D$  can be calculated by  $\sigma_t^2 - \sigma_0^2 = 4Dt$  where  $\sigma^2$  represents the variance of pump-probe signal with Gaussian shape at different time delays ( $t$ ). This method is also used to evaluate the carrier transport across grain boundaries<sup>35</sup>, lateral heterojunctions<sup>38</sup>, and the near-surface carrier diffusion enhancement by phenethylammonium functionalization<sup>39</sup>.

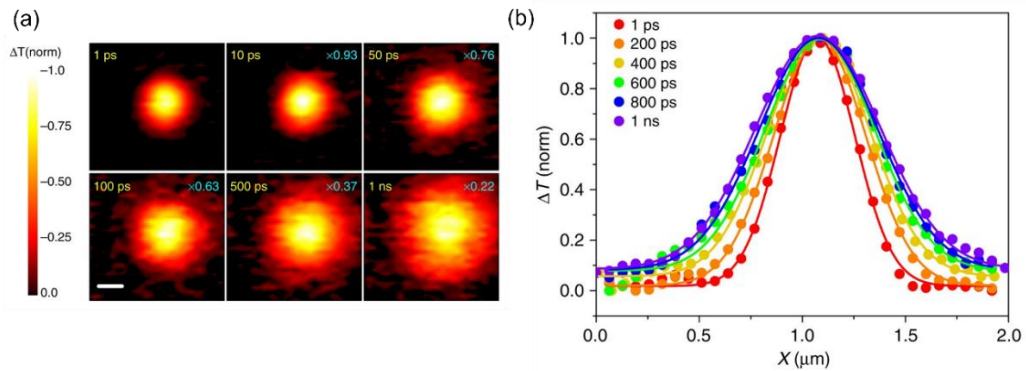


**Figure 11: Pump probe microscopy images of the carrier transport in a hybrid perovskite thin film. (a) The 2D imaging of the carrier density profile in MAPbI<sub>3</sub> at**

**different pump–probe time delays. For delay time >1 ps, the signal maximum in each image was normalized to the signal maximum at 1 ps. The scale bar in the figure is 300 nm. (b) Scans of excited-state density profile projected along one dimension. Data are acquired at different time delays. The profiles are fitted by Gaussian functions. Adapted with permission from Z. Guo, J. S. Manser, Y. Wan, P. V. Kamat and L. Huang, Nature Communications 6 (1), 7471 (2015). Copyright 2015, The Authors.**

Although the wavelength of the probe beam is usually chosen to directly monitor the charge carrier behavior near the band edge, multiple optical responses such as band gap renormalization<sup>40</sup>, band-filling<sup>41</sup>, and line broadening<sup>42</sup> might complicate the dynamics of carriers near the band edge. In the work of Erik M. Grumstrup's group, they select the probe wavelength to have photon energy well below the band gap energy. In such case, there is no significant probe absorption and majority of the complicated optical responses mentioned above are avoided. It is the refractive index change due to the presence of excited charge carriers that is probed. To a good approximation, the refractive index change should have a linear dependence of excited charge carrier density<sup>43</sup>. Without the presence of the pump beam, the image formed by the probe beam will show interference fringes due to the variation of the thickness of the perovskite thin films. When the pump beam is present, the interference fringes will shift due to the change of films' refractive index change. Figure 12 shows the original and shifted interference fringes of a hypothetical domain. A predicted pump-probe signal is determined by the difference between the original and shifted fringes<sup>36</sup>. Since the original fringes can be determined with the help of atomic force microscopy (AFM)

which provide the topography of materials, the shifted fringes and the change of local refractive index can be obtained by the pump-probe signal.

Since the change of refractive index can be directly related to the charge carrier dynamics, the time-resolved charge carrier dynamics can be obtained by tuning the arrival times of pump and probe pulses just like the conventional PPM. Combining this method with a modified pump probe microscopy technique similar to what we mention above (fix the pump beam and solely scan the probe beam across the sample), more fundamental properties of perovskite thin films such as the carrier mobility, effective mass and mean scattering time can be determined<sup>36</sup>.

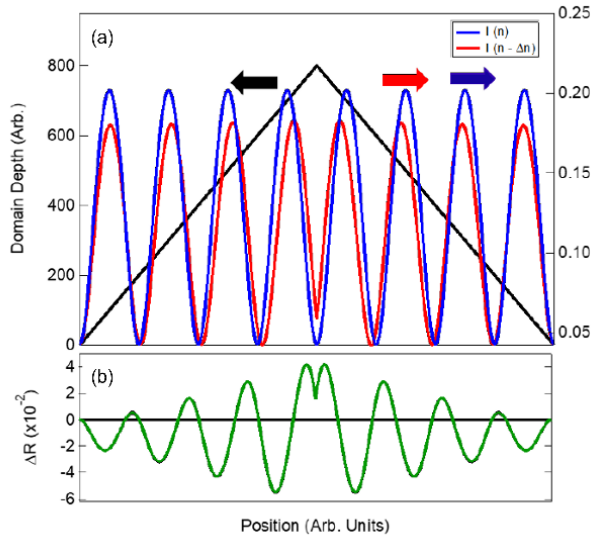


**Figure 12: Effects of a refractive index change in pump probe reflection imaging. (A) Profile of hypothetical domain (black line) overlaid with two predicted reflectivity traces assuming different refractive indices. A decrease in the refractive index (red vs. blue traces) is accompanied by lateral shifts of the interference fringes. Also note the mean decrease in amplitude between the blue and red traces. (B) Predicted pump-probe signal,  $[I(n - \Delta n) - I(n)]$ , determined from the two traces shown in panel A. Adapted with permission from A. H. Hill, C. L. Kennedy, E. S.**

**Massaro and E. M. Grumstrup, *The Journal of Physical Chemistry Letters* 9 (11), 2808-2813 (2018). Copyright 2018, American Chemical Society.**

Although pump probe microscopy studies on perovskite thin films have achieved certain success, the ultrafast charge carrier dynamics ( $< 1$  ps) and the spatial heterogeneity of charge carrier dynamics have not yet been fully understood due to the involvement of multiple optical processes. Attempts to spatially correlate the time-integrated fluorescence microscopy and pump probe microscopy<sup>6</sup> have been made by Mary Jane Simpson from Oak Ridge National Laboratory. They discovered spatial heterogeneity of time-integrated fluorescence intensity and spatially uniform pump-probe signal<sup>6</sup> at 5 ps time delay. The uniform pump-probe signal at early time (in picosecond scale) indicates a uniform excitation from the pump beam. The heterogeneity of time-integrated fluorescence intensity is associated with trapping states which will alter the local quantum efficiency of the sample.

In addition to the work mentioned above, many improvements have been made to broaden the usage of PPM. Electron backscattering diffraction (EBSD) can be coupled with PPM to correlate the local crystal quality and charge carrier transport in lead halide perovskite thin films<sup>44</sup>. A modified PPM setup with the broadband probe beam can push the study of hot carrier cooling process in the perovskite thin films even further by providing temporal, spatial and spectral resolution at the same time<sup>45</sup>.

Despite the progress of PPM on perovskite thin films described above, spatial heterogeneity of charge carrier dynamics is still not completely understood. For

example, the correlation between fluorescence signal and pump-probe signal is absent and the ultrafast charge carrier dynamics is overlooked in most of the studies. In this thesis, the correlation between fluorescence signal and pump-probe signal is discovered with micrometer spatial resolution and the ultrafast charge carrier dynamics within the first picosecond is discussed.

### **1.7 Thesis outline**

In chapter 2, I demonstrate the ability of PPM to reveal the ultrafast charge carrier dynamics with sub-micrometer spatial resolution. Adapted phasor analysis is used to distinguish the spatial heterogeneity of charge carrier dynamics found in PPM and FLIM images. Sub-micrometer scale mapping between phasor and SEM images is achieved. The heterogeneous charge carrier dynamics are associated with the spatial defects and structural disorder.

In chapter 3, I introduce a model to decompose the pump-probe and fluorescence signal in different time regions to better understand the charge carrier dynamics. The correlation between PPM and FLIM in the same region is analyzed. Spatial heterogeneity of charge carrier dynamics is related to visible and invisible defects by mapping PPM and FLIM images to the morphology of MAPbI<sub>3</sub> perovskite thin films.

In Chapter 4, the ultrafast charge carrier dynamics is related to the hot carrier cooling process. I demonstrate the hot carrier cooling process can be monitored by multi-wavelength pump probe microscopy. The time-resolved local electron

temperature is obtained with micrometer spatial resolution by analyzing local pump-probe spectra at different time delays.

In Chapter 5, I discuss the potential of using PPM to investigate the impact of degradation and different microstructures of the MAPbI<sub>3</sub> thin films on the samples' charge carrier dynamics.

## **2 Probing the spatial heterogeneity of charge carrier dynamics in $\text{CH}_3\text{NH}_3\text{PbI}_3$ perovskite thin films with femtosecond time-resolved nonlinear optical microscopy**

The spatial heterogeneity of perovskite thin films has reported by multiple research groups<sup>6, 44</sup>. It is closely related with various defects in the thin films<sup>10, 32, 35, 44</sup>. The charge carrier dynamics change due to such spatial heterogeneity plays an important role in PCE of the thin films. However, the difference of charge carrier dynamics between heterogeneous regions is not fully understood. Since the study of ultrafast charge carrier dynamics and correlation between different charge carrier dynamics are limited by the temporal and spatial resolution, the ability of PPM to monitor various nonlinear optical interactions raised by the change of charge carrier population with sub-picosecond temporal resolution and sub-micrometer spatial resolution makes PPM a suitable tool for such study. Combining PPM with FLIM, the time scale of monitoring charge carrier population can range from picoseconds to nanoseconds and the different recombination processes (radiative and non-radiative) can be distinguished. In this chapter, I demonstrate the correlation between spatial heterogeneity of  $\text{MAPbI}_3$  thin films' morphology and the charge carrier dynamics. The correlation between the charge carrier dynamics in different time scales is also revealed.

## 2.1 Optical microscopy setup

### 2.1.1 Pump probe microscopy setup

Figure 13 shows our PPM setup. A mode-locked Ti:Sapphire laser (Chameleon, Coherent) generates a laser pulse train with 80MHz repetition rate. The pulse train is split into the pump beam (red) and the probe beam (yellow). The pump beam is modulated by an acousto-optic modulator (AOM) with a square function at 2MHz. The probe beam is sent to an optical parametrical oscillator (Mira-OPO, Coherent) for wavelength tuning. The optical path length of the pump beam is adjusted with a translational stage before spatially overlapped with the pump beam. A beam splitter is used to spatially combine the pump and probe beams.

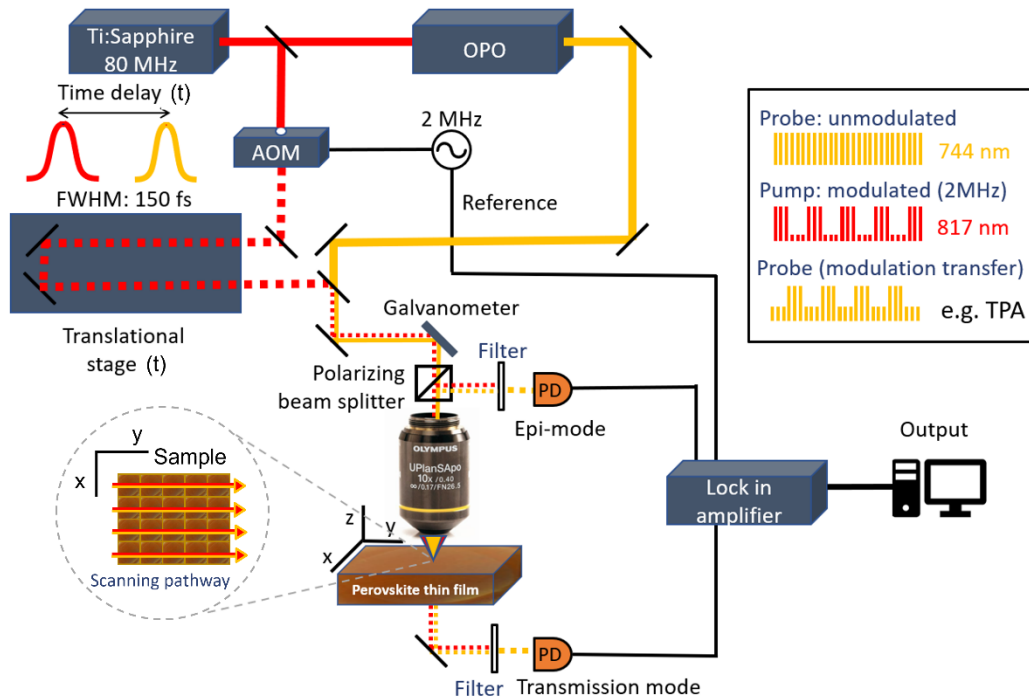


Figure 13: Pump probe microscopy setup. The pump and probe beams are shown in red and yellow respectively. An AOM is used to modulate the pump beam

at 2MHz. Pump and probe beams are combined and focused to the sample. A pair of Galvo mirrors scan beams across the x-y plane of the sample. Nonlinear optical interactions involving both beams transfer the pump beam modulation to the probe beam. Spectral filters are applied before the photodiode (PD) to block the pump beam and selectively measure the probe signal. A lock-in amplifier is used to extract the intensity modulation of the probe signal. Inset shows the modulation transfer when TPA happens.

An objective lens is used to focus the spatially overlapped beams on the sample and a pair of Galvo mirrors scan the two beams together across the x-y plane of the sample. Multiple spectral filters are placed before the photodiodes (PDA55, Thorlabs) to filter the pump beam and selectively pass the probe beam. The intensity modulation of the probe beam due to the presence of the pump beam (via nonlinear optical interactions, TPA is shown in Figure 13: Pump probe microscopy setup. as an example) is extracted by a lock-in amplifier (SR844, Stanford Research). By tuning the length of the translational stage, the difference of arrival times between each pump pulse and probe pulse (time delay,  $t$ ) to the sample can be controlled and a time-resolved trace of pump-probe signal can be obtained. Figure 14 shows typical time-resolved pump-probe signal in MAPbI<sub>3</sub> thin films and a spatial image of pump-probe signal at a specific time delay.

Our PPM setup has two detection modes: trans-mode and epi-mode. The trans-mode measures the intensity changes of the transmitted probe beam, and the epi-mode detects the changes of the depolarized back-scattered probe beam reflected by a beam splitter. Depending on the transmittance of the sample, one of the detection modes will be used. Our setup also utilizes two scanning modes: time delay scan and depth scan.

For the time delay scan,  $\tau$  is varied to obtain time-resolved pump-probe traces across the sample with fixed focal position as shown in figure 14. For the depth scan,  $\tau$  is fixed at a certain value and the focal position is scanned through different depths. A depth-resolved pump-probe trace across the sample at a fixed time delay can be obtained with this scanning mode. In this chapter, all the pump-probe measurements of perovskite thin films are acquired with time delay scan in trans-mode.

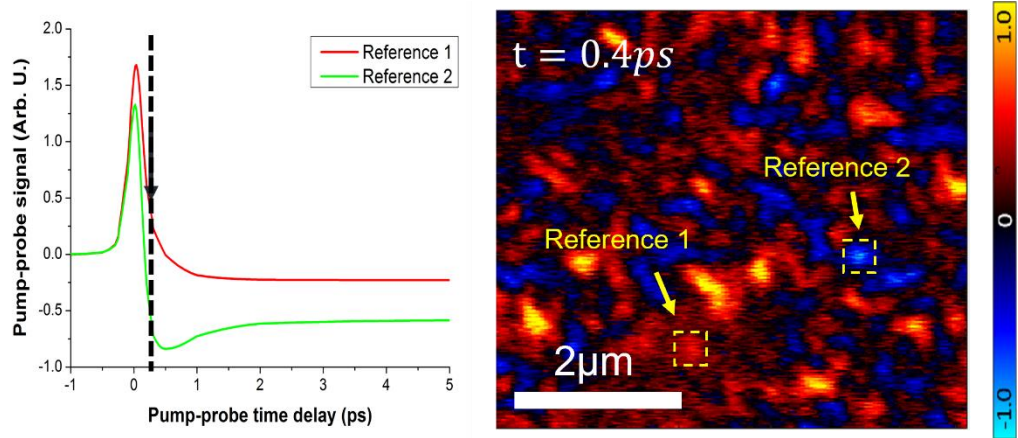


**Figure 14: Time-resolved Pump-probe traces and pump-probe image at fixed time.** (a) Two typical pump-probe traces in MAPbI<sub>3</sub> thin films. They show the averaged pump-probe trace of regions reference 1 and 2 in (b) respectively. The dash line and arrow show the pump-probe signal of two regions at  $t = 0.4\text{ps}$  time delay. (b) The pump-probe image at  $t = 0.4\text{ps}$  time delay. The color bar shows the intensity of pump-probe signal with arbitrary unit ranging from -1 to 1. Reference 1 and 2 show regions having different signs of pump-probe signal at  $t = 0.4\text{ps}$ . It indicates the spatial heterogeneity of pump-probe signal across the sample.

### 2.1.2 Noise analysis of the pump probe microscopy

The amplitude of the detected pump-probe signal, which relies on the nonlinear optical interactions, usually is very small compared to the unmodulated probe signal when the pump beam is absent. The amplitude of the pump-probe signal, which is the

amplitude of the modulation transferred to the probe beam, is approximately  $10^{-5}$  of the unmodulated probe signal. To extract such small modulation from the detected signal, the noise contributions need to be carefully considered. The major noise contributions are the electronic noise, the relative intensity noise, and the shot noise. Since the relative intensity noise is reported to be 0.15% of the laser intensity out of a Ti:sapphire modelocked laser<sup>46</sup>, it is overwhelming for the transferred modulation. However, the relative intensity noise is frequency-dependent, its contribution to the detected signal is negligible above 1MHz. Therefore, a 2MHz modulation is chosen for the pump beam modulation to eliminate the impact of the relative intensity noise. The electronic noise can be minimized by amplifying the detected signal via an amplified photodiode since it is irrelevant to the amplitude of the detected signal. Additionally, taking more average of the detected signal can efficiently reduce the noise.

### **2.1.3 Fluorescence lifetime microscopy setup**

Our FLIM setup is shown in figure 15, the pulse train generated by the Chameleon laser is split into the excitation beam and the reference beam. The reference beam sends the time reference of each pulse to a TCSPC module (SPC-630, Becker & Hickl). The excitation beam is focused on the sample by an objective lens and the fluorescence signal is reflected by a dichroic mirror and detected by a PMT. Multiple filters can be applied before the PMT to selectively collect fluorescence signal of certain wavelength. The TCSPC module outputs time-resolved fluorescence traces by counting

the fluorescence signal at different arrival times compared to reference pulses. Again, scanning is done by a pair of Galvo mirrors.

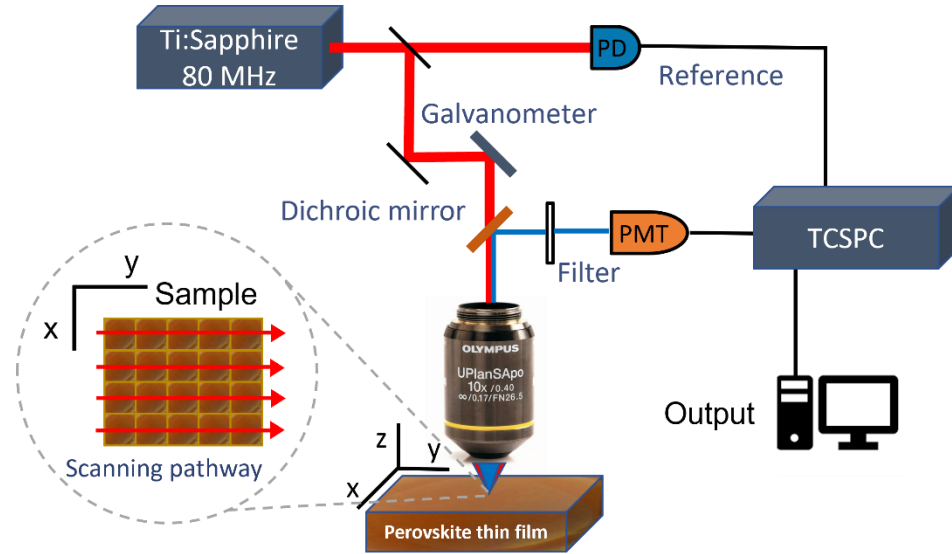


**Figure 15: Fluorescence lifetime microscopy setup.** The reference and excitation beams are shown in red, and the fluorescence signal is shown in blue. Spectral filters are used to filter out the excitation beam. A PMT is used to detect the fluorescence signal. A time-resolved fluorescence trace is obtained by comparing the arrival time between fluorescence signal and the laser pulses of the reference beam.

### 2.1.4 Phasor analysis

Phasor analysis is commonly used in FLIM for fast differentiation of various fluorophores<sup>47, 48</sup>. It is a single frequency Fourier transformation ( $\omega$  as a free parameter) that can project a decay trace having multiple exponential decays  $I(t)$  into a phasor point (figure 16a) with the real part ( $g$ ) as x coordinate and the imaginary part ( $s$ ) as y coordinate:

$$g(\omega) = \frac{\int_0^{\infty} I(t) \cos(\omega t) dt}{\int_0^{\infty} I(t) dt} \quad (22)$$

$$s(\omega) = \frac{\int_0^{\infty} I(t) \sin(\omega t) dt}{\int_0^{\infty} I(t) dt} \quad (23)$$

Any unipolar signal is bounded by semicircles on the first quadrant (positive signal) and the third quadrant (negative signal). The former is known as the universal semicircle. All phasor points of single exponential decay traces will sit on the semicircle and the linear combination of two exponential decay traces will lead to a phasor point on the line connecting two end points on the semicircle (figure 16a).

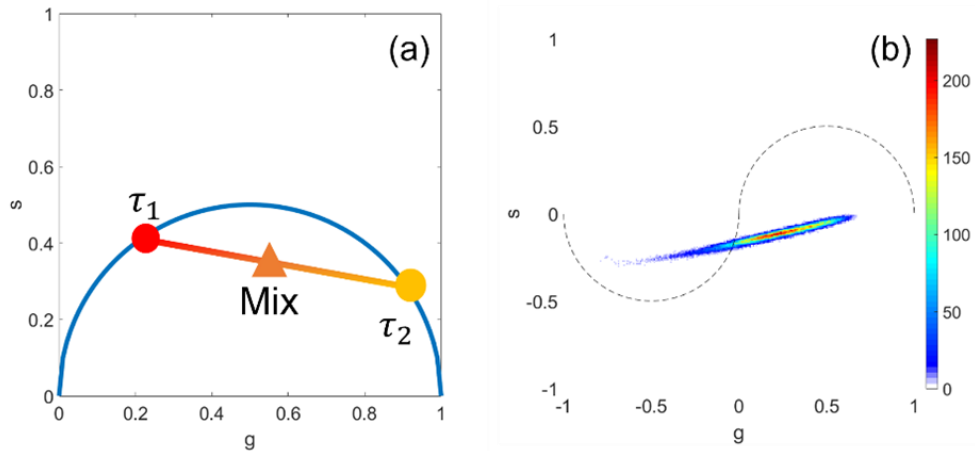


**Figure 16: Phasor plots. (a) Phasor plot of exponential decay traces. Two end points on the semicircle correspond to two single exponential decay traces:  $I_1 = A \exp(-t/\tau_1)$ ,  $I_2 = B \exp(-t/\tau_2)$ . The mix point indicates a decay trace with mixture of two single exponential components:  $I_{mix} = A' \exp(-t/\tau_1) + B' \exp(-t/\tau_2)$ . (b) Phasor plot of a pump probe microscopy image. The color bar shows the density of phasor points.**

In pump probe microscopy, a bipolar signal is not unusual (mixture of TPA and GSD for example). In order to avoid singularities and an unbound result<sup>49</sup>, the phasor analysis is adjusted:

$$g(\omega) = \frac{\int_0^{\infty} I(t) \cos(\omega t) dt}{\int_0^{\infty} |I(t)| dt} \quad (24)$$

$$s(\omega) = \frac{\int_0^{\infty} I(t) \sin(\omega t) dt}{\int_0^{\infty} |I(t)| dt} \quad (25)$$

Now, the phasor point can span the between two semicircles when projecting pump probe signals into the phasor plot. When applying phasor analysis to each pixel of pump probe microscopy images, their phasor distribution will be shown with a color scale reflecting the phasor histogram (figure 16b).

## **2.2 Charge carrier density calculation**

Due to the dependence of different recombination processes on the charge carrier density, a calculation for pump induced charge carrier density can indicate the dominant recombination process. In our PPM experiment, the wavelengths of the pump and probe beams are chosen to be 817nm (1.52eV photon energy) and 745nm (1.66eV photon energy) respectively due to the limited wavelength combination available in our system. Since the band gap energy of MAPbI<sub>3</sub> thin films is 1.63eV, a single photon from the 817nm pump beam does not provide enough energy to excite electrons to the conduction band from the valence band. Therefore, two-photon excitation process is utilized to excite electrons: two pump photons together provide energy for a single electronic excitation. Since the majority of excited electrons will thermalize to the energy states near the band edge, the probe beam is selected to have photon energy slightly higher than the band gap energy to measure the charge carrier population.

To calculate the initial charge carrier density excited by the pump beam, the nonlinear absorption coefficient ( $\beta$ ) is considered. For MAPbI3 thin films,  $\beta$  is reported to be<sup>50</sup>  $5 \times 10^{-7} \text{ cm/W}$ . The power ( $P$ ) of the pump beam used in our experiment is 0.3mW and the excitation area ( $A$ ) is approximately  $3 \times 10^{-8} \text{ cm}^2$ . The peak intensity is:

$$I_p = \frac{P}{A} \times \frac{T_s}{T_p} = 8.3 \times 10^8 \text{ W/cm}^2 \quad (26)$$

where  $T_s = 12.5\text{ns}$  is the time of a single pulse period and  $T_p = 150\text{fs}$  is the time of a single pulse duration. The penetration depth ( $Z_p$ ) can be calculated as:

$$Z_p = \frac{1}{e\beta I_p} = 8.8\mu\text{m} \quad (27)$$

where  $e$  is the Euler's number. The thickness of MAPbI3 thin films ( $Z_m$ ) is usually around 300nm which is much smaller than the penetration depth. Therefore, the nonlinear absorption of the pump beam can be simplified as:

$$\Delta E = \beta Z_m I_p^2 T_p = 1.56 \times 10^{-6} \text{ J/cm}^2 \quad (28)$$

The initial charge carrier density can be calculated as:

$$\frac{\Delta E}{2\omega\hbar Z_m} = 10^{17} / \text{cm}^3 \quad (29)$$

the coefficient 1/2 in the equation indicates the two-photon excitation. According to previous studies<sup>51, 52</sup>, the trap-assisted recombination processes is the dominant contribution to the change of charge carrier population with the initial charge carrier density calculated above.

## 2.3 Experimental results

### 2.3.1 Pump probe microscopy images of MAPbI<sub>3</sub> thin films

Figure 17 shows the PPM image of a MAPbI<sub>3</sub> thin film. Traditional pump probe spectroscopy averages the pump-probe signal across the whole region (average signal in figure 17). It fails to reveal the different pump-probe signals shown at reference 1 and 2 and the spatial heterogeneity of the signals is overlooked. PPM, in another hand, demonstrates its ability to study the spatial heterogeneity of charge carrier behaviors.

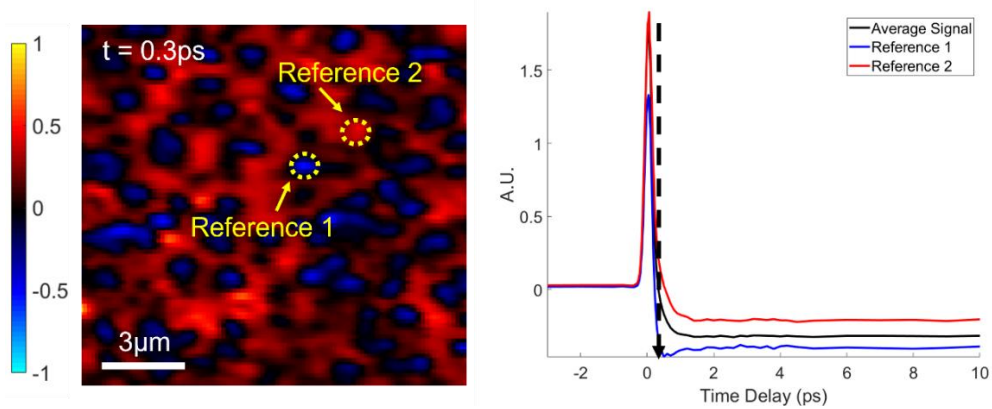


**Figure 17: Pump probe microscopy image of MAPbI<sub>3</sub> thin films. The left image shows the pump-probe image at  $t = 0.18\text{ps}$  time delay and the color bar shows the intensity of local pump-probe signal. Complete time-resolved pump-probe traces of reference 1 and 2 are shown on the right. The average trace across the whole region is also plotted. Black dashed line indicates the time delay that corresponds to the left image.**

In figure 17, all time-resolved pump-probe traces of MAPbI<sub>3</sub> thin films share the same instantaneous absorption peak that centers at  $t = 0\text{ps}$  and a long-lived negative signal. However, the sub-picosecond behavior of the pump-probe traces varies in different investigated regions. The trace of reference 1 shows a rapidly decaying

negative signal within the first picosecond, which is absent in the trace of reference 2. This rapidly decaying negative signal competes with the instantaneous positive peak and leads to a steeper trace within the first picosecond. Therefore, the spatial heterogeneity of charge carrier behaviors can be identified by investigating the spatial image of pump-probe signal at early time delays. When the time delay between pump and probe pulses are large, the dominant pump-probe signal is a long-lived negative signal. Such long-lived negative signal might consist of several contributions. The fluorescence signal with lifetime of nanosecond scales, which is observed by FLIM in the same sample, can contribute to the detected probe signal since the wavelength of the emission photons is close to the probing wavelength (both have photon energy close to the band gap energy). Therefore, it counts as a long-lived negative signal. The state-filling effect near the band edge and the ground state bleaching can reduce the absorption of the probe beam and lead to a long-lived negative signal if the lifetime of the charge carrier recombination is long enough. Since the amplitude of such long-lived negative signal reduces rapidly if probing with shorter wavelengths (details will be shown in the chapter 4), the contribution from the ground state bleaching is not significant. Additionally, since most of the trap-assisted recombination, which is the dominant recombination process with current power combination of the pump and probe beams, is a non-radiative recombination process. The contribution of the radiative recombination to the change of the detected probe signal is less pronounced. Therefore,

the dominant contribution of this long-lived signal is likely to be the bleaching signal raised by the state-filling effect near the band edge. Since most of the pump excited electrons will thermally relax to the band edge for long time delays, the long-lived bleaching signal represents the pump induced charge carrier population.

To better understand the charge carrier dynamics behind the pump-probe trace, the intensity dependence of different nonlinear optical interactions can be utilized. Such intensity dependence can be analyzed by carrying out a power study of the pump-probe signal.

### **2.3.2 Power study of the pump-probe signal**

A series of PPM measurements with different pump and probe powers are recorded. Figure 18 shows the intensity dependence of pump-probe signal at two different regions. Each region corresponds to a type of pump-probe trace discussed in the previous section. The left figure shows the trace with no rapidly decaying negative signal and the right figure shows the trace with such signal. For the instantaneous peak, only the trace without the rapidly decaying negative signal is chosen to study the intensity dependence. It is because the competition between the peak signal and the rapidly decaying negative signal will influence overall signal and make it hard to solely investigate the intensity dependence of the peak signal. For the long-lived bleaching signal, the trace with the rapidly decaying negative signal is chosen, since traces without

the rapidly decaying negative signal tend to have a small long-live bleaching signal, which influence the accuracy of the analysis of the intensity dependence.

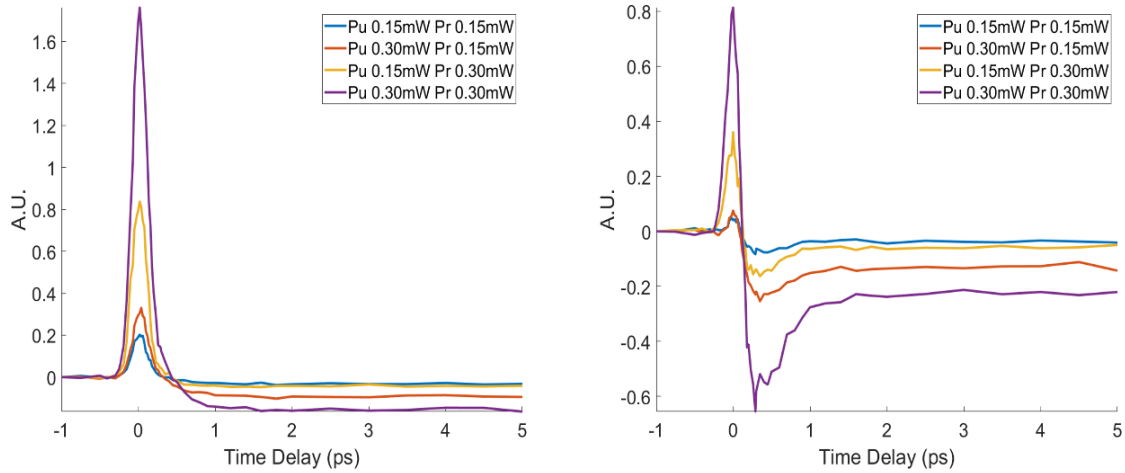


**Figure 18: Power study of two types of pump-probe traces. The left figure shows the power study of an investigated region that do not have a rapidly decaying negative component and the right figure shows a region that has a rapidly decaying negative component. The pump and probe powers are selected to be either 0.15mW or 0.3mW.**

To examine the intensity dependence of these two signals, we assume that instantaneous peak is dominant at 0ps, and the long-lived bleaching signal is dominant at longer time delays ( $t > 1.5\text{ps}$ ). In the next chapter, the reasoning of this assumption will be given. The ratio between the peak value of the pump-probe signal at 0ps from traces without the rapidly decaying negative signal is listed in table 1. The ratio between the mean value of the pump-probe signal ranging from 1.5ps to 5ps from traces with the rapidly decaying negative signal is also shown.

**Table 1: Intensity dependence of two charge carrier dynamics**

Pump power/Probe power (mW)	0.15/0.15	0.30/0.15	0.15/0.30	0.30/0.30
Instantaneous peak signal ratio	1	1.63	4.1	8.7
Long-lived bleaching signal ratio	1	3.6	1.6	6.3

From table 1, we can estimate roughly a linear intensity dependence of the pump beam and a quadratic intensity dependence of the probe beam for the instantaneous peak signal. For the long-lived bleaching signal, the intensity dependence is quadratic for the pump beam and linear for the probe beam. (More power combinations are used to verify this intensity dependence in Appendix A).

Figure 19 shows a possible model to explain the charge carrier dynamics behind these intensity dependences. For small time delays ( $t < 0.5\text{ps}$ ), the arrival time of pump and probe beams are very close so that the excitation processes involving multiple pump and probe photons become possible. Although the two-photon absorption involving one pump photon and one probe photon is expected, the intensity dependence for the instantaneous peak of the pump-probe suggests the dominant contribution is from a three-photon absorption process (figure 19a). The three-photon absorption might be explained as an electron in the conduction band excited by absorbing one pump photon and one probe photon is further excited to a higher energy band by absorbing an additional probe photon. Since a single photon from the pump beam is not able to excite

an electron to an electronic state, a virtual state is involved in the three-photon absorption. It also supports the observation that the instantaneous peak is dominant only during the overlapping time between pump and probe beams. The long-lived bleaching signal is associated with the state-filling effect (figure 19b), the observed linear intensity dependence of the probe beam agrees with equation 21 for SFE. As discussed in the previous section, two-photon excitation is utilized for the creation of pump excited electrons in our experiment. Therefore, the population of the pump excited electrons is quadratically dependent on the pump intensity. The intensity dependence of the pump beam for the SFE is also quadratic under this condition. It matches the observed quadratic intensity dependence of the pump beam for the long-lived bleaching signal.

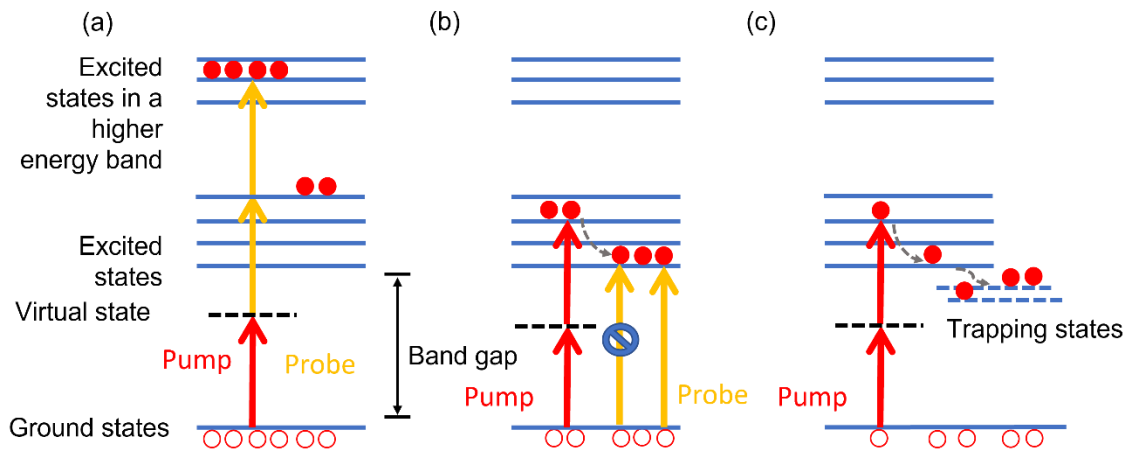


**Figure 19: Energy diagram of MAPbI<sub>3</sub> thin films. Red solid and hollow circles represent electrons and holes. Electrons are excited from ground states in the valence band to excited states in the conduction band. The red and yellow arrows represent pump and probe beams respectively. Gray dashed lines show the thermalization process of excited electrons. The black dashed lines show the virtual energy states. (a) Three-photon absorption, one pump photon and two probe photons are absorbed at**

**the same time via some virtual energy states. (b) State-filling effect, the thermalized electrons occupy energy states near the band edge and reduce the absorption of probe photons. (c) Electron injection from the energy states of the band edge to the trapping states in the band gap. The electron population near the band edge is reduced.**

Additionally, one possible explanation for the small long-lived bleaching signal in trace without the rapidly decaying negative signal is illustrated in figure 19c. The existence of trapping states in the band gap, which are created by defects and structural disorder, leads to an electron injection from the energy states near the band edge to these states. Therefore, the pump excited electron population above the band edge is reduced. This reduction results in a smaller long-lived bleaching signal.

For the rapidly decaying negative signal, it is associated with temporal state-filling effect (details will be discussed in chapter 4), which also depends on the charge carrier population as shown in figure 18. Therefore, the reduction of the pump excited electron population also leads to a smaller rapidly decaying negative signal. Since the rapidly decaying negative signal competes with the instantaneous absorption peak, the rapidly decaying negative signal will be overlooked when it has a small amplitude. It explains the difference between the two types of pump-probe traces.

### **2.3.3 Phasor analysis of pump probe microscopy data**

To qualitatively identify the two types of pump-probe traces, the phasor analysis is employed. The phasor distribution of the pump-probe traces of the MAPbI<sub>3</sub> thin film is shown in figure 20.

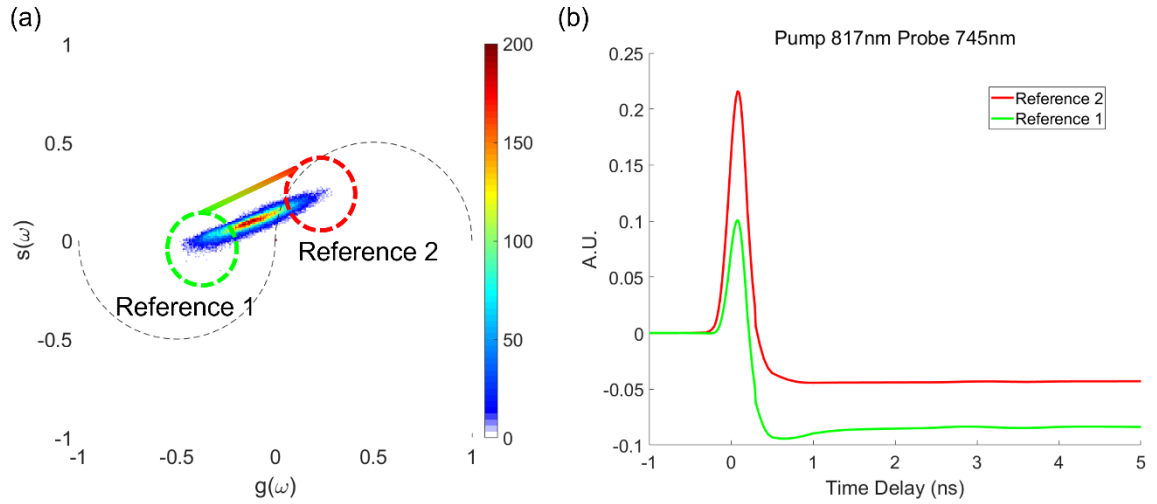


**Figure 20: Phasor plot of PPM data. (a) Shows the phasor location of the pump-probe trace of each pixel. The color bar shows the density of pixels that have the same phasor location. Dashed circles show the two ends of the phasor location. The average traces inside the circles are shown in (b).**

Since every pixel in the PPM image corresponds to a complete pump-probe trace, a pair of phasor values,  $s$  and  $g$  shown in equation 24 and 25, can be calculated for each pixel. Figure 20a shows the distribution of phasor values of all pixels. The two ends of the phasor distribution represent two types of pump-probe traces that is shown in figure 20b. They agree with the two types of traces that correspond to spatial heterogeneities shown in figure 17. The distribution of pixels that connect these two endpoints stands for regions have mixture of these two traces. Pixels within this distribution correspond to the regions, whose rapidly decaying negative signal is not completely vanished due to the electron injection to trapping states and the competition with the peak signal.

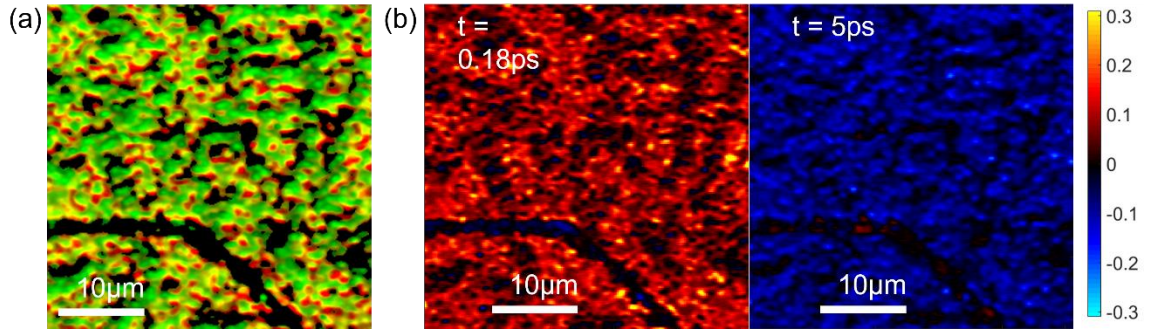


**Figure 21: Phasor image and PPM image of the same region. (a) A false color image shows the phasor information of each pixel. Red and green regions correspond to reference 2 and 1 in figure 20 respectively. Other regions are colored with the interpolated path with red and green color as two ends. An intensity filter is used to filter out regions with small signal. These regions, therefore, show black color in the phasor image. (b) PPM images of the same region as the phasor image. They show the pump-probe signal at different time delays ( $t = 0.18\text{ps}$  and  $t = 5\text{ps}$ ).**

A phasor image can be obtained by assigning red and green color to each pixel located in the red and green circles respectively. All the pixels between the two circles are colored with the interpolated path using red and green as the two endpoints. As shown in figure 21, images of PPM can only show the pump-probe signal at a certain time delay. The phasor image, in the other hand, can represent the character of the pump-probe trace by colors.

In both PPM and phasor images, some regions show the color close to black. However, they have different meanings. For the phasor image, an intensity filter is used to filter out regions with small signal before the phasor calculation is done. Therefore, they are not included in the phasor plot and assigned black color in the phasor image. For PPM images, regions with black color just indicate that the amplitude of their pump-probe signal is small at that specific time delay. The mark seen in the lowest third of all

images is artificially created by burning the sample with the probe beam with an excessively high power. It serves as a landmark for future image registration between phasor images and SEM images.

### 2.3.4 Correlation between phasor and SEM images

Now, the spatial heterogeneity of charge carrier dynamics can be qualitatively located with the phasor image. To investigate the correlation between this heterogeneity and the morphology of the MAPbI<sub>3</sub> thin film, mapping between SEM and phasor images of the same region needs to be achieved. As mentioned in the previous section, artificial landmarks are made to co-register SEM and phasor images. The mapping between SEM and FLIM images will be discussed in the next chapter.

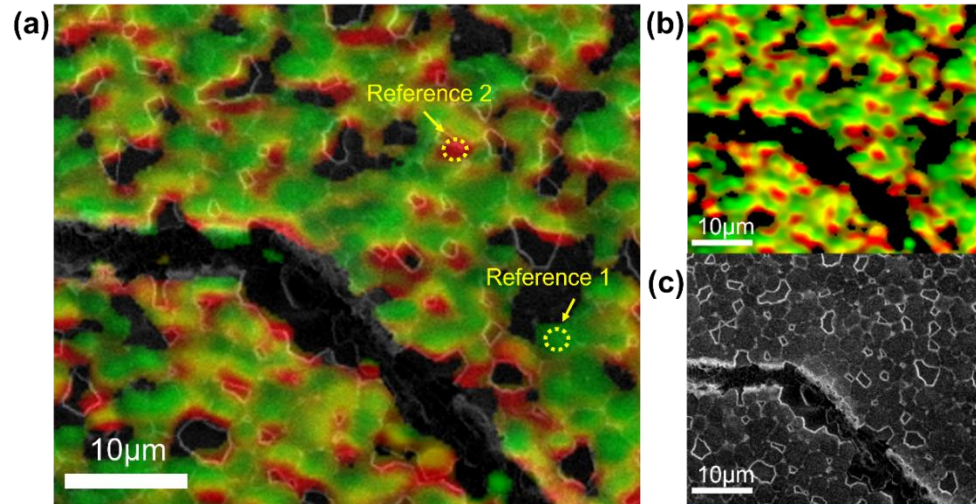


**Figure 22: Overlapped images of phasor and SEM. (a) Combined image with a phasor image (50% transparency) on top of a SEM image of the same region. Reference 1 and 2 show the same regions investigated in figure 14. (b) The phasor image with 0% transparency. (c) The SEM image. Bright white lines stand for the edge of pinholes that are generated during the sample preparation. Granular structure can**

**be seen in the image. Dim white lines stand for the grain boundaries. The grain size is roughly 2 to 3 $\mu\text{m}$ .**

The SEM image shown in figure 22c reveals the surface structure of the MAPbI<sub>3</sub> thin film. The artificial landmark can be clearly seen. There are also pinholes with bright white edge observed in the SEM image. They are introduced during the sample preparation and considered as spatial defects. A granular structure with grain size around 2 $\mu\text{m}$  can also be found in the most part of the film.

For the phasor image shown in figure 22b, the reference 1 and 2 correspond to the same regions that we investigate in figure 17. The green and red color in the dash circles again agree with the different charge carrier dynamics discussed in the previous section. In figure 22a, a phasor image with 50% transparency is registered with a SEM image via the artificial landmark. Regions with black color in the phasor image match with pinholes in the SEM image. The fact that little MAPbI<sub>3</sub> exists in pinholes agrees with the observation since the black regions indicate low pump-probe signal. The red regions are mostly distributed around pinholes and the green regions spread among grains. It suggests that the pump-probe signal near pinholes have less rapidly decaying negative signal and long-lived bleaching signal compared to the pump-probe signal in grains away from pinholes. Since the reduction of both signals could be associated with the existence of additional trapping states, it is likely that trapping states are more abundant near pinholes. It agrees with the previous report about the association of trapping states with spatial defects<sup>53</sup>.

### 2.3.5 Phasor analysis of fluorescence lifetime microscopy data

Since the spatial heterogeneity of charge carrier dynamics in picosecond time scale has been discovered, heterogeneity is likely to be observed in FLIM images which monitor the charge carrier dynamics in a longer timescale (nanosecond). Figure 23a shows the fluorescence intensity of different regions in the MAPbI<sub>3</sub> thin film at a 3ns time delay. The reflectance image in figure 23b shows the morphology of the same area by collecting backscattered light from the sample.

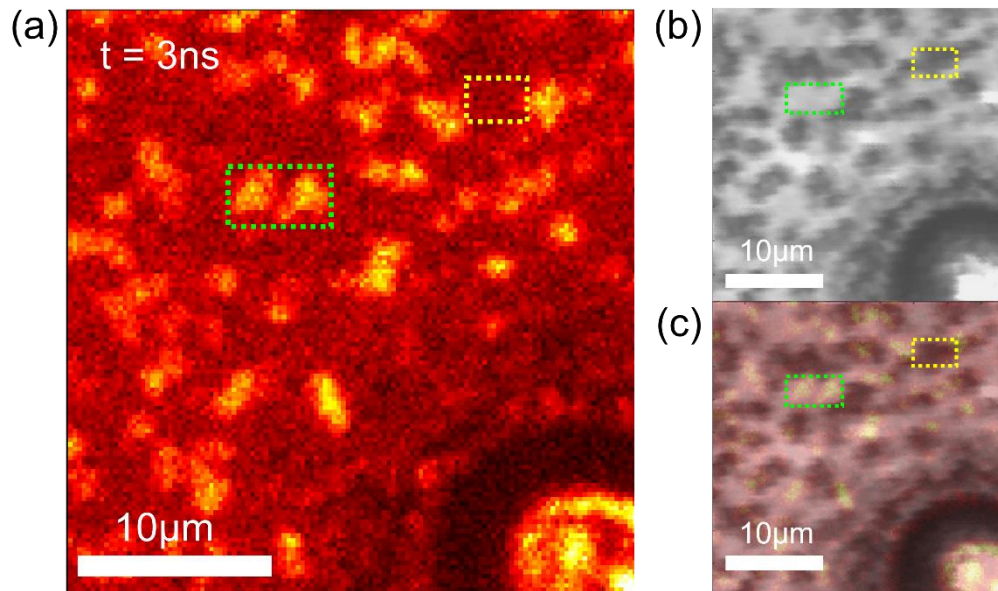


**Figure 23: FLIM and reflectance images of MAPbI<sub>3</sub> thin films. (a) FLIM image at a 3ns time delay. The lower right corner shows an intrinsic spatial defect serving as the landmark for image registration. The color bar shows the intensity of fluorescence signal. (b) Reflectance image of the same region. Darker regions represent spatial defects. (c) Combined images of a FLIM image (27% transparency) on top of a reflectance image. Dashed boxes with green and yellow color highlight the correlation between fluorescence signal and morphology of the same region.**

A clear correlation between the fluorescence intensity at 3ns and the morphology of the same region can be found in figure 23c. High fluorescence intensity is associated with regions with flat surface in the green dash box. Low fluorescence intensity is associated with regions related to spatial defects.

To better understand the spatial heterogeneity in FLIM, the same phasor approach is used for analyzing FLIM data. Figure 24a and b show the phasor distribution and corresponding time-resolved traces of fluorescence signal. Due to the high repetition rate of our laser beam, the maximum time delay of the fluorescence signal that can be detected is limited by the time difference between two reference pulses (12.5ns). In our experiment, a time scale of 7ns is used. The 'shoulder' shown in fluorescence traces at 0.7ns is likely due to a reflected fluorescence signal between the PMT and the spectral filter. Unlike the time-correlated pump-probe trace, which has multiple charge carrier dynamics involved, the time-correlated fluorescence trace only monitors the radiative recombination of charge carriers. Since most trap-assisted recombination processes are non-radiative<sup>54,55</sup>, the major contribution to the fluorescence signal is the band-to-band recombination process. With the initial charge carrier density calculated in the previous section, the dominant recombination process will be the trap-assisted recombination. Therefore, the time-dependent charge carrier population  $n(t)$  can be estimate by equation 10. Since the amplitude of the band-to-band recombination is proportional to  $k_2n(t)^2$  as shown in equation 9, a single exponential decay is adapted

to describe such radiative recombination process. However, due to the limited time resolution of FLIM, an instrumental response function (ISF) needs to be included. The fluorescence trace is the convolution between a single exponential decay and the ISF. Details of the ISF and fitting model will be discussed in the next chapter.

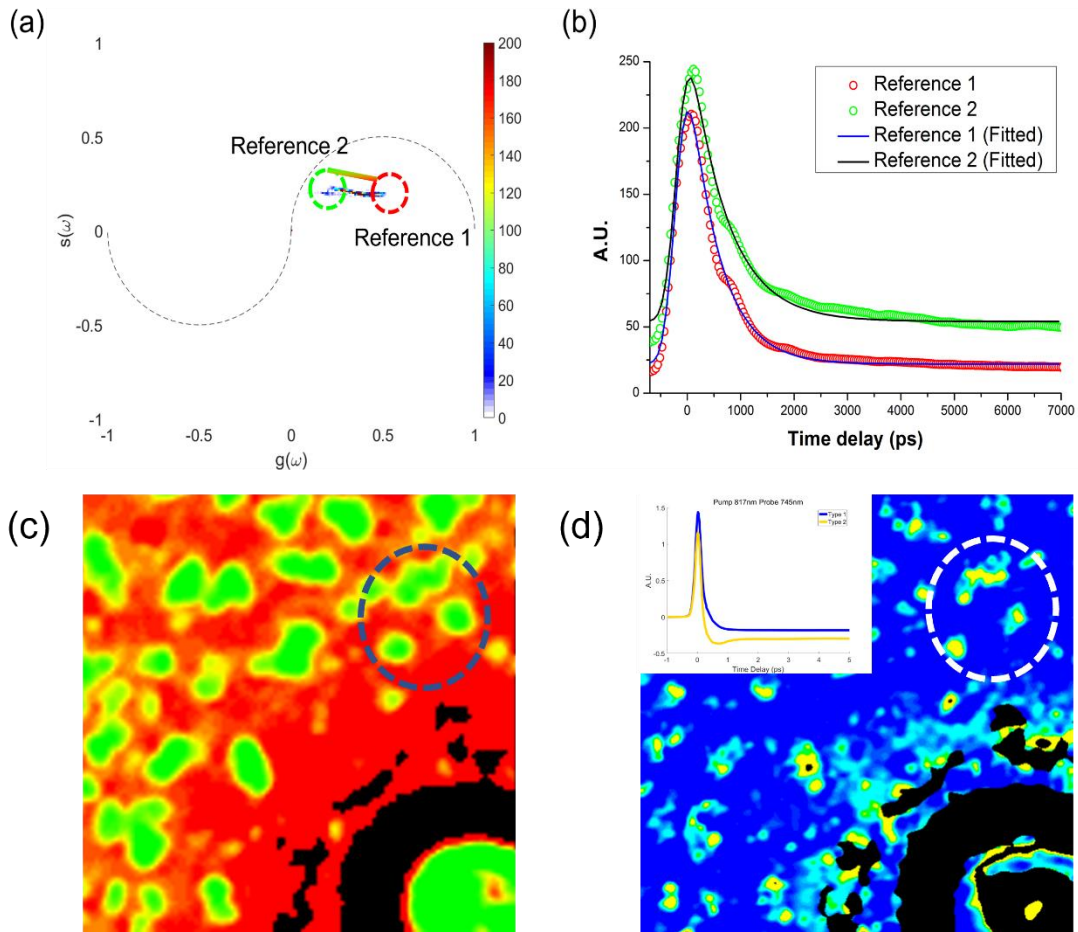


**Figure 24: Phasor plot of FLIM data. (a) Phasor distribution of different fluorescence traces. (b) Red and green circles show the fluorescence traces of reference 1 and 2 in (a). The solid lines are fitting curves of two measured traces. (c) Phasor image of FLIM data. (d) Phasor image of PPM data. Insert is pump-probe traces whose phasor locations correspond to yellow and blue color respectively.**

By fitting the fluorescence traces of reference 1 and 2 (solid lines in figure 24b), we can extract fluorescence lifetime ( $\tau_F$ ) and relate to their phasor location. The fluorescence lifetime 0.56ns and 0.69ns in reference 1 and 2 regions. So, the color in the phasor image (figure 24c) can qualitatively represent the fluorescence lifetime: from green to red, the corresponding fluorescence lifetime is reduced. This method provides a fast way to study the character of fluorescence trace of different regions without fitting each pixel.

The correlation between charge carrier dynamics in different timescales is found in figure 24c and d which show the phasor images of FLIM and PPM of the same region respectively. Green regions, whose FLIM phasor location represents in reference 2, in the blue dashed circle of figure 24c match yellow regions, whose pump-probe trace shows rapidly decaying negative signal in picosecond scale., in the white dashed circle of figure 24d.

A statistical analysis is adapted to study such correlation. For every pixel, the fluorescence and pump-probe traces are recorded. Fluorescence lifetime is obtained from each pixel by fitting the fluorescence trace. Pixels are sorted by the phasor location of their pump-probe traces. In figure 25a, pixels locate in two ends of the PPM's phasor distribution (blue and yellow circles) are investigated. The fluorescence lifetime associated with these pixels are counted separately. The counting number is normalized respectively to show the lifetime distribution (figure 25c). Clearly, pixels whose PPM

phasor values correspond to the reference a location tend to have shorter fluorescence lifetime. As discussed in the previous section, reference a might be associated with abundant trapping states. Therefore, the shorter fluorescence lifetime supports this correlation since abundant trapping states correspond to a faster trap-assisted recombination.

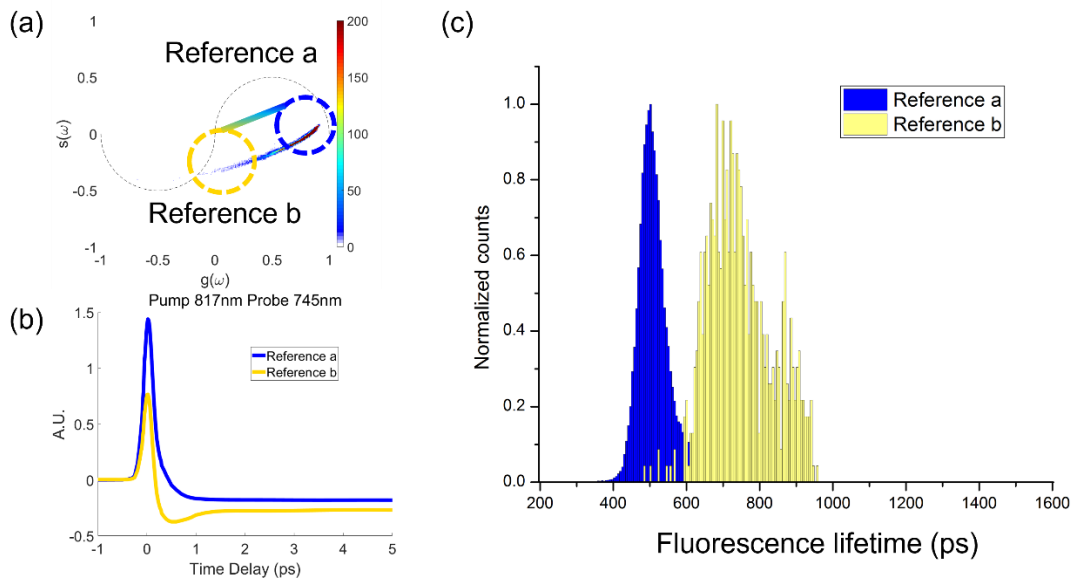


**Figure 25: Fluorescence lifetime histogram of regions with different PPM phasor locations. (a) Phasor distribution of pump-probe signal. The fluorescence lifetime histogram of pixels located in reference a and b are plotted with corresponding color, blue and yellow, respectively in (c). (b) The averaged pump-probe traces of two investigated regions. (c) Fluorescence lifetime histogram.**

## 2.4 Conclusion

In this chapter, the spatial heterogeneity of charge carrier dynamics is demonstrated by PPM and FLIM. Phasor analysis is adapted to qualitatively distinguish the different dynamics. By co-registering PPM and FLIM with the morphology of MAPbI<sub>3</sub> thin films, regions having little rapidly decaying negative and long-lived

bleaching pump-probe signal are found to have shorter fluorescence lifetime and be around spatial defects. The presence of abundant trapping states in these regions could be a possible explanation for the quench of negative signals and the reduction of the fluorescence lifetime.

### **3 Separating and bridging charge carrier dynamics of MAPbI<sub>3</sub> thin films on different timescales**

In chapter 2, the spatial heterogeneity of charge carrier dynamics has been qualitatively investigated by the phasor image of PPM and FLIM. A more quantitative analysis requires better understanding of the pump-probe trace which has multiple charge carrier dynamics involved on picosecond timescales. In this chapter, a model is introduced to separate charge carrier dynamics on the same timescale. The time window of pump-probe signal is also extended to nanosecond scale. Therefore, the charge carrier dynamics shown by PPM and FLIM can be directly compared.

#### **3.1 Experimental adjustment**

The upper limit of the pump-probe time delay is set by the length of the translational stage. A longer translational stage is adapted to extend the maximum time delay of the pump-probe trace to reach  $t = 3\text{ns}$ . A power adjustment of pump and probe beams is also made to reduce the multiphoton interaction, which is quadratically dependent on the intensity of the probe beam. In this chapter, the power of the pump beam is increased to 0.6mW ( $4 \times 10^{17}/\text{cm}^3$  initial charge carrier density) and the probe beam power is reduced to 0.03mW. With this power combination, the three-photon absorption process observed during the temporal overlap of the pump and probe beams is less pronounced and the long-lived bleaching signal is elevated due to its quadratic intensity dependence on the pump beam. To compare the fluorescence signal and

pump-probe signal, the excitation beam for the FLIM experiment is chosen to have the same wavelength and power as the pump beam used in the PPM experiment.

## **3.2 Model for charge carrier dynamics**

### **3.2.1 Model for charge carrier dynamics in pump-probe traces**

In chapter 2, the ability of the pump-probe signal to reveal the charge carrier dynamics with spatial resolution in MAPbI<sub>3</sub> thin films is demonstrated. However, the involvement of multiple charge carrier dynamics at the same time delays certainly impedes the analysis of each dynamic. With the help of the intensity dependence analysis in the previous chapter, a time-correlated model is proposed to describe the observed pump-probe signal.

The observed pump-probe signal mainly consists of three charge carrier dynamics, which are the three-photon absorption signal, the rapidly decaying negative signal, and the long-lived bleaching signal. For the three-photon absorption signal, it requires the presence of the pump and probe beams at the same time. Therefore, the amplitude of the three-photon absorption  $A_1$  is proportional to the intensity of the temporally overlapped part of the two beams (figure 26a). Since the three-photon absorption linearly depends on the pump intensity and quadratically depends on the probe intensity,  $A_1$  can be expressed as:

$$A_1(t) = \alpha_1 \int_{-\infty}^{+\infty} dt_1 (A_{pr} e^{\frac{-t_1^2}{2\sigma^2}})^2 \times A_{pu} e^{\frac{-(t-t_1)^2}{2\sigma^2}} = \alpha_1 \left(\frac{2}{3}\pi\sigma^2\right)^{\frac{1}{2}} A_{pr}^2 A_{pu} e^{\frac{-t^2}{3\sigma^2}} \quad (30)$$

where the intensity of the pump and probe beams are  $I_{pu}(t_1) = A_{pu} \exp(-t^2/2\sigma^2)$  and  $I_{pr}(t) = A_{pu} \exp(-t_1^2/2\sigma^2)$  respectively,  $\sigma$  is the standard deviation of the Gaussian pulse and  $\alpha_1$  is a numerical coefficient. The assumption that pump and probe pulses are Gaussian pulses and have the same pulse width is made.

For the long-lived bleaching signal, its amplitude  $A_2$  is associated with the charge carrier population as discussed in the previous chapters. Therefore, the reduction of the charge carrier population needs to be included. The charge carrier recombination with the initial charge carrier density mentioned in the previous section is dominant by the trap-assisted recombination, the population change follows equation 10. A time delay time delay  $t_0$  must be included for the actual population change since the pump excited electrons take time (usually several hundred femtoseconds<sup>56</sup>) to reach the quasi-equilibrium distribution to start recombination processes. It is supported by the fitting result shown in the next section. Additionally, since the pump excitation relies on the two-photon excitation, a quadratic intensity dependence should be included when calculate the charge carrier population. Therefore, the charge carrier population  $N$  can be written as:

$$N(t) = \beta \int_{-\infty}^{t-t_0} dt_1 (A_{pu} e^{-\frac{t_1^2}{2\sigma^2}})^2 \times e^{-\frac{-(t-t_0-t_1)}{\tau}} = \beta \left( \frac{\sqrt{\pi}}{2} e^{\frac{\sigma^2}{4\tau^2}} \right) A_{pu}^2 e^{-\frac{-(t-t_0)}{\tau}} \times \text{erfc} \left( \frac{\sigma}{2\tau} - \frac{t-t_0}{\sigma} \right) \quad (31)$$

where  $\tau$  is the recombination lifetime,  $\beta$  is a numerical coefficient and  $\text{erfc}$  is the complementary error function:

$$\text{erfc}(t) = \frac{2}{\sqrt{\pi}} \int_t^{+\infty} e^{-x^2} dx \quad (32)$$

Due to the finite temporal profile of the probe beam, the amplitude of the long-lived bleaching signal  $A_3$  is obtained by considering the contribution of the state-filling effect within the probe pulse as shown in figure 26b:

$$A_3(t) = \alpha_2 \int_{-\infty}^{+\infty} N(t_1) A_{pr} e^{-\frac{(t_1-t)^2}{2\sigma^2}} dt_1 \quad (33)$$

$$A_3(t) = \alpha_2 \beta A_{pu}^2 A_{pr} \sigma^2 \frac{\pi}{\sqrt{2}} e^{\frac{3\sigma^2}{4\tau^2}} e^{-\frac{t-t_0}{\tau}} \left( 2 - \text{erfc} \left( \frac{t-t_0}{\sqrt{3}\sigma} - \frac{\sqrt{3}\sigma}{2\tau} \right) \right) \quad (34)$$

where  $\alpha_2$  is a numerical coefficient. If the recombination lifetime  $\tau$  is much longer than the time scale of the pump-probe signal, equation 34 can be simplified with the approximation that  $\tau \gg t, \sigma$ :

$$A_3(t) = \alpha_2 \beta A_{pu}^2 A_{pr} \sigma^2 \frac{\pi}{\sqrt{2}} \left( 2 - \text{erfc} \left( \frac{t-t_0}{\sqrt{3}\sigma} \right) \right) \quad (\tau \gg t, \sigma) \quad (35)$$

The long-lived bleaching signal in the observed pump-probe signal satisfies this approximation when the time scale of the pump-probe signal is within 20ps. It is supported by the extended pump-probe signal, which shows that the long-lived bleaching signal has a lifetime in nanosecond scales.

As for the rapidly decaying negative signal, equation 34 is adapted as an empirical model based on its dependence of the charge carrier population. Since the intensities of the pump and probe beams are fixed, the complete expression of pump-probe trace, after absorbing all constant values to the coefficients, can be written as:

$$A_{pp}(t) = \alpha_t e^{\frac{-t^2}{3\sigma^2}} + \alpha_r e^{\frac{-t-t_0}{\tau}} \left( 2 - \operatorname{erfc} \left( \frac{t-t_0}{\sqrt{3}\sigma} - \frac{\sqrt{3}\sigma}{2\tau} \right) \right) + \alpha_l \left( 1 + \operatorname{erf} \left( \frac{t-t_0}{\sqrt{3}\sigma} \right) \right) \quad (36)$$

where  $A_{pp}$  is the amplitude of the pump-probe trace,  $\tau$  is the lifetime of the rapid decaying negative signal,  $\alpha_t$  is the coefficient for the three-photon absorption,  $\alpha_r$  is for the rapid decaying negative signal, and  $\alpha_l$  is for the long-lived bleaching signal. This expression is valid for the pump-probe signal with picosecond time scales.

Using a longer translational stage, the lifetime  $\tau_l$  of the long-lived bleaching signal can be obtained separately. Since the short-lived signals have no contribution to the pump-probe signal at nanosecond scale. With the approximation that  $\tau_l, t \gg \sigma$  and  $t \gg t_0$ , the pump-probe trace at long time delay can be simply written as:

$$A_{pp}(t) = 2\alpha_r e^{\frac{-t}{\tau_l}} + \alpha_o \quad (\tau_l, t \gg \sigma \text{ and } t \gg t_0) \quad (37)$$

where  $\alpha_o$  is an offset signal that have lifetime beyond our detection range.

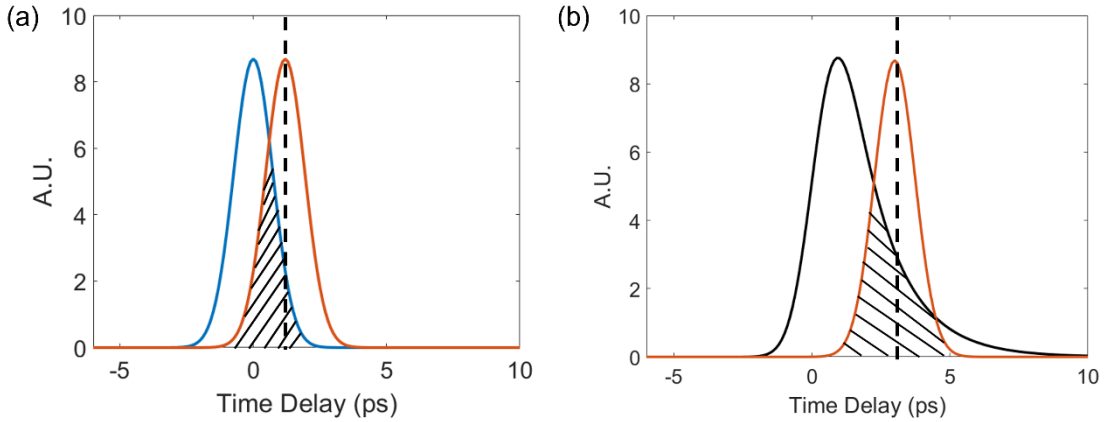


**Figure 26: Pump-probe signal of two charge carrier dynamics. The dashed line indicates the time delay. (a) The three-photon absorption only happens in the shadow part where pump (blue) and probe (red) beams temporally overlap. (b) The long-lived bleaching signal counts the state-filling effect within the probe beam profile (red) due to the presence of charge carrier population (black).**

### 3.2.2 Model for charge carrier dynamics in fluorescence traces

A time-correlated model is also introduced to describe the fluorescence signal. Since the trap-assisted recombination is still dominant in with the adjust power combination of the pump and probe beams<sup>51</sup>, the time-dependent charge carrier population  $n(t)$  can be approximated by a single exponential decay according to equation 10. The contribution of the band-to-band recombination to the fluorescence signal can be described as:

$$A_b(t) \propto k_2 n(t)^2 = \beta_b e^{-\frac{t}{\tau_b}} \quad (38)$$

where  $\tau_b$  is the lifetime of the fluorescence signal from the band-to-band recombination,  $\beta_b$  is a numerical coefficient. Additionally, a fast recombination is also observed in the fluorescence trace. Due to the limited time resolution, the lifetime of this recombination cannot be revealed by our experimental setup. To include this recombination in the model, a delta function is assigned to represent it. The total fluorescence signal can be written as:

$$A_f(t) = \beta_b e^{-\frac{t}{\tau_b}} + \beta_f \delta(t) + \beta_o \quad (39)$$

where  $\beta_f$  is the numerical coefficient associated with the fast recombination,  $\beta_o$  is the numerical coefficient for the offset signal that have lifetime beyond our detection range. The instrumental response function (ISF) should be also considered when reconstructing the fluorescence trace. The actual fluorescence trace can be expressed by the convolution between the ISF and the fluorescence signal:

$$A_F(t) = (A_{ISF} * A_f)(t) = \int_{-\infty}^{+\infty} A_{ISF}(t_1)A_f(t - t_1) dt_1 \quad (40)$$

where  $A_{ISF}$  is the amplitude of the ISF and  $A_f$  is the amplitude of the observed fluorescence signal. The ISF is obtained by measuring the fluorescence trace of potassium dihydrogenphosphate (KDP) sample excited by the same pump beam. Since the observed signal of KDP is mainly from the scattered second harmonic generation (SHG) signal generated by the pump excitation, which only exists within the pulse during of the excitation beam, such signal can be treated as a delta function. Therefore, the convolution between the KDP signal and the ISF should return the ISF itself.

### 3.3 Fitting result of PPM and FLIM traces

Now, the PPM and FLIM traces can be decomposed into several dynamics with the model proposed in the last section. Figure 27 illustrates the typical pump-probe traces under the adjusted power combination of the pump and probe beams.

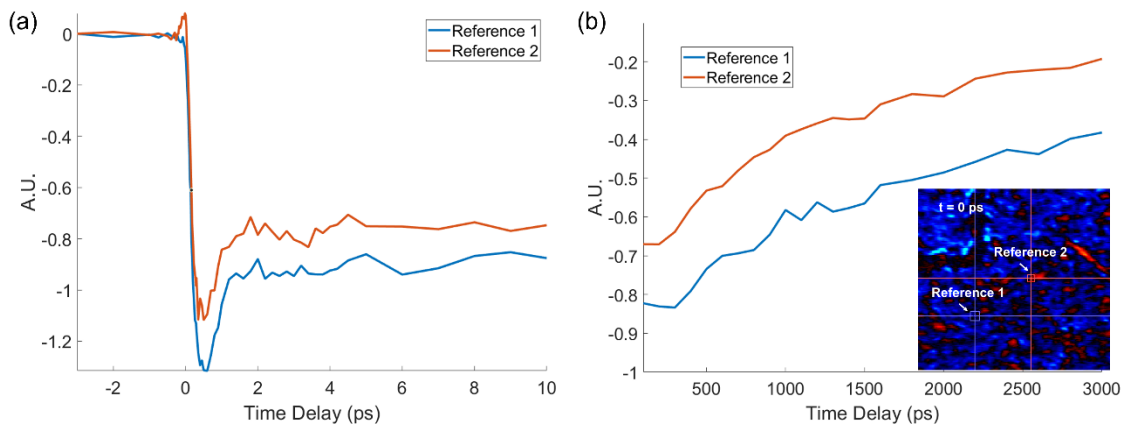


**Figure 27: Pump-probe traces under adjusted beam power. (a) Pump-probe traces of two reference regions ranging from  $t = -3$ ps to  $t = 10$ ps. (b) Pump-probe traces at the same regions ranging from  $t = 100$ ps to  $t = 3000$ ps. Insert shows the PPM image**

at  $t = 0.04\text{ps}$ . The red and blue boxes correspond to the two reference regions respectively.

Due to the power reduction of the probe beam, now the rapidly decaying negative signal becomes dominant, and the instantaneous absorption peak is less pronounced. A nanosecond time-delay is also achieved for the pump-probe signal. Both regions show a monotonically decreasing long-lived bleaching signal.

Two timescales of the pump-probe trace are fitted separately to optimize the fitting result. For the picosecond scale, equation 36 is adapted for the fitting. For the nanosecond scale, equation 37 is used to fit the data ranging from 100ps to 3000ps. The fitting result of both timescales are shown in figure 28.

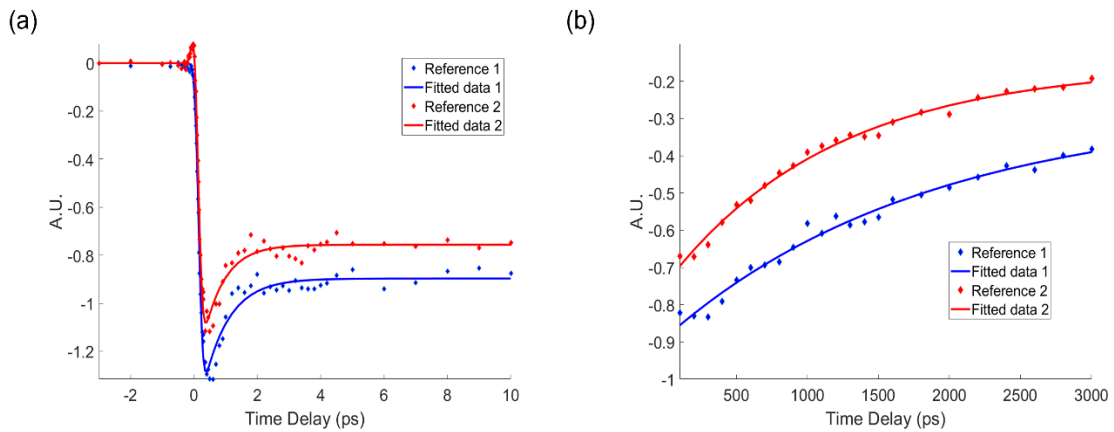


**Figure 28: Fitting traces of PPM data. The solid lines show the fitting traces of the measured data. (a) Fitting result of the data ranging from  $t = -3\text{ps}$  to  $t = 10\text{ps}$ . (b) Fitting result of the data ranging from  $t = 100\text{ps}$  to  $t = 3000\text{ps}$ .**

Our model successfully reconstructs the two types of pump-probe traces under adjusted power. To better understand the contribution of different charge carrier dynamics in pump-probe traces. The amplitude of each fitting parameter from the two

types of the pump-probe traces ranging from  $t = -3\text{ps}$  to  $t = 10\text{ps}$  is listed in table 2.

Additionally, charge carrier dynamics are separated with the help of the fitting result, and their corresponding pump-probe traces are plotted in figure 29.

**Table 2: Fitting parameters of pump-probe traces in the first 10ps**

	$\alpha_t(\text{A.U.})$	$\alpha_r(\text{A.U.})$	$\alpha_l(\text{A.U.})$	$\tau(\text{ps})$	$t_0(\text{ps})$
Reference 1	$0.33 \pm 2.19$	$-15.67 \pm 0.88$	$-25.83 \pm 0.31$	$0.79 \pm 0.10$	$0.15 \pm 0.01$
Reference 2	$16.32 \pm 1.96$	$-13.83 \pm 0.89$	$-21.78 \pm 0.26$	$0.67 \pm 0.09$	$0.15 \pm 0.01$

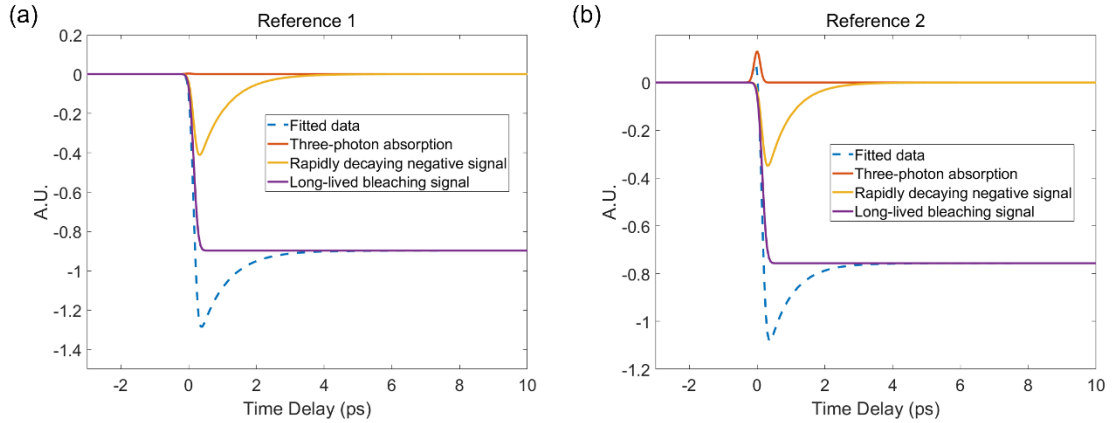


**Figure 29: Pump-probe traces of individual charge carrier dynamics. Each solid line stands for the pump-probe trace of a single charge carrier dynamic. The dashed lines show the complete pump-probe trace, which combines these three dynamics. (a) and (b) correspond to the two reference regions shown in figure 27.**

The different amplitude  $\alpha_l$  of the long-lived bleaching signal in the two traces might be explained by the population difference of trapping states. As mentioned in the previous chapter, the existence of abundant trapping states can lead to larger electron injection to these states from the band edge. The reduction of the excited electron

population near the band edge will result in a weaker state-filling effect for the probe beam. Therefore, a smaller amplitude of the long-lived bleaching signal in the pump-probe trace could be associated with regions having abundant trapping states.

For the three-photon absorption, in regions that have strong long-lived bleaching signal, which is considered to have fewer trapping states, the amplitude of the three-photon absorption is greatly reduced. The significant difference between the amplitude  $\alpha_t$  of the three-photon absorption in two traces suggests that such multiphoton interaction is likely to be more pronounced in regions with abundant trapping states.

Additionally, the same time delay constant  $t_0$  is found in both traces. It stands for the thermalization time for excited electrons to reach the quasi-equilibrium distribution. This thermalization process happens before the major recombination and injection processes. Therefore, the value of the time delay should be consistent for all regions, which is consistent with our fitting result.

To bridge the charge carrier dynamics shown in PPM and FLIM, the fitting result of pump-probe traces in the large time delays (ranging from  $t = 100\text{ps}$  to  $t = 3000\text{ps}$ ) is discussed together with the fitting result of the FLIM data. Figure 30 shows a fitted fluorescence trace and the decomposed recombination processes.

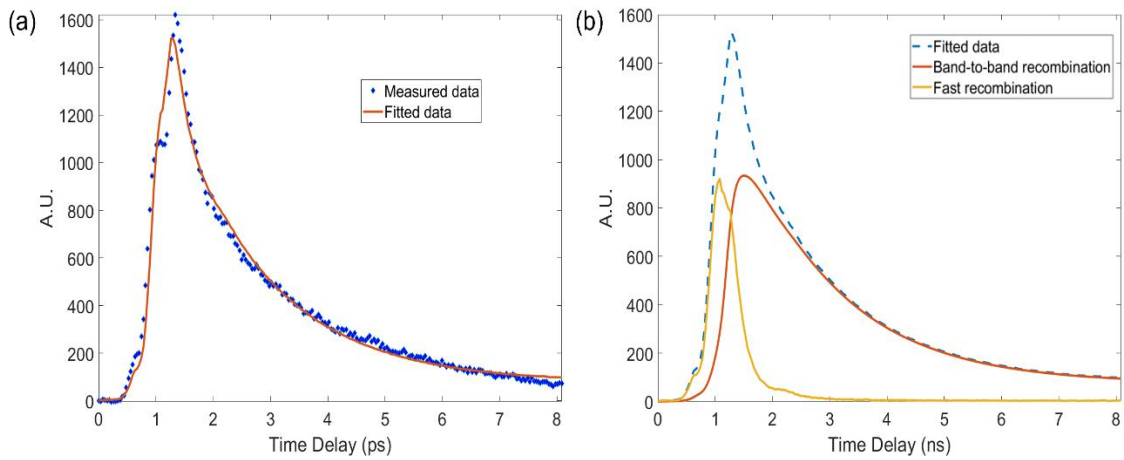


**Figure 30: Fitting result of the fluorescence trace. (a) The solid line shows the fitted trace including fast and band-to-band recombination processes. (b) The solid lines show the fluorescence trace of each recombination process, and the dashed line shows the complete fitted trace.**

Heterogeneity is also found in the FLIM data (figure 31a). To compare the fluorescence signal and the pump-probe signal in nanosecond time scales, the fluorescence and pump-probe signals of the same region are investigated. The reference 1 and 2 shown in the insert of figure 27 matches the region 1 and 2 shown in figure 31a. Equation 37 is used to obtain the fitting parameters of the pump-probe traces in long time delays. Table 3 compares the fitting result of the two types of fluorescence traces shown in figure 31 and the two pump-probe traces in long time delays shown in figure 29b.

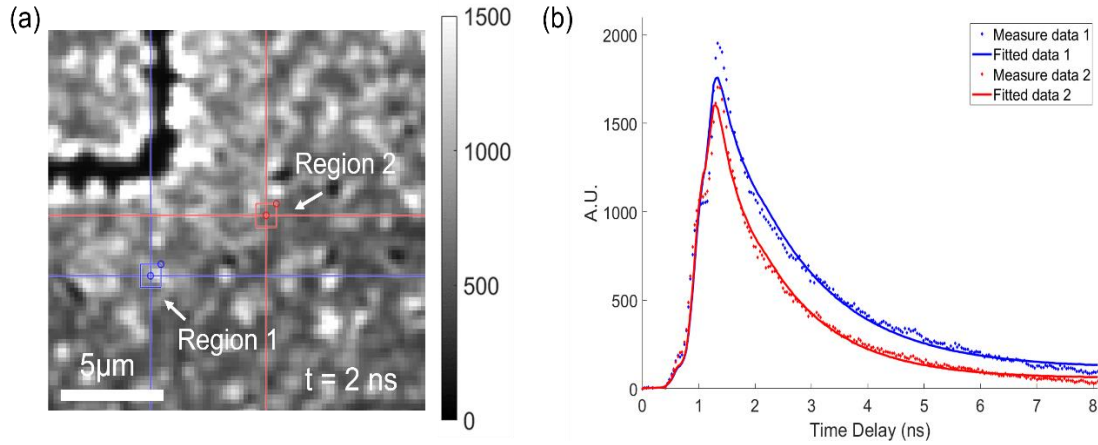


**Figure 31: Heterogeneous fluorescence signal observed in MAPbI<sub>3</sub> thin films. (a) FLIM image at time delay  $t = 1$  ns. Two regions within the boxes are investigated. They are the same region shown in the insert of figure 27. (b) fluorescence signal of the two regions shown in (a).**

**Table 3: Fitting parameters of fluorescence and pump-probe signal**

Fluorescence signal	$\beta_f$ (A.U.)	$\beta_b$ (A.U.)	$\tau_b$ (ns)	$\beta_o$ (A.U.)
Measured Data 1	$789.0 \pm 24.5$	$156.0 \pm 2.7$	$1.46 \pm 0.05$	$9.00 \pm 0.94$
Measured Data 2	$885.5 \pm 21.3$	$131.6 \pm 2.7$	$1.23 \pm 0.04$	$4.21 \pm 0.66$
Pump-probe signal	$\alpha_l$ (A.U.)	$\tau_1$ (ns)	$\alpha_o$ (A.U.)	
Reference 1	$-0.62 \pm 0.04$	$1.84 \pm 0.09$	$-0.27 \pm 0.05$	
Reference 2	$-0.59 \pm 0.01$	$1.18 \pm 0.30$	$-0.16 \pm 0.02$	

As shown in table 3, a shorter lifetime and a reduced amplitude of the band-to-band fluorescence signal is shown in measured data 2, which agrees with the shorter lifetime and reduced amplitude of the pump-probe signal observed in reference 2.

The similar lifetimes observed in the fluorescence and pump-probe signals indicate that in the fluorescence signal and the pump-probe signal are monitoring the similar charge carrier dynamics in nanosecond scales. Since the fluorescence signal only reflects the radiative recombination processes and the pump-probe signal monitors the whole charge carrier population changes including radiative and non-radiative recombination processes, combining these two signals can provide a complete picture of charge carrier dynamics in nanosecond scales.

With the help of the two models, different charge carrier dynamics can be identified from the first picosecond to several nanoseconds, a more quantitative investigation on the impact of spatial heterogeneity on charge carrier dynamics can be achieved.

### ***3.4 Correlation between charge carrier dynamics and the sample's morphology***

The models introduced in the previous sections enable a pixel-by-pixel fitting on PPM and FLIM data. Fitting result of single pixel is included in Appendix B. Instead of using combined SEM and phasor images to qualitatively show the spatial heterogeneity of charge carrier dynamics, images of fitting parameters are combined with the SEM image of the same area to quantitatively represent the spatial distribution of different dynamics. Figure 32 illustrates the spatial distribution of two radiative recombination processes. The amplitude of both recombination processes is normalized by the mean value of the whole region.  $I_f$  and  $I_b$  are used to represent the normalized amplitude of the fast and band-to-band recombination respectively. Additionally, the total

fluorescence fluence of each pixel, which is obtained by integrating the whole fluorescence trace, is also shown (figure 32b). The amplitude of the fluorescence fluence  $I_T$  is also normalized by the mean value of the whole region.

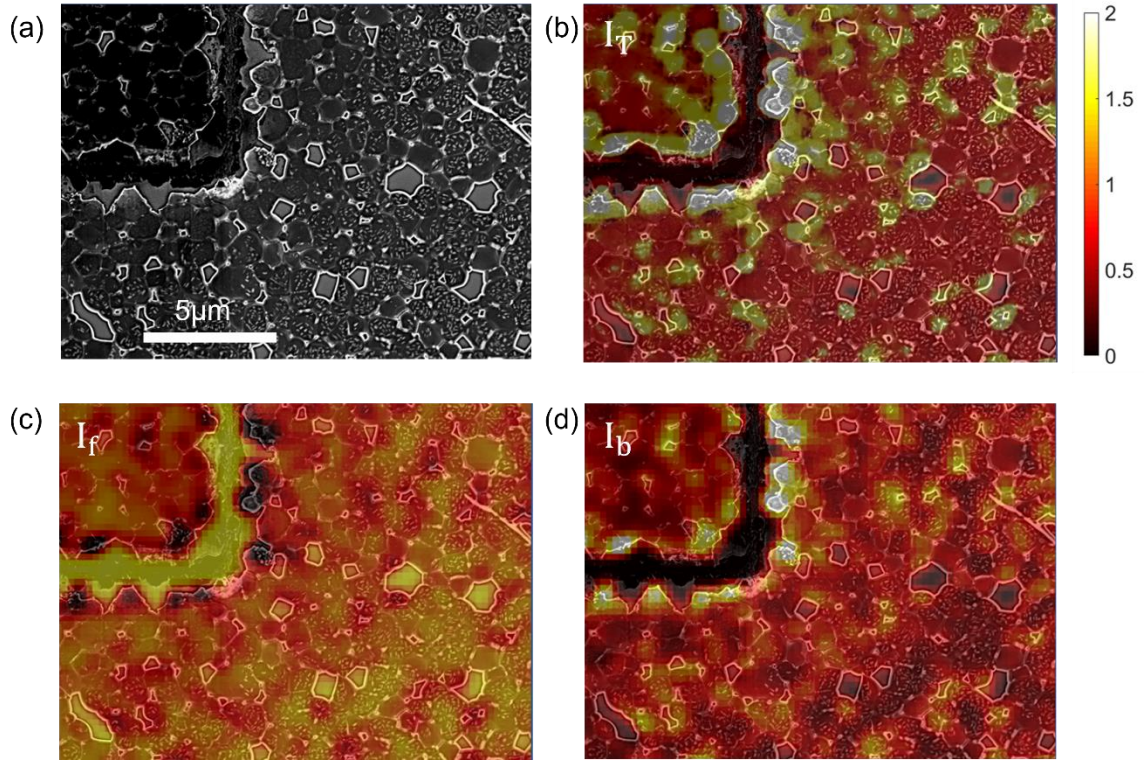


**Figure 32: Combined images of SEM and different radiative recombination processes. The amplitude of each recombination process is normalized by its mean value of the whole area. The color bar represents the amplitude of each process.  $I_T$ ,  $I_f$  and  $I_b$  correspond to the amplitude of total fluorescence fluence, fast recombination, and band-to-band recombination respectively. (a) SEM image. (b) Combined image with the image of the total fluorescence fluence (50% transparency) on top of the SEM. (c) Combined image of the fast recombination and SEM. (d) Combined image of the band-to-band recombination and SEM.**

The artificial mark on the top left side in figure 32 is created by burning the sample with excess laser power. It shows little signal from the band-to-band recombination in figure 32d and small total fluorescence fluence in figure 32b. However,

a significant fast recombination signal is observed within the mark (figure 32c). Pinholes with bright edges also show similar result as the artificial mark. The anti-correlation between the amplitude of the fast recombination and the other two signals (band-to-band recombination and total fluorescence fluence) suggests that spatial defects such as damage spots and pinholes might provide extra radiative recombination pathways that speed up the charge carrier recombination processes.

The same analysis method can be applied to the PPM data. Figure 33 shows the correlation between the different charge carrier dynamics in picosecond scales and the sample's morphology. Again, the amplitude of each dynamic is normalized by the mean value of the whole region.  $L_t$ ,  $L_r$  and  $L_l$  are the normalized amplitude of the three-photon absorption, rapidly decaying negative signal, and long-lived bleaching signal respectively.

Unlike the fast radiative recombination signal shown in the FLIM data, which shows a strong correlation within the pinholes, the three-photon absorption shows little signal at pinholes. Instead, its amplitude is only significant in regions near the boundaries of pinholes. The small amplitude of the three-photon absorption inside the pinholes is due to the reduction of the  $\text{MAPbI}_3$  material in these regions, which reduces the overall amplitude of the pump-probe signal. It is consistent with the amplitude reduction of the total fluorescence fluence inside the pinholes shown in figure 32b. The large three-photon absorption signal, together with the reduced rapidly decaying

negative signal and the long-live bleaching signal suggests the existence of abundant trapping states near the pinholes. It is consistent with the spatial distribution analysis of the pump-probe signal discussed in chapter 2, which utilize phasor to qualitatively sort different types of charge carrier dynamics.

Additionally, the amplitude of the long-live bleaching signal show strong correlation with the granular structure. This signal is more significant within the grain interiors compared with at the grain boundaries. The reduction of amplitudes across the grain boundaries might also suggest more trapping states exist at the grain boundaries.

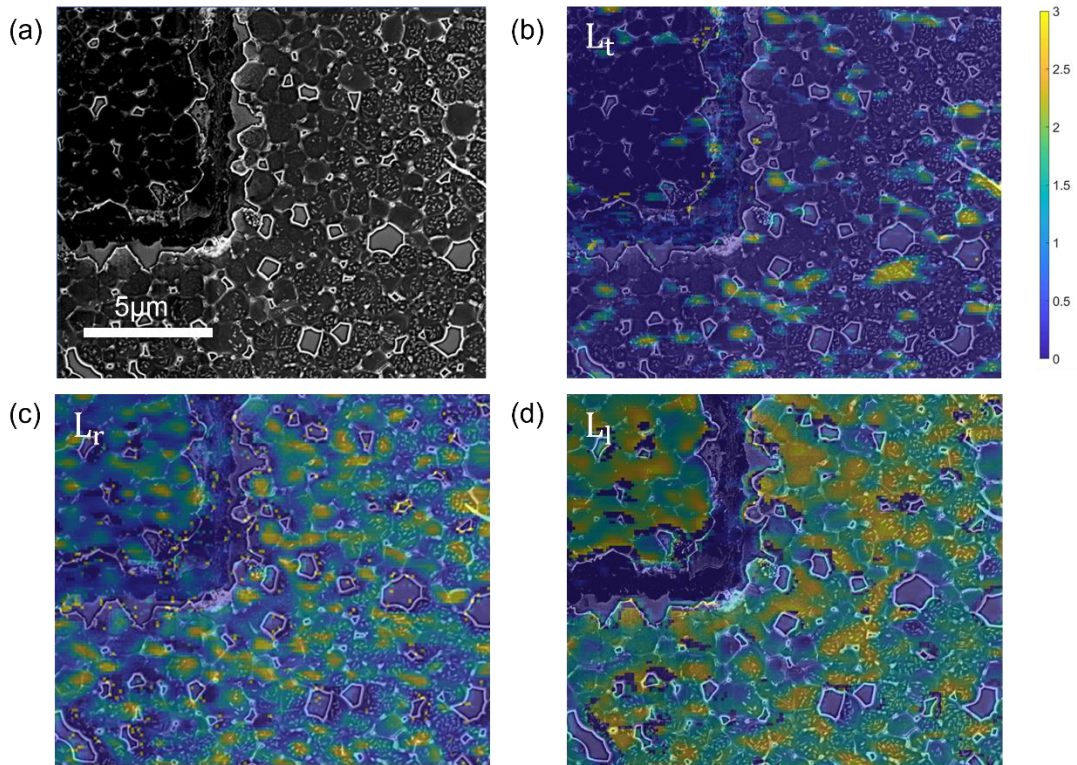


**Figure 33: Combined images of SEM and different charge carrier dynamics in nanosecond scales. The amplitude of each dynamic is normalized by its mean value of the whole area. The color bar represents the amplitude of each process.  $L_t$ ,  $L_r$  and  $L_l$  correspond to the amplitude of three-photon absorption, rapidly decaying negative**

signal, and long-lived bleaching signal respectively. (a) SEM image. (b) Combined image with the image of the three-photon absorption (50% transparency) on top of the SEM. (c) Combined image of the rapidly decaying negative signal and SEM. (d) Combined image of the long-lived bleaching signal and SEM.

An amplitude comparison of the long-lived bleaching signal across a selected grain is plotted in figure 34 to support this observation. From figure 34a, a clear grain structure is observed. The white dashed line highlights the grain boundary between the two grains. The signal amplitude of 15 pixels along the red arrow is recorded in figure 34b. Clear amplitude reduction at the two ends and the middle of the pixel positions matches the grain boundaries position. Since the long-live bleaching signal represent the charge carrier population, the assumption that the grain boundaries have more trapping states agrees with the reduced amplitude of such signal. It agrees with de Quillettes's study on the impact of microstructure on local carrier intensity and lifetime<sup>10</sup>.

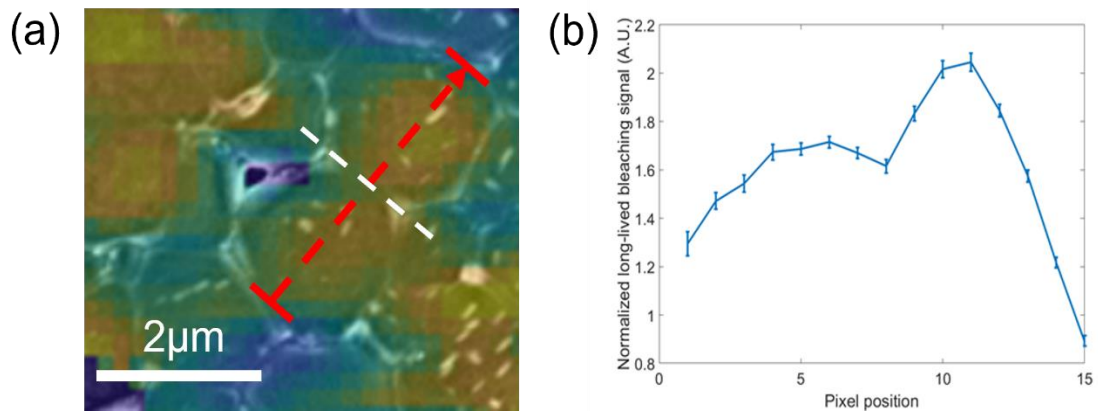


**Figure 34: Long-lived bleaching signal comparison across grains. (a) Combined image between long-lived bleaching signal and SEM. The red arrow shows the grain boundaries of two grains. The signal amplitude of pixels along the red arrow is recorded with error bar in (b).**

### **3.5 Combining FLIM and PPM for the quality evaluation of MAPbI<sub>3</sub> perovskite thin films**

In perovskite solar cells, the ability of creating and transporting excited electrons in perovskite thin films is directly related to the PCE of the whole device. Traditionally, fluorescence signal is widely used to evaluate the quality of perovskite thin films<sup>57, 58</sup>. However, the fluorescence signal only represents population of electrons that recombine radiatively. Instead, the long-lived bleaching signal in pump-probe signal stands for the whole electron population. Therefore, combining the two signals might offer a more justified way to evaluate the quality of perovskite thin films.

As mentioned in the previous sections, the trap-assisted recombination is the dominant recombination process with current power of the pump beam. Both the fluorescence signal and the pump-probe signal are related to the charge carrier population change raised by the trap-assisted recombination in nanosecond scales according to equation 37 and 38. Therefore, the correlation between the band-to-band recombination contribution in the fluorescence signal and the long-lived bleaching signal in the pump-probe signal is used to investigate their ability on representing the local charge carrier population. Figure 35 shows the correlation between the two signals. Each signal is normalized to their mean value. The Pearson correlation coefficient between them is 0.490, which indicates a positive correlation between these two signals. Since the amplitude of both signals has a positive correlation with the whole electron

population, the positive correlation between these signals is expected. However, regions with abnormal ratio between these two signals are also observed.

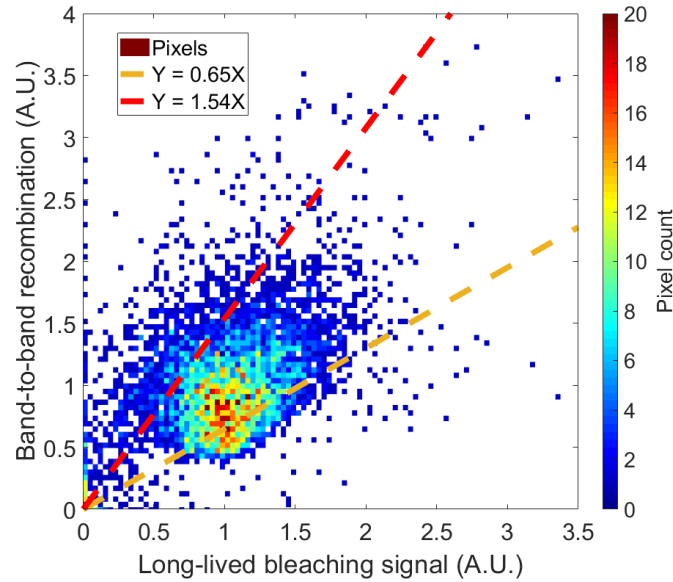


**Figure 35: Correlation plot between the long-live bleaching signal and the band-to-band recombination signal. Both signals are normalized to their mean value. Two dash lines are plotted to separate the regions that have abnormal ratio between the two signals.**

To investigate the spatial distribution of the regions with abnormal ratio between the two signals discussed above, pixels with high and low signal ratio  $R$  (the amplitude of the normalized trap-assisted recombination signal divides by the amplitude of the normalized long-lived bleaching signal) are separately overlapped with the SEM image. Figure 36 shows regions having high ratio between the two signals ( $R > 1.54$ ). These regions correspond to a strong fluorescence signal via the band-to-band recombination but have small charge carrier population indicated by the small amplitude of the long-lived bleaching signal. They mainly distribute around spatial defects.

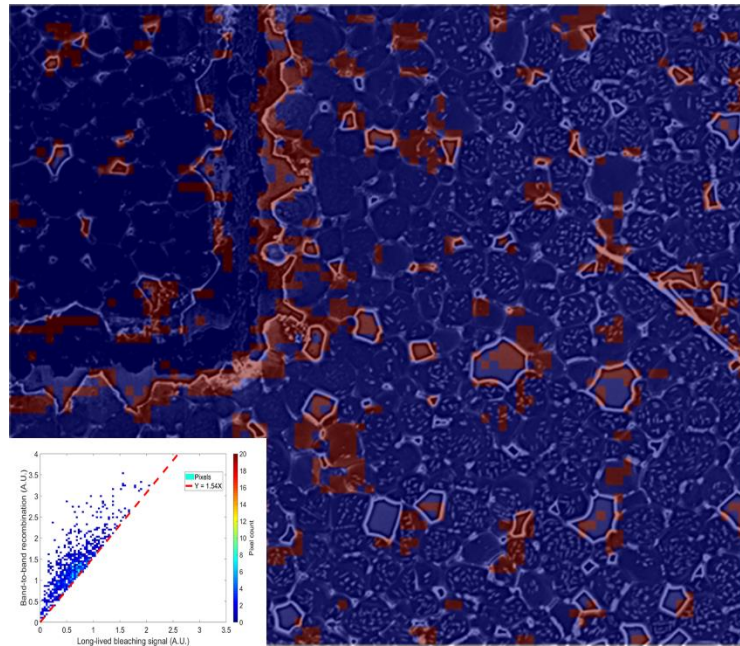


**Figure 36: Spatial distribution of pixels with high ratio ( $R > 1.54$ ) between the band-to-band recombination signal and the long-lived bleaching signal. The high ratio pixels are overlapped with the SEM image and colored in red. Inserts are the corresponding pixel locations in the correlation plot.**

Figure 37 shows low ratio regions ( $R < 0.65$ ), which have large total electron population whereas show little fluorescence signal. They mainly distribute across grains, no strong correlation between grain structure and the distribution of low ratio regions is observed. It might suggest that there are heterogeneities, which cannot be revealed by the sample's morphology, reducing the efficiency of the radiative recombination processes.

These observations indicate that both visible and invisible spatial heterogeneities can hinder the fluorescence signal from accurately representing the population of total electrons. Therefore, solely using fluorescence signal to evaluate the quality of the

perovskite thin films might be inaccurate. However, by combining the pump-probe signal and the fluorescence signal, we can not only accurately monitor the local charge carrier population but also obtain the local efficiency of the radiative recombination processes.

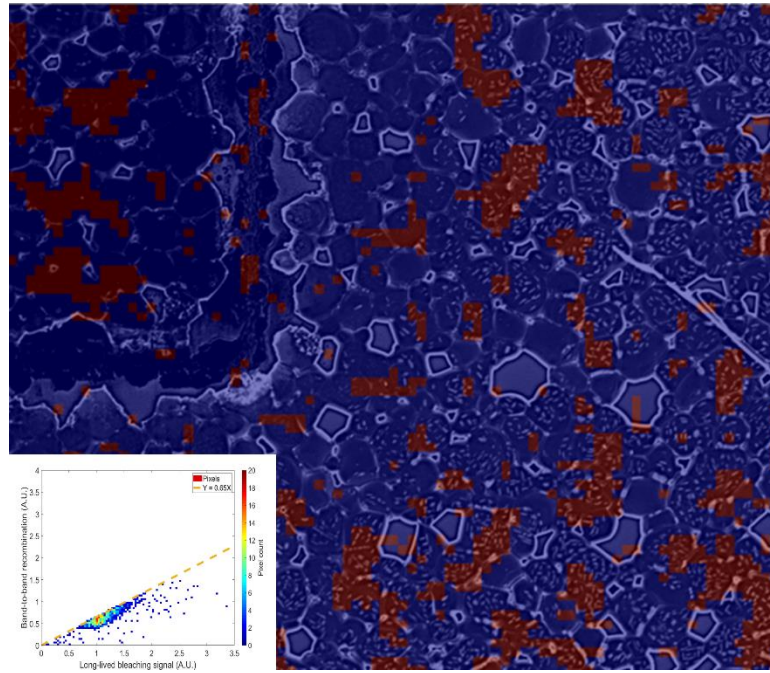


**Figure 37: Spatial distribution of pixels with low ratio ( $R < 0.65$ ) between the band-to-band recombination signal and the long-lived bleaching signal. The low ratio pixels are overlapped with the SEM image and colored in red. Inserts are the corresponding pixel locations in the correlation plot.**

### **3.6 Conclusion**

In this chapter, models for PPM and FLIM data are established. Two radiative recombination processes, which are fast recombination and band-to-band recombination, are separated from the fluorescence signal. The pump-probe signal is decomposed into three charge carrier behaviors: three-photon absorption, rapidly decaying negative

signal, and long-lived bleaching signal. The spatial distribution of each process is compared with the sample's morphology. Correlation between spatial defects and heterogeneities of charge carrier dynamics are revealed. In the end, the inaccuracy of evaluating the quality of perovskite thin films solely by the fluorescence signal is pointed out. The analysis, which combines the spatial distribution of the fluorescence signal and the pump-probe signal, can offer a more justified way to estimate the quality of the MAPbI<sub>3</sub> thin films. Additional information of local efficiency of radiative recombination processes can also be obtained by such analysis.

## **4 Analyzing the hot carrier cooling process in MAPbI<sub>3</sub> thin films by multi-wavelength pump probe microscopy**

### ***4.1 Introduction to hot carrier harvesting in solar cells***

Hot carriers are originally introduced to represent electrons or holes that gain high kinetic energy by an intense electric field in semiconductor devices. In the field of solar cells, hot carriers stand for the excited electrons and holes which have not thermally relaxed to the band edge. For a solar cell, if hot carriers are transported to carrier accept layers before the thermal relaxation, the excess energy above the band edge can be harvested. Figure 38 shows the basic mechanism of the hot carrier harvesting in solar cells. Hot carriers are transported to electrodes through energy selective contact materials, which selectively transport electrons in a small energy range. The energetically narrow contacts greatly reduce the cooling effect inside contacts due to the scattering between electrons with different energy. Charge carriers whose energy is below the selected energy can also be transported by either obtaining more energy via electron-electron scattering in the conduction band or external electric field acceleration<sup>59</sup>. A larger open circuit voltage is achieved by this mechanism compared to the traditional single junction solar cells. Therefore, the PCE of such device can be greatly improved. Theoretically, the optimal efficiency a single junction solar cell can achieve by employing hot carrier harvesting is 66%, which substantially exceeds the 33% Shockley-Queisser limit<sup>60, 61</sup>.

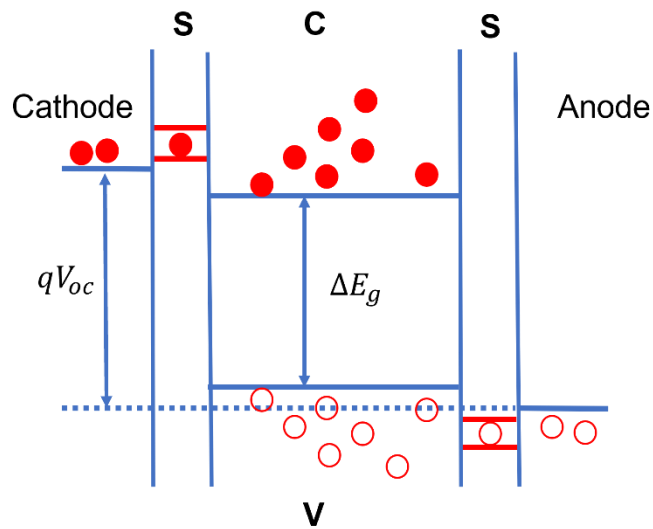


**Figure 38: Mechanism for hot carrier harvesting. S stands for energy selective contacts. C and V are conduction band and valence band, respectively.  $\Delta E_g$  is the band gap energy.  $V_{oc}$  is the open circuit voltage. Solid and hollow circles represent electrons and holes respectively.**

The thermal relaxation ('cooling') process of hot carriers is crucial to the hot carrier harvesting. Fast hot carrier cooling process might lead to the failure of hot carrier transport. Therefore, understanding the hot carrier cooling process is necessary for the design of solar cells employing hot carrier harvesting.

In this chapter, multiple wavelengths are employed as probe beams to investigate the hot carrier cooling process by monitoring charge carrier dynamics of electrons with different energy. Before analyzing the experimental results, the hot carrier cooling model needs to be discussed.

## ***4.2 Hot carrier cooling model***

In our experiment, hot carriers are created by absorbing photons from the pump beam at 817nm. As discussed in the previous chapters, two-photon excitation is the primary process to excite electrons from the valence band to the conduction band. The photon energy (3.04eV) that single electron absorbs is much larger than the band gap energy (1.63eV). It enables the hot carrier cooling process since the energetic electrons will interact with the environment and relax to the energy states near the band edge.

Figure 39 illustrates the hot carrier cooling process. Initially, electrons are excited to reach high energy states in the conduction band. After a fast thermalization among electrons (typically several hundreds of femtoseconds<sup>36</sup>), a quasi-equilibrium distribution is achieved, and the excited electron population follows the Boltzmann distribution. The temperature of electrons ( $T_e$ ) are the same among electrons but higher than the lattice temperature of the sample ( $T_c$ ). Then, the energetic electrons start to interact with phonons in the lattice. The electron-phonon interaction consumes the energy of the excited electrons and dissipates as heat via lattice vibration. As a result, the electron temperature gradually decreases. When the electron temperature is equal to the lattice temperature, the electron-phonon interaction reaches a balance. In this situation, electrons mainly distribute around the band edge and hot carriers now become “cold”.

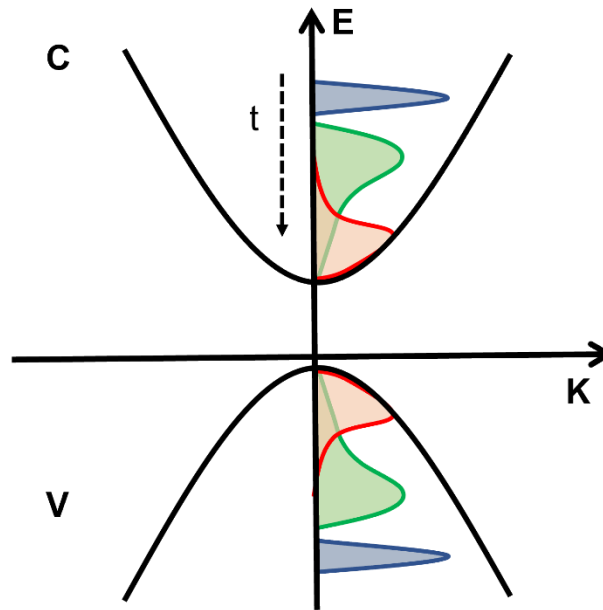


**Figure 39: Hot carrier cooling model. Blue area indicates the initial electron distribution, green and red areas stand for electron distribution during the hot carrier cooling process. V and C represent the valence band and the conduction band respectively.**

To monitor the hot carrier cooling process described above, one straightforward way is to determine the electron population distribution at different time delay after the photon excitation. Since the pump-probe signal can represent the charge carrier population, it is well suited to study the hot carrier cooling process. Broadband pump probe spectroscopy has been widely used to interrogate such process<sup>40</sup>. It provides the average pump-probe signal of the investigated region with a wide range of probe wavelengths. With this method, the spectral analysis of pump-probe signal at different time delays can be realized. However, multiple photoinduced effects can distort the

shape of the spectra of pump-probe signals. The impact of these effects needs to be considered to correctly monitor the hot carrier cooling process.

Figure 40 shows the spectra of pump-probe signals at a series of time delays taken by Libai Huang's group<sup>56</sup>. The MAPbI<sub>3</sub> thin film is excited by the pump beam (400nm) with 3.1 eV photon energy, and a broadband probe beam provides pump-probe signal with photon energy ranging from 1.5 eV to 1.9 eV. The earliest time delay recorded is chosen to be 400 fs to make sure the initial thermalization is finished and electrons distribute with a defined temperature. The positive sign in the figure is assigned to represent reduced absorption and the negative sign stands for the enhanced absorption. The broad bleaching signal at early time reflects the hot carrier distribution. It becomes narrower as the time increases. The change of the spectrum's shape reflects the hot carrier cooling process.

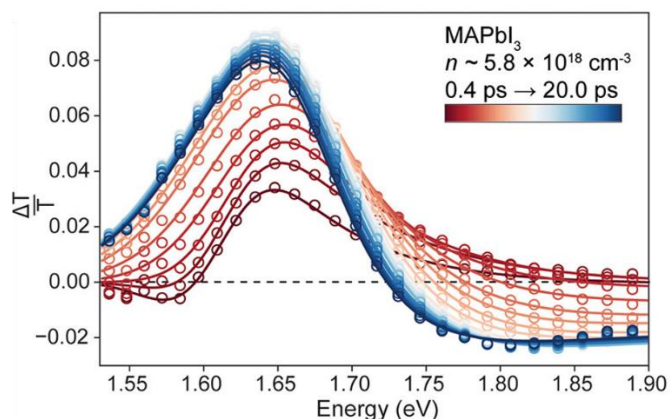


**Figure 40: Spectra of pump-probe signal at different time delays. Adapted with permission from J. W. M. Lim, D. Giovanni, M. Righetto, M. Feng, S. G. Mhaisalkar, N. Mathews and T. C. Sum, *The Journal of Physical Chemistry Letters* 11 (7), 2743-2750 (2020). Copyright 2020, American Chemical Society.**

Other photoinduced effects are also observed in the spectra. The main bleaching peak shown in figure 40 at the large time delay (20ps) is at 1.65 eV, which is close to the band gap energy (1.63 eV). It is associated with the state-filling effect at the band edge due to the thermally relaxed electrons<sup>62-64</sup>. The absorption signal below the band edge at early time is due to the bandgap renormalization: excited electrons and holes have a screening effect on the energy of bound charge carriers, the average charge density felt by single particles are reduced due to the presence of excited electrons and band gap energy is reduced. Therefore, photons with energy less than the original band gap energy are possible to be absorbed due to the existence of excited charge carriers. The absorption signal appears at the high energy end is mainly a result of photoinduced reflectivity changes<sup>40, 56</sup>.

To accurately extract time-dependent temperature of electrons from the pump-probe spectra, all the photoinduced effects need to be considered<sup>56</sup>. However, an approximation can be made at the high energy end of the spectra for temperature estimation<sup>40, 64, 65</sup>:

$$\frac{\Delta T}{T}(E) \propto \exp \frac{E_F - E}{k_b T_e} + R(E) \quad (41)$$

where the  $\Delta T/T(E)$  stands for normalized pump-probe signal with different probe energy  $E$ ,  $E_F$  is the quasi-Fermi energy,  $k_b$  is the Boltzmann constant,  $T_e$  is the electron temperature and  $R(E)$  is the contribution of the photoinduced reflectivity changes to the pump-probe signal. It assumes that the high energy end of the spectra is less affected by

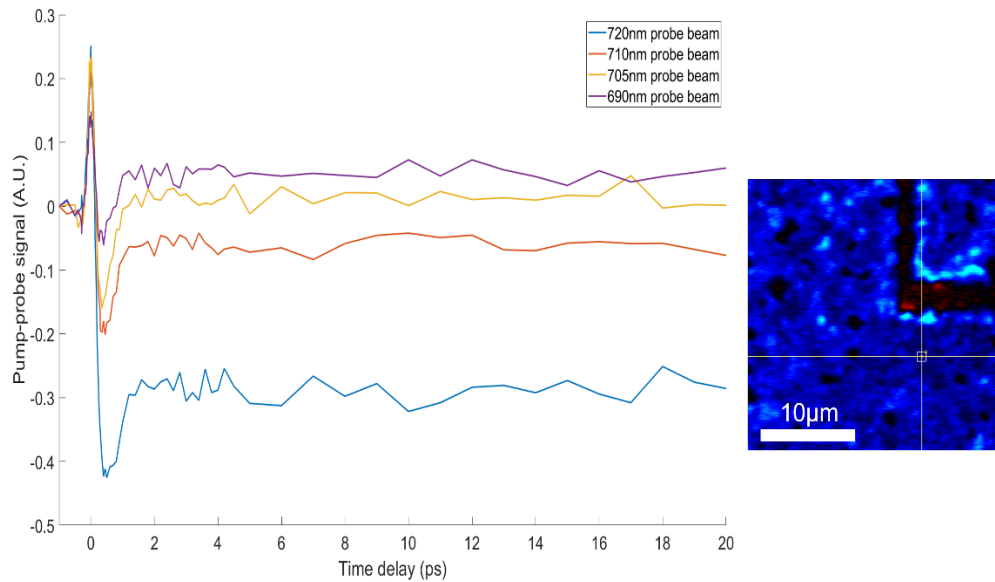
the band renormalization. Therefore, electron distribution in high energy states can be estimated with the Boltzmann distribution.

Utilizing this assumption, the spatially resolved electron temperature can be obtained by our PPM setup. First, a series of PPM data with different wavelengths of the probe beam are measured. Second, the pump-probe traces of the investigated region are selected. Then, the pump-probe signals from different traces, which are at the same time delay are plotted to form the time-resolved spectra. Finally, the spectrum at different time delays is fitted to the Boltzmann distribution and the time-dependent electron temperatures are obtained.

### ***4.3 Spectra of pump-probe signals***

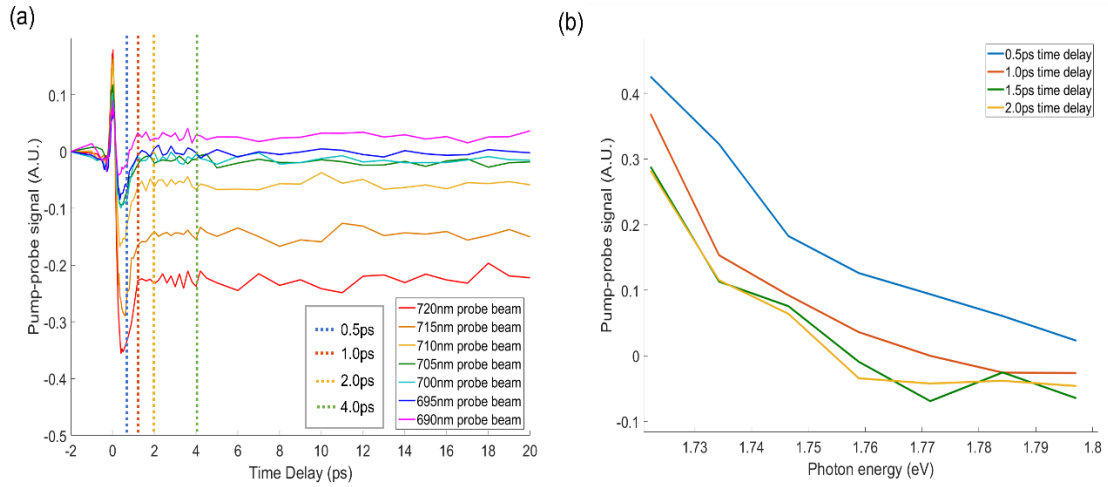
As discussed in the previous section, we obtain a series of PPM data by varying the wavelength of the probe beam from 720nm (1.72 eV) to 690nm (1.80 eV) while keeping the pump beam fixed at 817nm (1.52 eV). The high initial charge carrier density ( $4 \times 10^{17}/cm^3$ ) created by the pump beam via two-photon excitation ensures the hot carrier cooling process can be observed by PPM. In this section, the same sign convention used in chapter 3 for the pump-probe signal is adapted. The positive pump-probe signal stands for enhanced absorption. Before plotting the spectra, an amplitude calibration for each pump-probe signal is made. It is because the spectral filter used to selectively pass the probe beam has different transmittance for different probe beam wavelengths.

Figure 41 illustrates four pump-probe traces of a selected region. Similar charge carrier behaviors are observed as the trace with 745nm probe beam shown in the previous chapter: three-photon absorption, rapidly decaying negative signal, and long-lived bleaching signal. Since high energy states are available in a wide range<sup>66</sup>, three-photon absorption can happen with a wide range of the probe beam wavelengths. Therefore, it is observed in all four pump-probe traces. The rapidly decaying negative signal shown in the pump-probe signal with different probe wavelengths can be understood as the result of the state-filling effect at different energy states due to the hot carrier distribution. As electrons gradually relax to the band edge, the occupation of high energy states is reduced and the bleaching signal due to the state-filling effect will decrease. For the long-lived bleaching signal, it is the result of state-filling effect near the band edge due to the thermally relaxed electrons. It is dominant when probing the energy states close to the band edge. As the probe energy further increases, this signal becomes less significant. Therefore, only the pump-probe traces with 720nm and 710nm probe beams show the long-lived bleaching signal. When the phonon energy of the probe beam rises to 1.76 eV (705nm), little long-lived bleaching signal is observed. When the phonon energy further increases, a long-lived positive signal is observed. It is the result of photoinduced reflectivity changes. This positive signal agrees with the feature at the high energy end of the pump-probe spectra shown in the previous section (figure 40).



**Figure 41: Pump-probe traces with different probe beam wavelengths. Inset shows the selected region.**

In figure 42, pump-probe signals from different probe beam wavelengths are plotted together at the same time delay to obtain the spectra. To better compare the pump-probe spectra with the spectroscopy data shown in figure 40, the sign of the pump-probe spectra is flipped to be consistent with the convention adapted in figure 40. Since the electron temperature is equal to the lattice temperature after thermalization, the same pump-probe spectra are expected for time delays after thermalization. Therefore, the overlapped spectra in figure 42b after 2ps indicates the hot carrier cooling process has finished within the first 2ps.



**Figure 42: Spectra of the pump-probe signal. (a) Pump-probe traces with different probe beam wavelengths. Dash lines show the time delays selected to plot the spectra. (b) Spectra of pump-probe signal at four different time delays. The sign of the pump-probe signal in (b) is flipped to be consistent with the convention adapted in figure 40.**

#### **4.4 Local temperature analysis**

To obtain the electron temperature locally, the pump-probe traces of selected regions will be analyzed. However, the signal to noise ratio (SNR) of the pump-probe traces of a single pixel is too low to accurately extract the electron temperature. Typically, pump-probe traces averaging over an area  $S = 1 \mu\text{m}^2$  have enough SNR to form the accurate spectra and reveal the time-resolved electron temperatures. Therefore, a micrometer scale electron temperature distribution can be obtained.

As discussed in the previous section, the overlapped spectra after 2ps shows the electron distribution with electron temperature equal to the lattice temperature of the sample, which is close to the room temperature (300K). Additionally, according to the previous study<sup>40</sup>, the contribution of photoinduced reflectivity changes to the pump-

probe signal in the photon energy range from 1.72eV to 1.80eV is close to a constant. Therefore,  $R(E)$  in equation 41 can be approximated by a fixed value  $R$ . By fitting the spectra after 2ps with room temperature using equation 41,  $R$  can be obtained. Now, instead of treating  $R$  as a fitting parameter, it can be included as a fixed constant.

Figure 43 shows the fitting result of the spectra and the extracted time-resolved electron temperatures. At early time delay, the electron temperature is high due to the high excitation energy. It gradually drops back to the lattice temperature of the sample in the first 2ps. After 2ps, electrons have cooled down to energy states near the band edge and the electron temperature remains unchanged. The time-resolved temperature shown in figure 43 agrees with the temperature measurement from another group's work<sup>64</sup>.

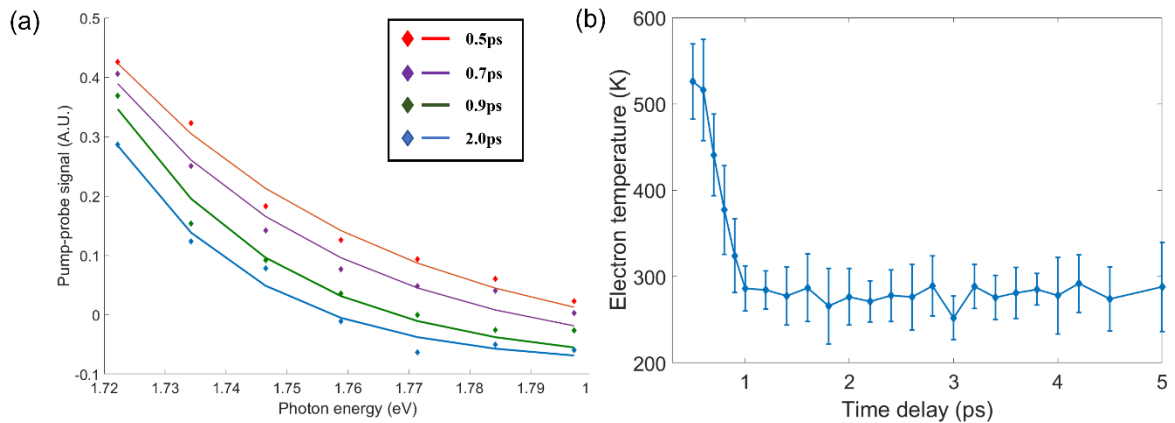


**Figure 43: Spectra of pump-probe signal with fitting result and time-resolved electron temperatures. (a) Spectra from 0.5ps to 2.0ps are plotted as dots. The solid lines show the fitting result. After 2ps, the spectra have similar shape. (b) Temperatures with the error bar at different time delays (from 0.5ps to 5ps) are obtained from the fitting result.**

Applying this method across the sample, an electron temperature map with micrometer spatial resolution can be obtained. Figure 44a shows the amplitude of the pump-probe signal at its negative maximum across the sample. Regions with little signal, which are likely to be spatial defects, are filtered out when extracting temperature. Figure 44b shows the electron temperature map at 0.5ps time delay. Regions with large negative maximum signal shows quite uniform electron temperature at 0.5ps time delay. The unexpected high temperature at 0.5ps observed in regions close to areas which are filtered out might be explained by the poor SNR of the pump-probe signal. Additionally, the hot carrier cooling time ( $\tau_c$ ) can be obtained by fitting the time-resolved temperature trace with an exponential decay. Figure 44c and d show the fitting of one temperature trace and the map of the cooling time across the sample. Regions with large negative maximum signal show similar cooling times.

In this section, I demonstrate that multi-wavelength pump-probe microscopy can be used to obtain electron temperature and hot carrier cooling time with micrometer spatial resolution. However, there are still several limitations of this method, which prevent us from accurately correlating the sample's morphology with the hot carrier cooling process. First, the noisy pump-probe signal of regions close to spatial defects leads to an inaccurate temperature measurement. Second, some regions show an additional increasing negative pump-probe signal after 5ps, which is not considered in our model. The explanation of this additional pump-probe signal is still unrevealed. It

limits us to understand the electron temperature behavior in a larger time scale. Third, the spatial resolution of the temperature map is close to the size of a single grain in the sample. It prevents us from investigating the impact of the grain boundaries to the local temperature. In order to improve these problems, more probe wavelengths and a longer averaging time for data acquisition should be considered in future experiments for better fitting result and spatial resolution.

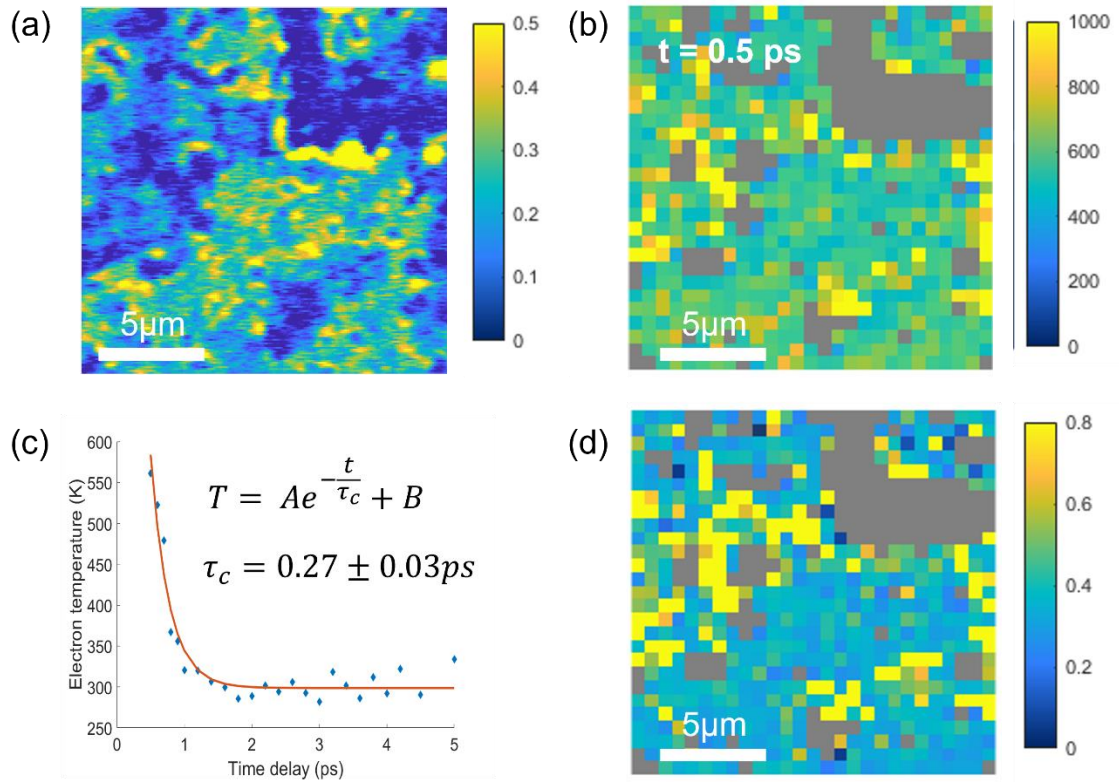


**Figure 44: Electron temperature map at 0.5ps and hot carrier cooling time map.**

Grey regions indicate areas that are filtered out and no temperature is obtained from these regions. (a) Amplitude of the negative maximum value of the pump-probe signal across the sample. Upper right shows the artificial mark created for image registration. (b) Electron temperature map at 0.5ps time delay. (c) Fitting of the electron temperature trace. Hot carrier cooling time,  $\tau_c$ , is obtained. (d) Hot carrier cooling time map.

## **4.5 Conclusion**

In this chapter, the basic concepts of hot carriers and the hot carrier cooling process are discussed. The rapidly decaying negative signal observed in the pump-probe signal is related to the hot cooling process. The multi-wavelength pump probe microscopy is introduced to obtain the spectra of pump-probe signals. By adapting the electron distribution assumption in high energy states, time-resolved electron temperatures and hot carrier cooling time are obtained with micrometer spatial resolution.

## 5 Future research directions and conclusion

In the previous chapters, the ability of PPM to reveal the charge carrier dynamics in the MAPbI<sub>3</sub> thin films is discussed in depth. In this chapter, two potential applications of PPM are discussed to improve the understanding on photovoltaic properties of the perovskite thin films.

### ***5.1 Revealing degradation on MAPbI<sub>3</sub> perovskite thin films by pump probe microscopy***

One major drawback of perovskite thin films is their poor long-term stability<sup>67</sup>. They are prone to degrade when exposed to light illumination, humidity and so on<sup>68,69</sup>. PPM provides a direct way to observe the degradation in perovskite thin films and reveal its impact on the charge carrier dynamics.

To compare the change of carrier dynamics in MAPbI<sub>3</sub> perovskite thin films due to the degradation, the pump-probe signals of two samples are compared. One sample is sealed with epoxy glue to prevent the degradation from oxidation and humidity and another one is unsealed. Both samples are prepared at the same time with the same method. Two samples are placed together for two weeks before acquiring PPM data. The power combination of the pump and probe beams adapted here is the same as the one used in chapter 2. The phasor distributions of their pump-probe signal are shown in figure 45. Both samples show the typical pump-probe features discussed in chapter 2, however, a new type of pump-probe signal is observed in the unsealed sample, which corresponds to an additional phasor location.

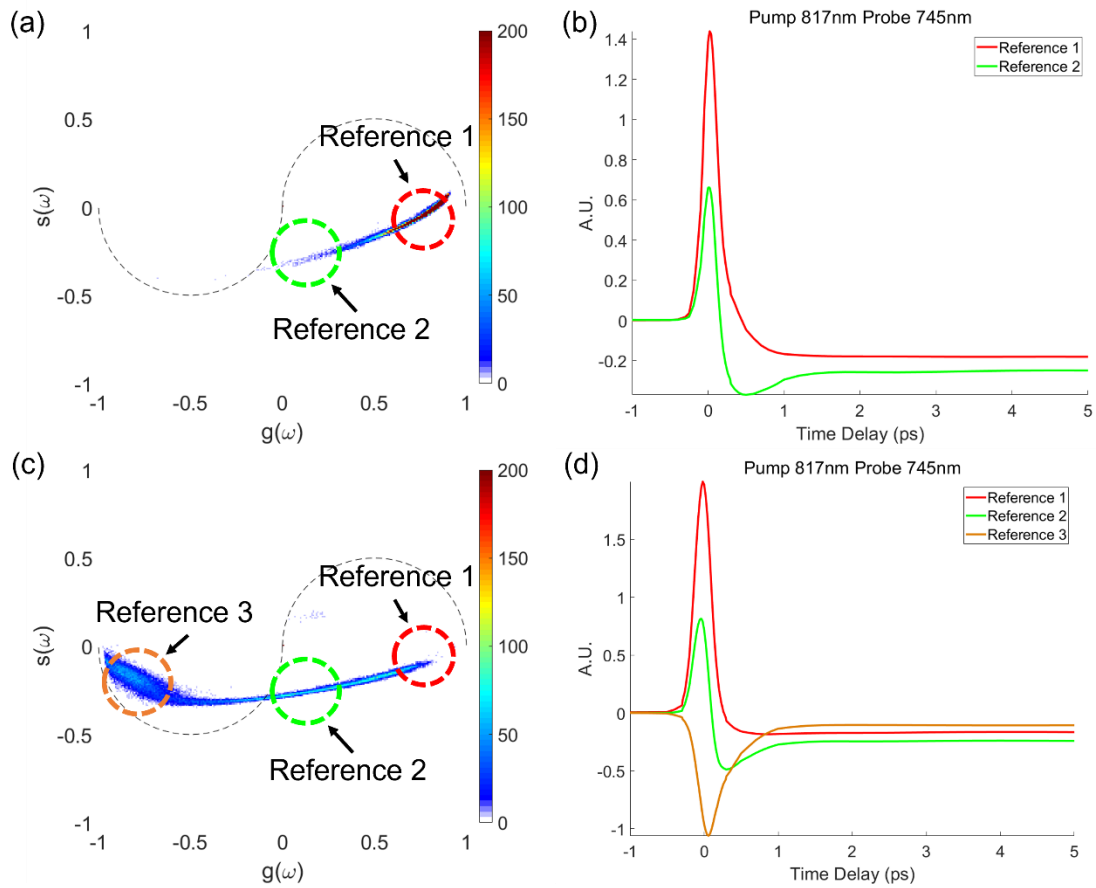


**Figure 45: Phasor plots of pump-probe signal from the sealed and unsealed samples. (a) Phasor plot of the sealed sample, two phasor locations are selected to show their corresponding pump-probe signals. Color bar shows the density of pixels that have the same phasor location. (b) Average pump-probe signals of pixels located in the two phasor locations shown in (a). (c) Phasor plot of the unsealed sample, an additional phasor location is observed. The two selected phasor locations (reference 1 and 2) are the same locations as (a). (d) Average pump-probe signals of pixels located in the three phasor locations shown in (c).**

As shown in figure 45, the pump-probe signals of the sealed sample show the similar phasor distribution to the pump-probe signals of fresh samples shown in chapter 2. It suggests little degradation has happened to the sealed sample after two weeks. However, the unsealed sample clearly shows an additional phasor location (reference 3

in figure 45c), which corresponds to a new type of pump-probe signal. The long-lived bleaching signal of this type of signal is smaller compared to both types of pump-probe signal discussed in the previous chapter. Although the charge carrier dynamics associated with such signal is unclear, its small long-lived bleaching signal suggests the poor capability to maintain charge carrier population for a long time. Therefore, the new appeared pump-probe signal is likely to associate with the degradation raised in the unsealed sample. To better understand the correlation between the degradation of the sample and the change of the sample's charge carrier dynamics, a more careful comparison experiment is required. For example, the sealed and unsealed samples should be imaged at sequential dates after the preparation to track the change of their pump-probe signal. Additionally, mapping the phasor images of the degraded sample with the sample's morphology (obtained by the sample's SEM images) can determine whether the degradation leads to the structural change of the sample.

## ***5.2 Investigating the charge carrier dynamics of MAPbI<sub>3</sub> thin films with different microstructures***

Depending on the fabrication methods, multiple types of MAPbI<sub>3</sub> thin films with different microstructures can be prepared<sup>32, 70</sup>. The combination of PPM and SEM offers a direct way to investigate the impact of different microstructures on the charge carrier dynamics of MAPbI<sub>3</sub> thin films.

As discussed in chapter 2 and 3, the sample's morphology can be associated with local charge carrier dynamics by mapping the signatures of pump-probe signal (phasor

images or fitting parameters) with the SEM images. This method also works for MAPbI<sub>3</sub> thin films with different microstructures. Figure 46 illustrates the correlation between local charge carrier dynamics, which are sorted by phasor images of their corresponding pump-probe signal, and samples' morphology. Two samples with granular and fibrous microstructures are shown. The sorted charge carrier dynamics exhibit granular distribution (figure 46a, c) in the sample with granular microstructure. For the sample with fibrous microstructure, the sorted charge carrier dynamics seems to distribute in different fibers shown in figure 46e.

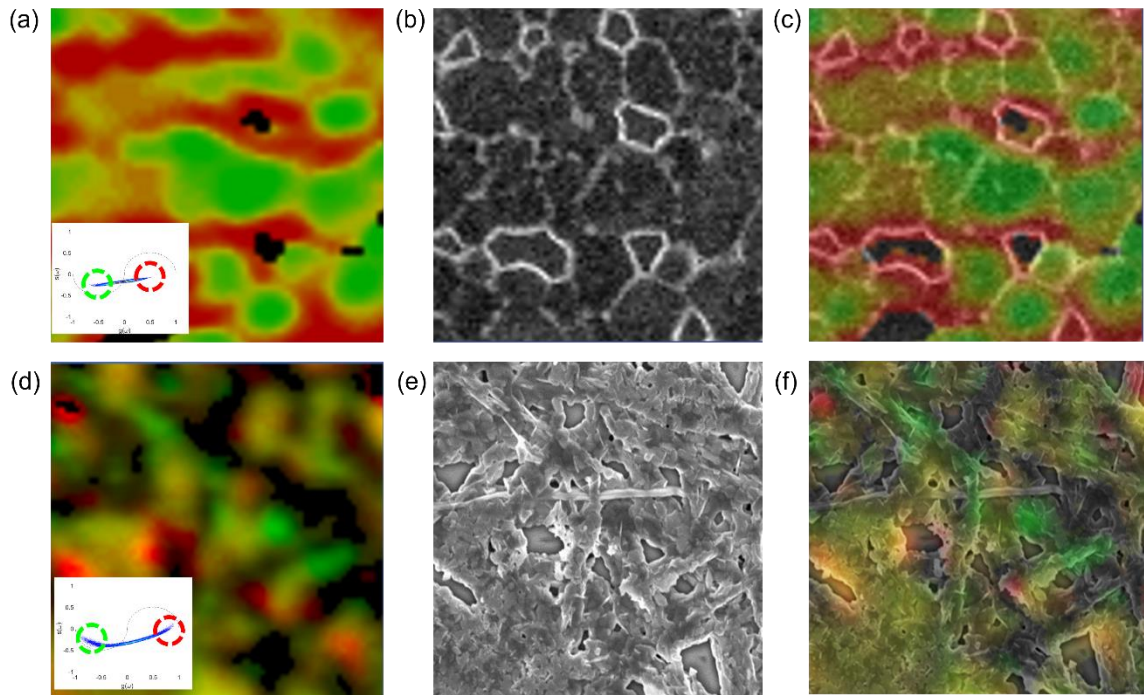


**Figure 46: Phasor, SEM, and combined images of MAPbI<sub>3</sub> samples. Insets are the phasor distribution of the pump-probe signal of each sample. (a-c) Phasor, SEM, and combined images of the sample with a granular microstructure. (d-f) Phasor, SEM, and combined images of the sample with a fibrous microstructure.**

To further investigate the impact of samples' microstructures on the spatial distribution of different charge carrier dynamics, a careful analysis of charge carrier dynamics on different parts of the microstructures, such as grain boundaries in the granular structure, the tips and the middle parts of the fibrous structure, is required. The model introduced in chapter 3 can also offer a more detailed analysis on each charge carrier dynamic.

### **5.3 Conclusion**

In this dissertation, I demonstrate the use of optical microscopy methods to better understand the different charge carrier dynamics of MAPbI<sub>3</sub> thin films.

In chapter 2, I show the observation of spatial heterogeneity of charge carrier dynamics in picosecond time scales of MAPbI<sub>3</sub> thin films. The adjusted phasor analysis is introduced to qualitatively identify the different types of charge carrier dynamics. A false color image is generated to represent the spatial distribution of each type of the charge carrier dynamics. With the help of SEM, the spatial distribution of charge carrier dynamics is related with the sample's morphology. Spatial defects are found to be responsible for the heterogeneity of charge carrier dynamics and related with abundant trapping states. The observation of the fluorescence signal obtained by FLIM supports this conclusion.

In chapter 3, models are introduced to decompose the fluorescence signal and the pump-probe signal. Each decomposed signal corresponds to a charge carrier dynamic.

The fluorescence signal consists of contributions from the fast recombination and the band-to-band recombination. The pump-probe signal is separated into three charge carrier dynamics: three-photon absorption, rapidly decaying negative signal due to the hot carrier cooling process and long-lived bleaching signal representing the state-filling effect near the band edge. The long-lived bleaching signal is used to represent the charge carrier population. The pixel-by-pixel fittings of the pump-probe signal and fluorescence signal are achieved. The spatial distribution of each charge carrier dynamic is compared with the sample's morphology. The spatial distribution of the long-lived bleaching signal and the band-to-band recombination signal shows an anti-correlation with the spatial defects such as pinholes. The reduction of these two signals can be explained by the large charge carrier injection from the band edge to the trapping states. Therefore, it suggests that the spatial defects are likely to obtain abundant trapping states, which reduce the charge carrier population in the conduction band and is detrimental to the PCE of the thin films. Additionally, the grain boundaries in the thin films are also associated with abundant trapping states. In the end, I show that the combination of the fluorescence signal and the pump-probe signal can offer a more justified way to evaluate the quality of the MAPbI<sub>3</sub> thin films.

In chapter 4, the hot carrier cooling process is introduced. I demonstrate that the rapidly decaying negative signal, which is decomposed from the pump-probe signal, can monitor the hot carrier cooling process. By varying the probing wavelength, the

time-resolved pump-probe spectra can be obtained. I show that the time-dependent electron temperature can be obtained by fitting the pump-probe spectra with the Boltzmann distribution. With the spatial resolution offered by the PPM, the local electron temperature change during the hot carrier cooling process can be resolved.

In chapter 5, I discuss two potential research directions of applying PPM to investigate the perovskite thin films. With the help of PPM, the impact of the sample's degradation and microstructure on the sample's charge carrier dynamics could be unveiled.

## Appendix A: Power study of the pump-probe signal

The pump intensity dependence of the instantaneous peak is plotted in figure 47a. Since the absorption signal is dominant at 0ps at regions due to the time delay constant  $t_0$  associated with the rapidly decaying negative signal and the long-lived negative signal, the peak value is used to represent the amplitude of the absorption signal. The natural logarithm of the pump power  $P$  and the peak value  $T$  is plotted in figure 47b and used to obtain a linear regression line. The slope is  $0.84 \pm 0.25$ , which agrees with the assumption of the linear dependence of the instantaneous peak on the pump power.

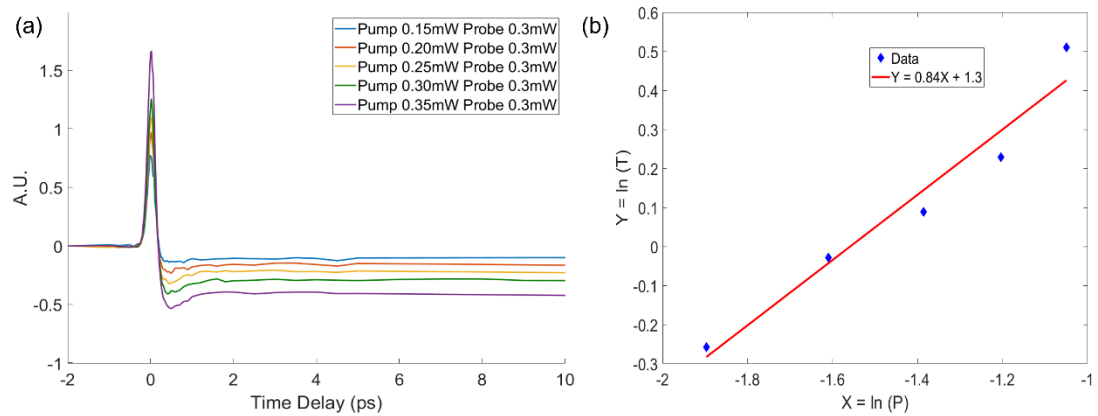


**Figure 47: Pump power dependence of the instantaneous peak. (a) Pump-probe signal with different pump power. The probe power is fixed. (b) Linear regression of the natural logarithm of the pump power  $P$  and the peak value  $T$ . The standard error of the slope is 0.25.**

The same analysis is applied to study the probe intensity dependence of the instantaneous peak. Figure 48 shows the data and the linear regression of the data. The

slope is  $1.71 \pm 0.17$ , which agrees with the assumption of the quadratic dependence of the instantaneous peak on the probe power.

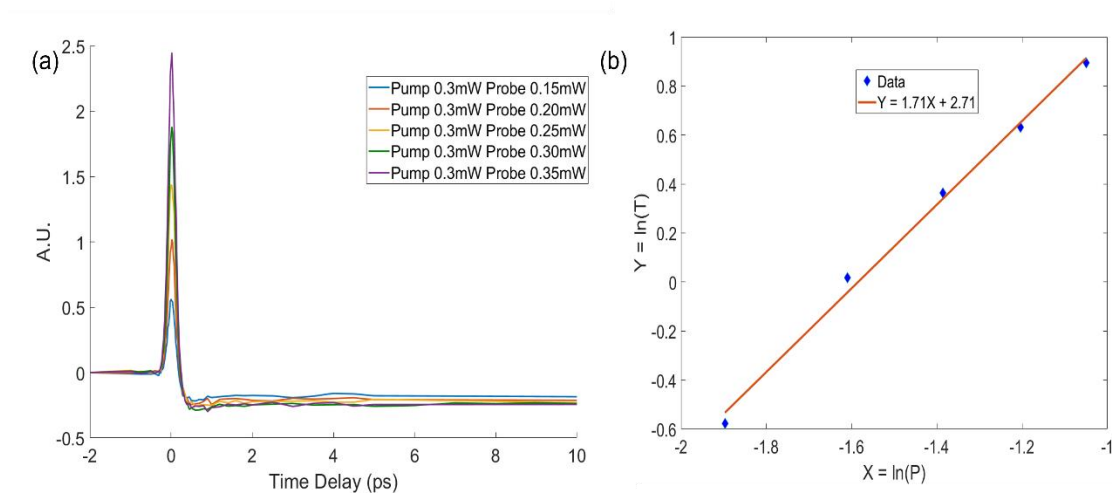


**Figure 48: Probe power dependence of the instantaneous peak. (a) Pump-probe signal with different probe power. The pump power is fixed. (b) Linear regression of the natural logarithm of the probe power  $P$  and the peak value  $T$ . The standard error of the slope is 0.17.**

For the long-live bleaching signal, its amplitude is represented by averaging the pump-probe signal from 2ps to 10ps. Figure 49 shows the quadratic intensity dependence of the long-lived bleaching signal on the pump power and figure 50 shows the linear intensity dependence on the probe power. The slope of the linear regression is  $1.76 \pm 0.36$  for the power study of the pump beam and  $0.98 \pm 0.32$  for the power study of the probe beam. These results agree with the fact that we are utilizing two-photon absorption to excite electrons.

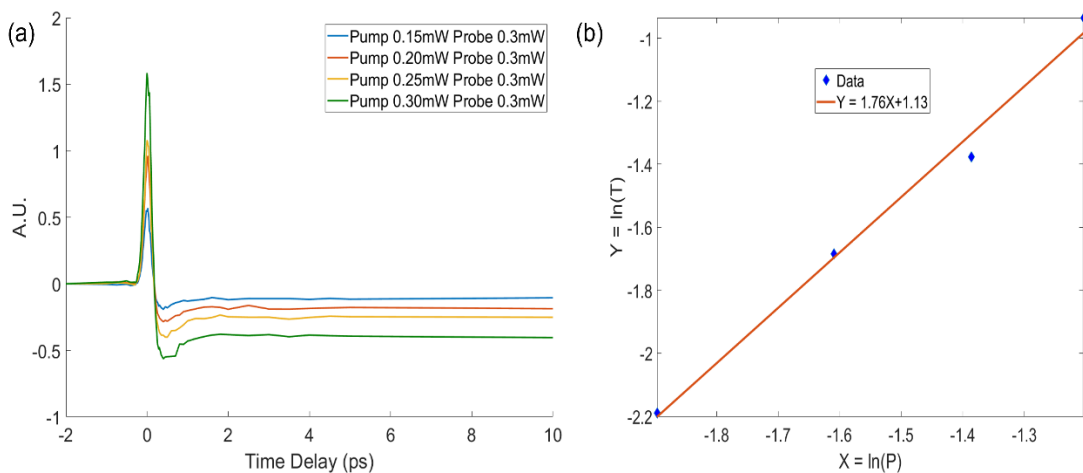


**Figure 49: Pump power dependence of the long-lived bleaching signal. (a) Pump-probe signal with different pump power. The probe power is fixed. (b) Linear regression of the natural logarithm of the pump power  $P$  and the peak value  $T$ . The standard error of the slope is 0.36.**

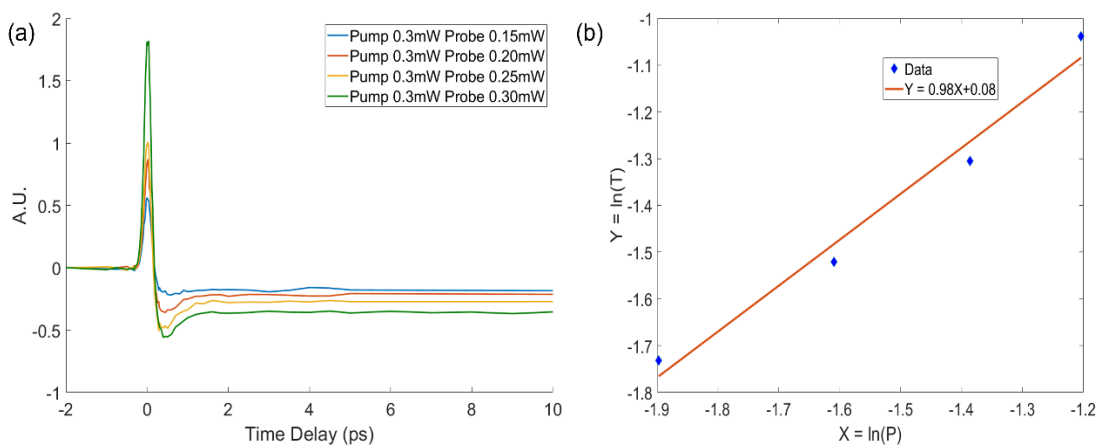


**Figure 50: Probe power dependence of the long-lived bleaching signal. (a) Pump-probe signal with different probe power. The pump power is fixed. (b) Linear regression of the natural logarithm of the probe power  $P$  and the peak value  $T$ . The standard error of the slope is 0.32.**

## Appendix B: Single pixel fitting of PPM and FLIM

As mentioned in chapter 3, the single pixel fitting is achieved for both PPM data and FLIM data. Figure 51 shows fitting result of the pump-probe signal of individual pixels. Figure 52 shows the fitting result of the fluorescence signal of individual pixels.

The fitting parameters and associated standard errors of both fittings are listed in table 5.

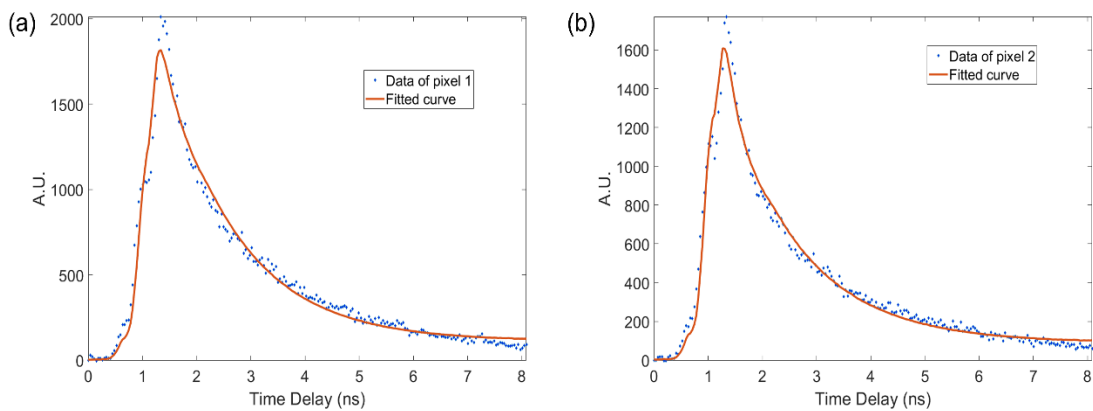


**Figure 51: Single pixel fitting of the fluorescence signal. Two random pixels are selected to plot their corresponding fluorescence signals and fitting curves.**

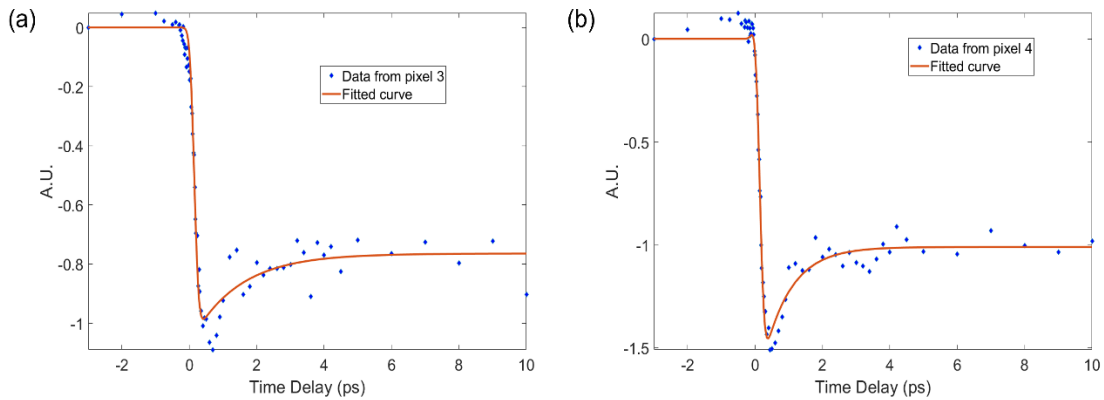


**Figure 52: Single pixel fitting of the pump-probe signal in picosecond scales. Two random pixels are selected to plot their corresponding pump-probe signals in the first 10 ps and fitting curves.**

**Table 4: Fitting parameters of individual pixels**

Fluorescence	$\beta_f$ (A.U.)	$\beta_b$ (A.U.)	$\tau_b$ (ns)	$\beta_o$ (A.U.)	
Pixel 1	780.3 $\pm$ 27.3	167.1 $\pm$ 3.2	1.33 $\pm$ 0.05	8.75 $\pm$ 0.93	
Pixel 2	928.9 $\pm$ 21.5	122.3 $\pm$ 2.5	1.37 $\pm$ 0.05	6.98 $\pm$ 0.76	
Pump-probe	$\alpha_t$ (A.U.)	$\alpha_r$ (A.U.)	$\alpha_l$ (A.U.)	$\tau$ (ps)	$t_0$ (ps)
Pixel 3	0 $\pm$ 3.66	-7.92 $\pm$ 1.43	-22.01 $\pm$ 0.52	1.40 $\pm$ 0.15	0.15 $\pm$ 0.01
Pixel 4	7.61 $\pm$ 3.49	-17.85 $\pm$ 1.03	-29.09 $\pm$ 0.70	0.81 $\pm$ 0.51	0.15 $\pm$ 0.01

## Appendix C: Information of MAPbI<sub>3</sub> thin films

The MAPbI<sub>3</sub> thin films used in our experiments are supplied by two corporation groups: Prof. David Mitzi's group from Duke and Prof. Clemens Burda's group from Case Western Reserve University. The samples described in this dissertation are uncovered samples. We measure all the information at the same day that it is fabricated. Therefore, we assume no significant degradation has happened to the samples, the heterogeneity is from the fabrication process. Figure 53 shows the typical morphology of our samples.

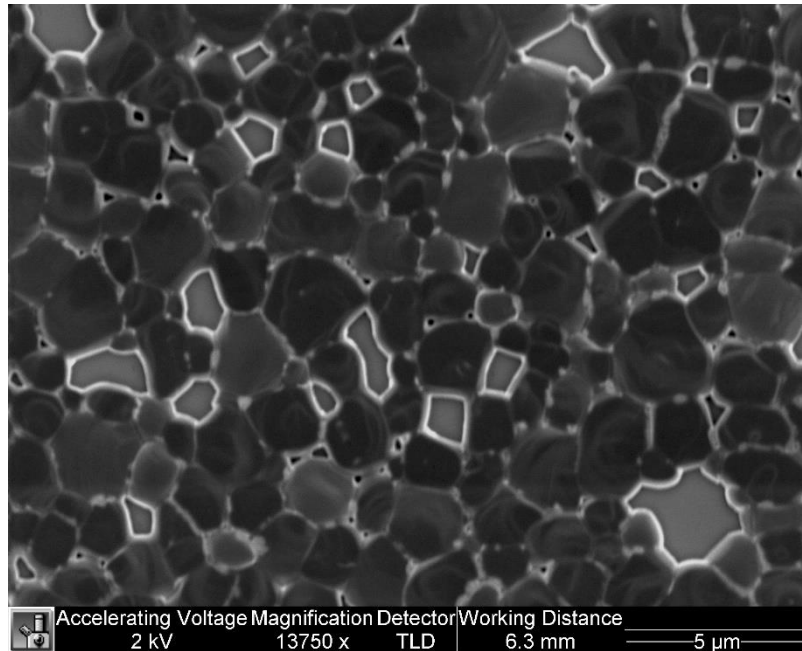


**Figure 53: SEM image of MAPbI<sub>3</sub> thin films used in our experiments. The gray areas are pinholes formed during the fabrication process.**

## Reference

1. Jeong, J.; Kim, M.; Seo, J.; Lu, H.; Ahlawat, P.; Mishra, A.; Yang, Y.; Hope, M. A.; Eickemeyer, F. T.; Kim, M.; Yoon, Y. J.; Choi, I. W.; Darwich, B. P.; Choi, S. J.; Jo, Y.; Lee, J. H.; Walker, B.; Zakeeruddin, S. M.; Emsley, L.; Rothlisberger, U.; Hagfeldt, A.; Kim, D. S.; Grätzel, M.; Kim, J. Y., Pseudo-halide anion engineering for  $\alpha$ -FAPbI<sub>3</sub> perovskite solar cells. *Nature* **2021**, 592 (7854), 381-385.
2. Gaonkar, H.; Zhu, J.; Kottokaran, R.; Bhageri, B.; Noack, M.; Dalal, V., Thermally Stable, Efficient, Vapor Deposited Inorganic Perovskite Solar Cells. *ACS Applied Energy Materials* **2020**, 3 (4), 3497-3503.
3. Yin, J.; Naphade, R.; Gutiérrez Arzaluz, L.; Brédas, J.-L.; Bakr, O. M.; Mohammed, O. F., Modulation of Broadband Emissions in Two-Dimensional (100)-Oriented Ruddlesden–Popper Hybrid Perovskites. *ACS Energy Letters* **2020**, 5 (7), 2149-2155.
4. Jiang, X. Transient Absorption Microscopy Study of Excited-State Dynamics and the Structural Origins in Metal Halide Perovskites. Ph.D., Northwestern University, Ann Arbor, 2021.
5. Zhu, T.; Snaider, J. M.; Yuan, L.; Huang, L., Ultrafast Dynamic Microscopy of Carrier and Exciton Transport. *Annual Review of Physical Chemistry* **2019**, 70 (1), 219-244.
6. Simpson, M. J.; Doughty, B.; Yang, B.; Xiao, K.; Ma, Y.-Z., Imaging Electronic Trap States in Perovskite Thin Films with Combined Fluorescence and Femtosecond Transient Absorption Microscopy. *The Journal of Physical Chemistry Letters* **2016**, 7 (9), 1725-1731.
7. Li, W.; Yadavalli, S. K.; Lizarazo-Ferro, D.; Chen, M.; Zhou, Y.; Padture, N. P.; Zia, R., Subgrain Special Boundaries in Halide Perovskite Thin Films Restrict Carrier Diffusion. *ACS Energy Letters* **2018**, 3 (11), 2669-2670.
8. Foley, B. J.; Cuthriell, S.; Yazdi, S.; Chen, A. Z.; Guthrie, S. M.; Deng, X.; Giri, G.; Lee, S.-H.; Xiao, K.; Doughty, B.; Ma, Y.-Z.; Choi, J. J., Impact of Crystallographic

Orientation Disorders on Electronic Heterogeneities in Metal Halide Perovskite Thin Films. *Nano Letters* **2018**, *18* (10), 6271-6278.

9. Draguta, S.; Thakur, S.; Morozov, Y. V.; Wang, Y.; Manser, J. S.; Kamat, P. V.; Kuno, M., Spatially Non-uniform Trap State Densities in Solution-Processed Hybrid Perovskite Thin Films. *The Journal of Physical Chemistry Letters* **2016**, *7* (4), 715-721.

10. de Quilletes, D. W.; Vorpahl, S. M.; Stranks, S. D.; Nagaoka, H.; Eperon, G. E.; Ziffer, M. E.; Snaith, H. J.; Ginger, D. S., Impact of microstructure on local carrier lifetime in perovskite solar cells. *Science* **2015**, *348* (6235), 683-686.

11. deQuilletes, D. W.; Jariwala, S.; Burke, S.; Ziffer, M. E.; Wang, J. T. W.; Snaith, H. J.; Ginger, D. S., Tracking Photoexcited Carriers in Hybrid Perovskite Semiconductors: Trap-Dominated Spatial Heterogeneity and Diffusion. *ACS Nano* **2017**, *11* (11), 11488-11496.

12. Vrućinić, M.; Matthiesen, C.; Sadhanala, A.; Divitini, G.; Cacovich, S.; Dutton, S. E.; Ducati, C.; Atatüre, M.; Snaith, H.; Friend, R. H.; Sirringhaus, H.; Deschler, F., Local Versus Long-Range Diffusion Effects of Photoexcited States on Radiative Recombination in Organic–Inorganic Lead Halide Perovskites. *Advanced Science* **2015**, *2* (9), 1500136.

13. Galkowski, K.; Mitioglu, A. A.; Surrente, A.; Yang, Z.; Maude, D. K.; Kossacki, P.; Eperon, G. E.; Wang, J. T. W.; Snaith, H. J.; Plochocka, P.; Nicholas, R. J., Spatially resolved studies of the phases and morphology of methylammonium and formamidinium lead tri-halide perovskites. *Nanoscale* **2017**, *9* (9), 3222-3230.

14. Draguta, S.; Christians, J. A.; Morozov, Y. V.; Mucunzi, A.; Manser, J. S.; Kamat, P. V.; Luther, J. M.; Kuno, M., A quantitative and spatially resolved analysis of the performance-bottleneck in high efficiency, planar hybrid perovskite solar cells. *Energy & Environmental Science* **2018**, *11* (4), 960-969.

15. Hovel, H. J., Solar cells. *NASA STI/Recon Technical Report A* **1975**, *76*, 20650.

16. Yin, W.-J.; Yang, J.-H.; Kang, J.; Yan, Y.; Wei, S.-H., Halide perovskite materials for solar cells: a theoretical review. *Journal of Materials Chemistry A* **2015**, 3 (17), 8926-8942.
17. Yu, L.; Kokenyesi, R. S.; Keszler, D. A.; Zunger, A., Inverse Design of High Absorption Thin-Film Photovoltaic Materials. *Advanced Energy Materials* **2013**, 3 (1), 43-48.
18. Kittel, C.; McEuen, P.; McEuen, P., *Introduction to solid state physics*. Wiley New York: 1996; Vol. 8.
19. Zhu, H.; Miyata, K.; Fu, Y.; Wang, J.; Joshi, P. P.; Niesner, D.; Williams, K. W.; Jin, S.; Zhu, X.-Y., Screening in crystalline liquids protects energetic carriers in hybrid perovskites. *Science* **2016**, 353 (6306), 1409-1413.
20. Li, M.; Bhaumik, S.; Goh, T. W.; Kumar, M. S.; Yantara, N.; Grätzel, M.; Mhaisalkar, S.; Mathews, N.; Sum, T. C., Slow cooling and highly efficient extraction of hot carriers in colloidal perovskite nanocrystals. *Nature Communications* **2017**, 8 (1), 14350.
21. Stranks, S. D.; Eperon, G. E.; Grancini, G.; Menelaou, C.; Alcocer, M. J. P.; Leijtens, T.; Herz, L. M.; Petrozza, A.; Snaith, H. J., Electron-Hole Diffusion Lengths Exceeding 1 Micrometer in an Organometal Trihalide Perovskite Absorber. *Science* **2013**, 342 (6156), 341-344.
22. Yang, J.; Wen, X.; Xia, H.; Sheng, R.; Ma, Q.; Kim, J.; Tapping, P.; Harada, T.; Kee, T. W.; Huang, F.; Cheng, Y.-B.; Green, M.; Ho-Baillie, A.; Huang, S.; Shrestha, S.; Patterson, R.; Conibeer, G., Acoustic-optical phonon up-conversion and hot-phonon bottleneck in lead-halide perovskites. *Nature Communications* **2017**, 8 (1), 14120.
23. Wehrenfennig, C.; Liu, M.; Snaith, H. J.; Johnston, M. B.; Herz, L. M., Charge-carrier dynamics in vapour-deposited films of the organolead halide perovskite CH<sub>3</sub>NH<sub>3</sub>PbI<sub>3</sub>-xCl<sub>x</sub>. *Energy & Environmental Science* **2014**, 7 (7), 2269-2275.

24. Arvizu, D. E.; Edenburn, M. W. *Overview of photovoltaic concentrator technology*; January 01, 1984, 1984; p 19539.
25. Octavi Semonin, J. M. L. a. M. C. B., Multiple exciton generation in a quantum dot solar cell. *SPIE Newsroom* 2012.
26. König, D.; Casalenuovo, K.; Takeda, Y.; Conibeer, G.; Guillemoles, J. F.; Patterson, R.; Huang, L. M.; Green, M. A., Hot carrier solar cells: Principles, materials and design. *Physica E: Low-dimensional Systems and Nanostructures* **2010**, 42 (10), 2862-2866.
27. Song, Z.; McElvany, C. L.; Phillips, A. B.; Celik, I.; Krantz, P. W.; Waththage, S. C.; Liyanage, G. K.; Apul, D.; Heben, M. J., A techno-economic analysis of perovskite solar module manufacturing with low-cost materials and techniques. *Energy & Environmental Science* **2017**, 10 (6), 1297-1305.
28. Becker, W., *Advanced time-correlated single photon counting techniques*. Springer Science & Business Media: 2005; Vol. 81.
29. O'Connor, D., *Time-correlated single photon counting*. Academic Press: 2012.
30. Yguerabide, J., [24] Nanosecond fluorescence spectroscopy of macromolecules. In *Methods in enzymology*, Elsevier: 1972; Vol. 26, pp 498-578.
31. Becker, W., The bh TCSPC Handbook: Becker & Hickl. <http://www.becker-hickl.de>.
32. Yu, J.; Li, Z.; Liao, Y.; Kolodziej, C.; Kuyuldar, S.; Warren, W. S.; Burda, C.; Fischer, M. C., Probing the Spatial Heterogeneity of Carrier Relaxation Dynamics in CH<sub>3</sub>NH<sub>3</sub>PbI<sub>3</sub> Perovskite Thin Films with Femtosecond Time - Resolved Nonlinear Optical Microscopy. *Advanced Optical Materials* **2019**, 7 (22), 1901185.
33. Simpson, M. J.; Doughty, B.; Yang, B.; Xiao, K.; Ma, Y.-Z., Spatial Localization of Excitons and Charge Carriers in Hybrid Perovskite Thin Films. *The Journal of Physical Chemistry Letters* **2015**, 6 (15), 3041-3047.

34. Lee, J.-W.; Bae, S.-H.; De Marco, N.; Hsieh, Y.-T.; Dai, Z.; Yang, Y., The role of grain boundaries in perovskite solar cells. *Materials Today Energy* **2018**, *7*, 149-160.
35. Snaider, J. M.; Guo, Z.; Wang, T.; Yang, M.; Yuan, L.; Zhu, K.; Huang, L., Ultrafast Imaging of Carrier Transport across Grain Boundaries in Hybrid Perovskite Thin Films. *ACS Energy Letters* **2018**, *3* (6), 1402-1408.
36. Hill, A. H.; Kennedy, C. L.; Massaro, E. S.; Grumstrup, E. M., Perovskite Carrier Transport: Disentangling the Impacts of Effective Mass and Scattering Time Through Microscopic Optical Detection. *The Journal of Physical Chemistry Letters* **2018**, *9* (11), 2808-2813.
37. Guo, Z.; Wan, Y.; Yang, M.; Snaider, J.; Zhu, K.; Huang, L., Long-range hot-carrier transport in hybrid perovskites visualized by ultrafast microscopy. *Science* **2017**, *356* (6333), 59-62.
38. Blach, D. D.; Zheng, W.; Liu, H.; Pan, A.; Huang, L., Carrier Transport Across a CdS<sub>x</sub>Se<sub>1-x</sub> Lateral Heterojunction Visualized by Ultrafast Microscopy. *The Journal of Physical Chemistry C* **2020**, *124* (21), 11325-11332.
39. Wang, T.; Fu, Y.; Jin, L.; Deng, S.; Pan, D.; Dong, L.; Jin, S.; Huang, L., Phenethylammonium Functionalization Enhances Near-Surface Carrier Diffusion in Hybrid Perovskites. *Journal of the American Chemical Society* **2020**, *142* (38), 16254-16264.
40. Price, M. B.; Butkus, J.; Jellicoe, T. C.; Sadhanala, A.; Briane, A.; Halpert, J. E.; Broch, K.; Hodgkiss, J. M.; Friend, R. H.; Deschler, F., Hot-carrier cooling and photoinduced refractive index changes in organic-inorganic lead halide perovskites. *Nature Communications* **2015**, *6* (1), 8420.
41. Manser, J. S.; Kamat, P. V., Band filling with free charge carriers in organometal halide perovskites. *Nature Photonics* **2014**, *8* (9), 737-743.
42. sharma, V.; Aharon, S.; Gdor, I.; Yang, C.; Etgar, L.; Ruhman, S., New insights into exciton binding and relaxation from high time resolution ultrafast spectroscopy of

CH<sub>3</sub>NH<sub>3</sub>PbI<sub>3</sub> and CH<sub>3</sub>NH<sub>3</sub>PbBr<sub>3</sub> films. *Journal of Materials Chemistry A* **2016**, *4* (9), 3546-3553.

43. Elliott, R. J.; Gibson, A. F., *An introduction to solid state physics and its applications*. Barnes & Noble: 1974.

44. Hickey, C. L.; Grumstrup, E. M., Direct Correlation of Charge Carrier Transport to Local Crystal Quality in Lead Halide Perovskites. *Nano Letters* **2020**, *20* (7), 5050-5056.

45. Piland, G.; Grumstrup, E. M., High-Repetition Rate Broadband Pump-Probe Microscopy. *The Journal of Physical Chemistry A* **2019**, *123* (40), 8709-8716.

46. Fischer, M. C.; Wilson, J. W.; Robles, F. E.; Warren, W. S., Invited Review Article: Pump-probe microscopy. *Review of Scientific Instruments* **2016**, *87* (3), 031101.

47. Stringari, C.; Cinquin, A.; Cinquin, O.; Digman, M. A.; Donovan, P. J.; Gratton, E., Phasor approach to fluorescence lifetime microscopy distinguishes different metabolic states of germ cells in a live tissue. *Proceedings of the National Academy of Sciences* **2011**, *108* (33), 13582-13587.

48. Digman, M. A.; Caiolfa, V. R.; Zamai, M.; Gratton, E., The Phasor Approach to Fluorescence Lifetime Imaging Analysis. *Biophysical Journal* **2008**, *94* (2), L14-L16.

49. Robles, F. E.; Wilson, J. W.; Fischer, M. C.; Warren, W. S., Phasor analysis for nonlinear pump-probe microscopy. *Opt. Express* **2012**, *20* (15), 17082-17092.

50. Ganeev, R. A.; Rao, K. S.; Yu, Z.; Yu, W.; Yao, C.; Fu, Y.; Zhang, K.; Guo, C., Strong nonlinear absorption in perovskite films. *Opt. Mater. Express* **2018**, *8* (6), 1472-1483.

51. Wehrenfennig, C.; Eperon, G. E.; Johnston, M. B.; Snaith, H. J.; Herz, L. M., High Charge Carrier Mobilities and Lifetimes in Organolead Trihalide Perovskites. *Advanced Materials* **2014**, *26* (10), 1584-1589.

52. Yamada, Y.; Nakamura, T.; Endo, M.; Wakamiya, A.; Kanemitsu, Y., Photocarrier Recombination Dynamics in Perovskite CH<sub>3</sub>NH<sub>3</sub>PbI<sub>3</sub> for Solar Cell Applications. *Journal of the American Chemical Society* **2014**, *136* (33), 11610-11613.
53. Uratani, H.; Yamashita, K., Charge Carrier Trapping at Surface Defects of Perovskite Solar Cell Absorbers: A First-Principles Study. *The Journal of Physical Chemistry Letters* **2017**, *8* (4), 742-746.
54. Shockley, W.; Read, W. T., Statistics of the Recombinations of Holes and Electrons. *Physical Review* **1952**, *87* (5), 835-842.
55. Hall, R. In *Germanium rectifier characteristics*, Physical Review, AMERICAN PHYSICAL SOC ONE PHYSICS ELLIPSE, COLLEGE PK, MD 20740-3844 USA: 1951; pp 228-228.
56. Lim, J. W. M.; Giovanni, D.; Righetto, M.; Feng, M.; Mhaisalkar, S. G.; Mathews, N.; Sum, T. C., Hot Carriers in Halide Perovskites: How Hot Truly? *The Journal of Physical Chemistry Letters* **2020**, *11* (7), 2743-2750.
57. Lim, J.; Hörantner, M. T.; Sakai, N.; Ball, J. M.; Mahesh, S.; Noel, N. K.; Lin, Y.-H.; Patel, J. B.; McMeekin, D. P.; Johnston, M. B., Elucidating the long-range charge carrier mobility in metal halide perovskite thin films. *Energy & Environmental Science* **2019**, *12* (1), 169-176.
58. de Quilletes, D. W.; Vorpahl, S. M.; Stranks, S. D.; Nagaoka, H.; Eperon, G. E.; Ziffer, M. E.; Snaith, H. J.; Ginger, D. S., Impact of microstructure on local carrier lifetime in perovskite solar cells. *Science* **2015**, *348* (6235), 683.
59. Conibeer, G., Get them while they're hot. *Nature Energy* **2020**, *5* (4), 280-281.
60. Limitations on Energy Conversion in Solar Cells. In *Physics of Solar Cells*, 2005; pp 137-153.
61. Ross, R. T.; Nozik, A. J., Efficiency of hot - carrier solar energy converters. *Journal of Applied Physics* **1982**, *53* (5), 3813-3818.

62. Xing, G.; Mathews, N.; Sun, S.; Lim, S. S.; Lam, Y. M.; Grätzel, M.; Mhaisalkar, S.; Sum, T. C., Long-Range Balanced Electron- and Hole-Transport Lengths in Organic-Inorganic CH<sub>3</sub>NH<sub>3</sub>PbI<sub>3</sub>. *Science* **2013**, *342* (6156), 344.
63. Sum, T. C.; Mathews, N.; Xing, G.; Lim, S. S.; Chong, W. K.; Giovanni, D.; Dewi, H. A., Spectral Features and Charge Dynamics of Lead Halide Perovskites: Origins and Interpretations. *Accounts of Chemical Research* **2016**, *49* (2), 294-302.
64. Fu, J.; Xu, Q.; Han, G.; Wu, B.; Huan, C. H. A.; Leek, M. L.; Sum, T. C., Hot carrier cooling mechanisms in halide perovskites. *Nature Communications* **2017**, *8* (1), 1300.
65. Yang, Y.; Ostrowski, D. P.; France, R. M.; Zhu, K.; van de Lagemaat, J.; Luther, J. M.; Beard, M. C., Observation of a hot-phonon bottleneck in lead-iodide perovskites. *Nature Photonics* **2016**, *10* (1), 53-59.
66. Li, C.; Wang, A.; Deng, X.; Wang, S.; Yuan, Y.; Ding, L.; Hao, F., Insights into Ultrafast Carrier Dynamics in Perovskite Thin Films and Solar Cells. *ACS Photonics* **2020**, *7* (8), 1893-1907.
67. Wang, R.; Mujahid, M.; Duan, Y.; Wang, Z. K.; Xue, J.; Yang, Y., A review of perovskites solar cell stability. *Advanced Functional Materials* **2019**, *29* (47), 1808843.
68. Snaith, H. J., Present status and future prospects of perovskite photovoltaics. *Nature Materials* **2018**, *17* (5), 372-376.
69. Raga, S. R.; Jung, M.-C.; Lee, M. V.; Leyden, M. R.; Kato, Y.; Qi, Y., Influence of Air Annealing on High Efficiency Planar Structure Perovskite Solar Cells. *Chemistry of Materials* **2015**, *27* (5), 1597-1603.
70. Ghahremani, A. H.; Martin, B.; Gupta, A.; Bahadur, J.; Ankireddy, K.; Druffel, T., Rapid fabrication of perovskite solar cells through intense pulse light annealing of SnO<sub>2</sub> and triple cation perovskite thin films. *Materials & Design* **2020**, *185*, 108237.

## Biography

Yuheng Liao received his B.S. degree in physics from Xi'an Jiaotong University, China. With a focus in non-linear optics, he began his graduate studies at Duke University in 2016. He is currently working with Prof. Warren S. Warren and Prof. Martin C. Fischer on pump probe microscopy study on charge carrier dynamics in MAPbI<sub>3</sub> thin films. He received the nanoscience fellowship at Duke (September 2018 – May 2019). During his graduate studies at Duke, he published two manuscripts: Yu, J., Li, Z., **Liao, Y.**, Kolodziej, C., Kuyuldar, S., Warren, W. S., Burda, C., Fischer, M. C., Probing the Spatial Heterogeneity of Carrier Relaxation Dynamics in CH<sub>3</sub>NH<sub>3</sub>PbI<sub>3</sub> Perovskite Thin Films with Femtosecond Time-Resolved Nonlinear Optical Microscopy. **Adv. Optical Mater.** 2019, 7, 1901185; Structural, Optical, and Electronic Properties of Two Quaternary Chalcogenide Semiconductors: Ag<sub>2</sub>SrSi<sub>4</sub>S<sub>4</sub> and Ag<sub>2</sub>SrGe<sub>4</sub>S<sub>4</sub>. Garrett C. McKeown Wessler, Tianlin Wang, Jon-Paul Sun, **Yuheng Liao**, Martin C. Fischer, Volker Blum, and David B. Mitzi. **Inorganic Chemistry** 2021 60 (16), 12206-12217.